FACULDADE DE ENGENHARIA DA UNIVERSIDADE DO PORTO

Parametric optimisation of thermoelectric planar devices: numerical simulation and development

Maria Carolina Chaves Fernandes

MASTER THESIS

Master in Mechanical Engineering

Supervisor: Prof. Sónia Isabel Silva Pinto

Co-Supervisor: Eng. Daniela Cristina Rodrigues Campanhã

July 23, 2020

Parametric optimisation of thermoelectric planar devices: numerical simulation and development

Maria Carolina Chaves Fernandes

Master in Mechanical Engineering

July 23, 2020

Abstract

With the increase of the energy needs and the demand for environmentally-friendly processes capable of obtaining useful energy, the expansion of applications for thermoelectric generators (TEGs) is a possible way of bridging the existing gap. Thermoelectric generators are reliable, flexible and wireless devices that are able to produce electricity through the recovery of waste heat, and they promote energy recovery in industrial environments.

The goals of this work were the simulation of a flexible planar thermoelectric generator made with bismuth telluride (Bi_2Te_3) and optimally design its geometry to efficiently generate electricity by taking advantage of a naturally existing temperature gradient.

Firstly, the research process took place, and the theoretical principles behind thermoelectricity were studied. Afterwards, the state of the art of the generators was reviewed, in order to establish the current state of the devices and the direction in which they are evolving in order to overcome the existing problems.

Then, an initial design of the generator was modelled in ANSYS 2019 and a sensitivity analysis took place to examine which geometrical and thermal changes resulted in a greater impact on the performance of the generator. The model of the generator was optimised through a parametric optimisation, both numerical and theoretical, in order to work at maximum power. The optimised parameters were the geometry, the dimensions and the number of thermocouples of the generator. The solutions of the numerical model were similar to the ones obtained with the created theoretical model.

With the optimisation process, the final optimal design of the thermoelectric generator was achieved, reaching 0.10 W of maximum power and producing an output voltage of 9.973 V when exposed to a temperature gradient between the temperatures of 20 °C and 150 °C. Additionally, the generator did not exceed the space limitations and worked with an efficiency level of 4.99%.

Keywords: thermoelectric, flexible devices, Seebeck effect, electricity generation, numerical simulation

Resumo

Com o aumento das necessidades energéticas e da procura por processos sustentáveis de obtenção de energia útil, a expansão de aplicações para geradores termoelétricos (TEG) representa uma estratégia de interesse de forma a preencher as lacunas existentes. Os geradores termoelétricos são dispositivos flexíveis e *wireless* que produzem eletricidade através da recuperação de calor residual e a sua utilização promove o aproveitamento energético em contextos industriais.

Os objetivos deste trabalho focaram-se na simulação numérica de um gerador termoelétrico planar flexível usando telureto de bismuto (Bi_2Te_3) e na optimização da sua geometria de modo a poder gerar eletricidade eficientemente, aproveitando um gradiente térmico naturalmente existente.

Primeiramente, deu-se o processo de pesquisa e foram estudados os princípios teóricos que sustentam a termoeletricidade. Posteriormente, foi analisado o estado da arte dos geradores, de modo a estabelecer o estado atual dos dispositivos e a direção de evolução destes de maneira a corrigir os problemas atualmente existentes.

Em seguida, um modelo inicial do gerador foi modelado no software ANSYS 2019 e uma análise de sensibilidade foi realizada para examinar quais os parâmetros com maior impacto no desempenho do gerador. O modelo do gerador foi posteriormente otimizado através de uma otimização paramétrica, numérica e teórica, para trabalhar na condição de potência máxima. Os parâmetros otimizados foram a geometria, as dimensões e o número de termopares do gerador. Verificou-se que as soluções dos modelos numérico e teórico apresentavam um comportamento similar.

Com o processo de otimização, o desenho ótimo final do gerador termoelétrico foi alcançado, atingindo 0,10 W de potência máxima e produzindo uma tensão em circuito aberto de 9,973 V quando exposto a um gradiente térmico entre as temperaturas de 20 °C e 150 °C. Além disso, o gerador não excedeu as limitações espaciais e exibiu uma eficiência de 4,99%.

Palavras-chave: termoelétrico, dispositivos flexíveis, efeito de Seebeck, geração de eletricidade, simulação numérica

Acknowledgements

Antes de tudo, gostaria da aproveitar este espaço para agradecer a todas as pessoas que permitiram e apoiaram a realização deste trabalho.

À minha orientadora, Professora Sónia Isabel Silva Pinto, e à co-orientadora do CeNTI, Eng. Daniela Cristina Rodrigues Campanhã, cujo conhecimento sobre os temas abordados, otimismo e apoio constantes foram essenciais para a elaboração desta dissertação. Para além disso, agradeço à Eng. Cristina Remédios Furtado, assim como à equipa do CeNTI, que me auxiliaram com conhecimentos técnicos.

À Faculdade de Engenharia da Universidade do Porto e, em especial, ao Departamento de Engenharia Mecânica, por ter sido uma segunda casa ao longo destes cinco anos, e a todos os docentes que me deram o conhecimento para poder exercer Engenharia profissionalmente.

Ao CeNTI, por me ter acolhido como estagiária e por me ter fornecido ótimas condições de trabalho.

Aos meus Pais, à minha Irmã e ao meu Avô, agradeço todos os esforços que fizeram para que eu pudesse ter chegado até aqui, assim como todo o apoio incondicional que sempre me deram. A todos os meus familiares, que sempre me acarinharam e apoiaram, ainda que à distância.

Aos meus amigos, pela amizade, pelo apoio, pelos momentos de descontração e por juntos termos festejado todos os sucessos que me trouxeram até aqui. Em particular, gostaria de agradecer à Ana Catarina Branco Ribeiro, por ser uma grande amiga nestes últimos cinco anos, com a qual quero conviver por muitos mais anos. Adicionalmente, ao Jorge Wolfs Gil, pelo apoio dado ao longo desta etapa, foste uma fonte de motivação essencial e incentivaste-me a dar o melhor de mim, mesmo quando não parecia o suficiente.

A todos, um enorme abraço e um sincero obrigado.

Carolina

True wisdom comes to each of us when we realise how little we understand about life, ourselves, and the world around us.

Socrates

Contents

List of Figures

List of Tables

Abbreviations

CEiiA	Centre for Excellence and Innovation in the Automotive Industry
CeNTI	Centre for Nanotechnology and Smart Materials
CITEVE	Technological Centre of the Textile and Clothing Industries of Portugal
CTIC	Technological Centre of Leather Industries
CNT	Carbon Nanotubes
FE	Finite Element
FEM	Finite Element Method
IRF	Integrity-Reliability-Failure
NASA	National Aeronautics and Space Administration
RTG	Radioisotope Thermoelectric Generator
TE	Thermoelectric
TEC	Thermoelectric Cooler
TEG	Thermoelectric Generator
TEH	Thermoelectric Heater

Symbols

A	cross-sectional area [m^2]
c	distance between consecutive legs [m]
e	electron charge [C]
h	height [m]
h	Planck constant [$m^2\,kg\,s^{-1}$]
h_{conv}	convection coefficient [$W\,m^{-2}\,K^{-1}$]
I	current [A]
J	current density [$A\,m^{-2}$]
K	conductance [S]
k	thermal conductivity [$W\,m^{-1}\,K^{-1}$]
k_B	Boltzmann constant [$W\,m^{-2}\,K^{-4}$]
L	length [m]
Lo	Lorenz number [$W\,\Omega\,K^{-2}$]
m	resistance ratio
m^*	effective mass [kg]
n	number of units in a TEG
n	carrier concentration [m^{-3}]
P	electrical power [W]
p	pitch [m]
Q	heat [J]
$\dot{Q}$	heat transfer rate [W]
$\dot{Q}_{high}$	heat transfer rate absorbed from the heat source [W]
$\dot{Q}_{low}$	heat transfer rate rejected to the heat sink [W]
$\dot{q}$	heat flux [$W\,m^{-2}$]
$\dot{q}'$	volumetric rate of heat generation [$W\,m^{-3}$]
R	electric resistance [Ω]
R_{int}	internal resistance [Ω]
R_{load}	load resistance [Ω]
R_{th}	thermal resistance [$K\,W^{-1}$]
S	Seebeck coefficient [$V\,K^{-1}$]
T	temperature [K]
t	thickness [m]
T_∞	temperature of fluid [K]
T_{high}	temperature of the heat source [K]

T_{low}	temperature of the heat sink [K]
T_{surf}	temperature of surface [K]
V	voltage [V]
V_{load}	load voltage [V]
V_{oc}	open-circuit voltage [V]
w	width [m]
$\dot{W}$	power [W]
$w_{generator}$	width of the generator [m]
z	figure of merit [K^{-1}]

GREEK LETTERS:

γ	ratio between cross-sectional area and length [m]
η	efficiency
μ	electrical mobility [$m^2 V^{-1} s^{-1}$]
μ_T	Thomson coefficient [$V K^{-1}$]
Π	Peltier coefficient [$W A^{-1}$]
ρ	electrical resistivity [Ωm]
σ	electrical conductivity [$S m^{-1}$]

Chapter 1

Introduction

1.1 Motivation

With the exponential growth of the world's population, the energy demands are constantly increasing. As a result, research is taking place in order to improve the efficiency of the already existing and well established methods of energy conversion, as well as using the current advances of technology to create innovative devices.

However, it is also important to guarantee that the methods used to obtain the required energy are sustainable and employ renewable sources. Therefore, practices like combustion of fossil fuels, like petroleum or coal, to produce electricity become unpractical, since the emitted gases are heavy contributors to global warming and climate change. In other words, despite being an established method with matured technologies and high versatility, its usage for electricity production has been steadily declining in recent years for sustainability reasons.

There are plenty of natural and renewable energy sources, such as the sun, wind, water courses, waves, and others, that have already proven their energy potential. However, not every country has promising levels of solar irradiation, wind speed or level differences to take advantage of these natural resources. Moreover, these sources of energy are not easy to implement in the transport sector, one of the biggest energy consumers, which needs to be adapted to the increase of intercultural mobility. Currently, this sector requires large amounts of fossil fuels, specially petroleum, whose reserves only exist in a small group of countries, creating a big dependency in countries without these resources. In the current economic and financial environment of countries like Portugal, the reduction of energy dependence on third parties is a possible way of bettering the economy, as well as the environment.

A very interesting method is the usage of special materials that are able to recover waste heat and convert it into electricity. Based on the unquestionable laws of thermodynamics, any working machine produces waste heat that, in most cases, is not "recycled" by the most conventional systems because it is set at lower temperatures [1].

Thus, the facts presented above have driven the development of alternative technologies for energy generation and recovery, namely thermoelectric generators (TEG).

1.2 Applications

Thermoelectric generation is mostly used near existing thermal gradients, like heat engines, recovering waste heat that would otherwise be entirely rejected to the environment. For example, since power generation plants reject high quantities of heat, thermoelectric generators are being used as a bottom cycle, increasing the efficiency of the overall system [2]. Additionally, TEGs have been proven to enhance the efficiency of solar thermal collectors, creating a hybrid system which produces heated waters and electricity [3, 4]. Moreover, in the past decade, the increased interest in nanotechnology has also been applied in thermoelectric generators [5].

Currently, researchers are also developing thermoelectric generators to be used in energy harvesting methods in several industries, namely the Automotive industry, by taking advantage of the high temperatures of the escape gases, that can be as high as 700 °C [1, 6, 7, 8, 9, 10, 11, 12, 13]. In addition, in Aeronautics, the implementation of these devices has been considered in airliners in order to power wireless sensors [14] and in spacecrafts, by recovering the energy from the decay of radioactive elements in order to produce electricity, called Radioisotope Thermoelectric Generator (RTG) [1, 15, 16]. In fact, Voyager 1, the space-probe launched by NASA (the National Aeronautics and Space Administration of the United States of America) in 1977 and the farthest man-made object from Earth, is powered by three RTGs with plutonium-238. [17].

Moreover, researchers have been studying the implementation of TEGs in wearable devices, taking advantage of body heat, due to the metabolism and muscular activity of an individual, in order to power electronics, such as biosensors, that could for instance power pacemakers and watches [18, 19, 20].

1.3 Objectives

As described in Section 1.2, despite this technology being successfully implemented in the Voyager 1 in 1977, the full potential of this technology has not been reached yet, and the range of the use of TEGs is still limited to experimental scenarios.

Additionally, it is important to highlight the relative lack of research of planar thermoelectric generators embedded in flexible substrates, as well as their manufacturing processes. In this scope, printed technologies are an attractive approach since, when combined with flexible materials, offer the possibility to produce low cost devices, and the process is suitable for mass production. Therefore, the production of TEGs based on these technologies, such as dispenser printing, becomes of interest for a near future, thus requiring a higher level of research for the improvement of printed TEGs.

To bridge these existing gaps, this project proposes to develop an optimally designed flexible thermoelectric generator, and attest its performance through numerical simulation. In order to achieve this goal, it is first necessary to understand the functioning of these devices and what the performance of the state-of-the-art devices is in order to develop the desired planar thermoelectric

generator and improve its design through numerical simulation of the geometry. Finally, it will be possible to verify the validity of the obtained model through numerical and theoretical analysis.

1.4 Thesis Outline

In Chapter 2, a theoretical analysis of the thermoelectric properties is presented, as well as the theoretical and mathematical definitions of the concepts of figure of merit and thermoelectric efficiency. Additionally, the heat transfer methods are addressed.

Chapter 3 glances at the state-of-the-art thermoelectric devices, the involved materials and manufacturing processes and finally the numerical simulation tools used by engineers and researchers to improve the desired phenomena.

Chapter 4 describes in detail the methods used to design and optimise the flexible TEG this project aims to construct. A comparison between the theoretical and the simulated results takes place in order to validate the model.

Chapter 5 presents a summary of the obtained results of the theoretical and numerical models, namely the output electrical properties the generator can provide to the load.

Chapter 6 expresses the main conclusions of the project and analyses possible future enhancements.

Appendix A shows images of the different modules that were numerically analysed in Section 4.2 regarding the sensitivity analysis of the model.

Appendix B shows the used EXCEL sheet used to perform the theoretical optimisation of the design of the generator.

Appendix C presents the full paper approved and published in the proceedings of *IRF2020 Conference (Integrity-Reliability-Failure)*. The presentation of the work at the conference will be held from the 6th to the 10th of September 2020, by video conference due to COVID-19 situation.

1.5 Centre for Nanotechnology and Smart Materials (CeNTI)

The Centre for Nanotechnology and Smart Materials, abbreviated to CeNTI, is a research and technological development institute whose main mission is the development of products contributing to several industries, mainly the Textile, Clothing and Automotive Industry.

It is well-established since 2006 in Vila Nova de Famalicão from a partnership between the Universities of Porto, Minho and Aveiro as well as the Technological Centre of the Textile and Clothing Industries of Portugal (CITEVE), and the Technological Centre of Leather Industries (CTIC), along with the Centre for Excellence and Innovation in the Automotive Industry (CEiiA), a center of Engineering and product development.

As of 2019, CeNTI has developed over 170 industrial projects, 111 projects funded at national level and 20 at European level. The more than 95 investigators that work on the Centre for Nanotechnology and Smart Materials have successfully conceded 7 patents and have 57 pending patents.

This non-profit institute focuses on prototyping, developing, analysing, testing and expanding smart materials and systems in order to incorporate more advanced technologies in traditional solutions found in the industries and markets, relying on cutting-edge technology and equipment. In fact, this centre is concerned in scientifically increasing the properties of the materials that most contribute to the national economy, such as textiles, polymers, leather, paper, glass, ceramics, natural stone, concrete, cork, wood and others. Consequently, CeNTI is notorious for working on projects with national industries, supporting and promoting domestic businesses and companies.

Moreover, along with other projects developed in cooperation with international entities, the Centre for Nanotechnology and Smart Materials aims to develop and legitimise new technologies [21].

Chapter 2

Theoretical analysis

Before proceeding with the design and optimisation of the thermoelectric performance, it is imperative to understand the underlying physical phenomena that occur in the conversion of heat into electricity in these devices, namely the involved heat transfer mechanisms and effects that can occur in these devices, like the Seebeck, Thomson and Peltier effect. Afterwards, it will be possible to fully understand the thermoelectric effect and understand the different variables that most contribute to the efficiency of these devices.

2.1 Thermoelectric effect

A thermoelectric generator is a solid-state device which, when subjected to a temperature gradient, has the power to transform heat into electricity according to the Seebeck effect. Moreover, the process can be reversed in order to preserve a temperature gradient, as is the case of Peltier coolers or heaters, which operate according to the Peltier effect. Figure 2.1 displays a basic scheme of the operating mechanism of TEG [22, 23].

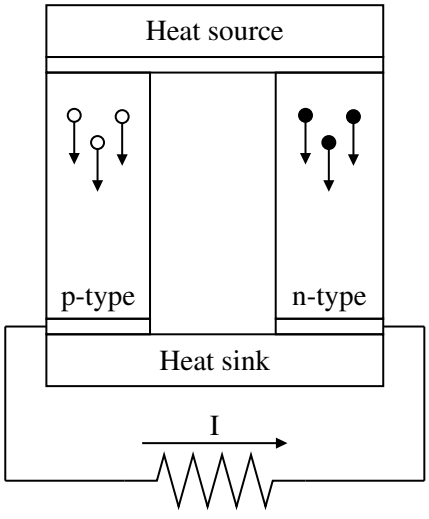

Figure 2.1: Power generation process. Adapted from [22].

A TEG unit, composed of two vertical "legs" connected at the top, are placed between a heat source and a heat sink, the first at a higher temperature than the latter, separated only by a thin layer of a conductive material that ensures the heat is uniformly distributed in the cross-sectional area of the legs. This configuration leads to a temperature gradient being imposed in the TEG, leading to the instability of the carriers on both legs. These charged particles diffuse and tend to move from the hot surface to the cold surface [24].

As seen in Figure 2.1, p- and n- type leg units - the first witnessing the movement of positive particles (or holes, h^+), represented as white circles, and the second of negative particles (or electrons, e^-), displayed as black circles, respectively – accumulate these charges at the bottom near the heat sink, generating an electrostatic potential or, in other words, a voltage [24].

The ratio between the electric potential and the temperature gradient is an interesting variable used to compare the produced voltage of different materials given the same temperature gradient, and it is called Seebeck coefficient [22, 24].

2.2 Seebeck Effect

The Seebeck effect was first discovered by the German physicist Thomas Seebeck in 1821 [25]. At the time, he noticed that a metallic needle would move when it was near a loop made with two different metallic materials whose junctions were exposed to two different temperatures. A scheme of the setup can be seen in Figure 2.2 [26].

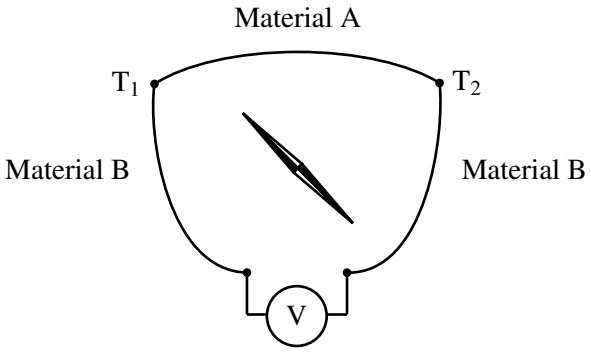

Figure 2.2: Seebeck effect experimental setup. Adapted from [26].

With the setup shown in Figure 2.2, this physicist discovered that there was a current flow through the circuit. The ruling equation of the Seebeck effect is displayed in Equation 2.1 where ΔV is the voltage differential, ΔT is the temperature difference and S_A and S_B are the Seebeck coefficients of material A and B, respectively [1, 26, 27].

$$\Delta V = -(S_A - S_B) \cdot \Delta T \tag{2.1}$$

When the two legs are made of the same material, the Seebeck coefficients of the p- and n-type can be considered symmetrical and, therefore, the electric potential is not null. For the purpose of simplification, let S be the Seebeck coefficient of a uni-material thermocouple, equal to the double

of the Seebeck coefficient of the material ($2 \cdot S_A$). In fact, the voltage is directly proportional to the number of pairs of p- and n-legs, in other words, the number of thermocouples, present in the generator, since they are connected electrically in series, as illustrated in Figure 2.1.

The Seebeck coefficient is a function of the temperature because the mobility of the charged particles is heavily connected with their energy level [26, 27, 28]. As such, it is possible to further develop Equation 2.1 into Equation 2.3, which represents the theoretical equation used to calculate the generated open-circuit voltage for a specific TEG and temperature gradient between T_{high} and T_{low} of the heat source and heat sink, respectively, where n is the number of thermocouples present in the generator.

$$dV = -S(T) \cdot n \cdot dT \therefore \tag{2.2}$$

$$V_{oc} = -n \cdot \int_{T_{low}}^{T_{high}} S(T) dT \tag{2.3}$$

Consequently, the produced electricity and the overall efficiency of the thermoelectric device are also dependent on the temperature [7, 20, 27, 29].

2.3 Joule effect

In 1841, James Prescott Joule, a British physicist, discovered that when a conductive material is subjected to a flow of electrons, heat is generated. In his experiment, a copper wire was immersed in a recipient of water and the ends were connected to a battery in order to induce a current flow in the created closed circuit. During a period of time, Joule measured the temperature of the liquid, which increased continuously during the experiment [30].

This discovery was extremely relevant at the time, because it turned the ruling Caloric Theory, a theory that described heat as a weightless fluid, obsolete and promoted further research of energy phenomena, leading to the universally accepted laws of Thermodynamics that currently exist [30].

Subsequently, this physicist deduced that the produced heat transfer rate, equal to the electrical power, P, could be calculated as a function of the current, I, squared, and the resistance R, generating Equation 2.4, also known as Joule's First Law [30].

$$P = R \cdot I^2 \tag{2.4}$$

2.4 Thomson effect

Another important physicist that contributed to the knowledge of thermoelectrics was William Thomson, better known as Lord Kelvin, the developer of the Kelvin temperature scale [31].

As reported by the effect studied by this British physicist, if a material is exposed to two different temperatures and there is a current I flowing through it, according to the direction of the current flow, the material will absorb or emit additional heat. The most significant difference

between this phenomenon and the Seebeck effect is that there is only one material and not a couple of materials [22].

As can be seen from Figure 2.3, a current is flowing through a material exposed to a high temperature and low temperature in each extremity. In situation (a), the current flow is in the same direction as the increase of the temperature, whereas in situation (b), the direction of the current flow is preserved, but the temperature increases in the opposite direction. According to this effect, the material absorbs heat in the former and it releases heat in latter situation [22, 32].

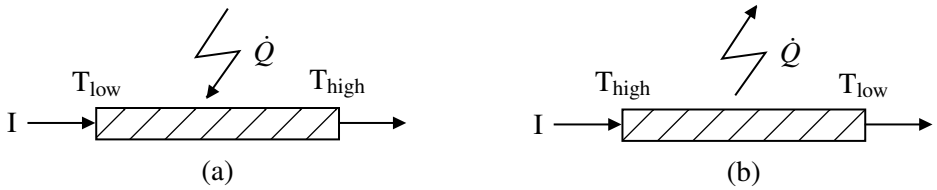

Figure 2.3: Heat absorption or emission due to the Thomson effect.

In other words, the volumetric heat generation rate $\dot{q}'$, expressed in $\mathrm{W\,m^{-3}}$, is the Joule heat transfer rate increased or decreased by the Thomson heat transfer rate per unit of volume. A ruling equation for the phenomenon is given by Equation 2.5 [22, 32, 33].

$$\dot{q}' = \rho \cdot J^2 \pm \mu_T \cdot J \cdot \frac{dT}{dx} \tag{2.5}$$

In fact, Equation 2.5 involves several parameters. Namely, the current density, J, meaning the electric current that flows through the material per unit of area perpendicular to the flow, is measured in $\mathrm{A\,m^{-2}}$. Additionally, what is essentially the inverse of the electrical conductivity, ρ, the electrical resistivity, represented in Ωm, quantifies how well a material opposes the flow of electric current. Moreover, μ_T is the Thomson coefficient, which is related to the variation of temperature to pressure (it measures the uniformity of the thermal properties of the material, unlike the Seebeck coefficient) and $\frac{dT}{dx}$ is the temperature variance throughout the material [22, 32, 33].

As previously stated, the thermal power per volume unit can be split into two parcels. Firstly, there is the resistant heating, directly obtained from Joule's First Law, presented in Equation 2.4. Secondly, there is the Thomson heat rate, which is responsible for linking the existing temperature gradient and the installed current and the Thomson coefficient.

Furthermore, it is possible to make a correlation between the Seebeck coefficient and the Thomson coefficient, as can be seen from Equation 2.6 [34].

$$\mu_T = T \cdot \frac{dS}{dT} \tag{2.6}$$

2.5 Peltier effect

Finally, the last effect to be introduced is the Peltier effect. The phenomenon adopted the name of the French physicist which studied it in the 19^{th} century [27]. It describes the opposite of

the Seebeck effect. It basically suggests that when a current is flowing through two dissimilar materials conjoined in two places, there will be a heat transfer process occurring in each junction, one absorbing and the other emitting. Therefore, the environment surrounding the junction that absorbs heat will witness its temperature increase whereas the other extremity will lose heat and lower its temperature [22, 32, 35, 36].

Each material possesses a Peltier coefficient, Π, which indicates the heat transfer rate that is exchanged in the joint between the materials over the current that flows through, which is obtained through experimentation [27].

Equation 2.7 translates the Peltier effect, where $\dot{Q}$ is the heat transfer rate and Π_A and Π_B are the Peltier coefficients of material A and B, respectively [22, 27, 32, 35, 36].

$$\dot{Q} = I \cdot (\Pi_A - \Pi_B) \tag{2.7}$$

From the analysis of the units, the relationship between the Seebeck and Peltier coefficients is simple and it is shown in Equation 2.8 [37].

$$\Pi = S \cdot T \tag{2.8}$$

2.6 Heat transfer mechanisms

There are three main heat transfer mechanisms: conduction, convection and, finally, radiation. In thermoelectric generators, the latter process is, at lower temperatures, despicable. Therefore, in this Section, the mechanism of conduction and convection are presented, in Subsection 2.6.1 and Subsection 2.6.2, respectively.

2.6.1 Conduction

The process of conduction is a heat transfer phenomenon through random motion of atoms which happens due to a temperature gradient. The rate of this energy transfer mechanism, or heat transfer rate, $\dot{Q}$, depends, for steady-state conditions, on the cross-sectional area, A, the thermal conductivity of the material, k, as well as the temperature variation in the direction of the heat flow x, $\frac{dT}{dx}$. Knowing that heat flows in the direction of the lowest temperature, the steady-state one-directional heat transfer rate is described by Equation 2.9, known as Fourier's Law [38, 22].

$$\dot{Q} = -k \cdot A \cdot \frac{dT}{dx} \tag{2.9}$$

Unlike the heat transfer rate, the heat flux does not depend on the cross-sectional area, since this parameter measures the heat which flows through a single square metre of area per time unit, $\dot{q}$, as can be seen in Equation 2.10 [38].

$$\dot{q} = -k \cdot \frac{dT}{dx} \tag{2.10}$$

For an unidirectional permanent heat transfer rate on a homogeneous flat surface, both the heat rate and the heat flux are constant. Consequently, it is possible to obtain an equation that represents the temperature distribution through the material with integrals, through the process presented in Equations 2.11 - 2.13 [38].

$$\frac{d^2T}{dx^2} = 0 \tag{2.11}$$

$$\therefore \frac{dT}{dx} = C_1 \tag{2.12}$$

$$\therefore T(x) = C_1 \cdot x + C_2 \tag{2.13}$$

In short, the variation of temperature through the thickness of the materials is linear and when the corresponding boundary-conditions are applied, it is possible to obtain the exact temperature distribution. Given that the legs of the thermoelectric generator, with a length L, are connected by a high conductivity material, it is safe to approximate the temperature of the waste heat, T_{high}, to the temperature of the top surface of the thermoelectric and, similarly, the heat sink temperature, T_{low}, to the bottom surface of the thermoelectric legs. Mathematically, these conditions can be expressed as Equation 2.14 [38].

$$\begin{cases} T|_{x=0} = T_{low} \\ T|_{x=L} = T_{high} \end{cases} \tag{2.14}$$

Therefore, the constants C_1 and C_2 are discovered, and Equation 2.13 transforms into Equation 2.16. The graphic representation of this equation is a linear function, with a slope given by the temperature gradient and the length of the material [38].

$$\begin{cases} T_{low} = C_2 \\ T_{high} = C_1 \cdot L + C_2 \end{cases} \tag{2.15}$$

$$\therefore T(x) = \frac{T_{high} - T_{low}}{L} \cdot x + T_{low} \tag{2.16}$$

2.6.1.1 Thermal resistance

When there is a series of different materials that compose the block through which the heat transfer rate is intended to be measured, the easier approach which can be followed to determine the temperature distribution is the thermal resistance one. This analysis is based on the similarity between the phenomena and ruling equations of an electrical resistance and a thermal resistance.

An electrical resistance is used to control the flow of electricity in an electrical circuit. Comparatively, a thermal resistance, R_{th} measures the opposition a given material has against heat that flows through itself [38].

In Equation 2.17, Ohm's Law is stated and it correlates the resistance, the potential differential and the current outlined in Figure 2.4. In contrast, the thermal resistance is similarly related to the heat transfer rate $\dot{Q}$ and the temperature difference ΔT in an object, as shown by Equations 2.18 and 2.19, sketched in Figure 2.5. It is important to notice that Equation 2.19 derives from introducing Equation 2.9 in Equation 2.18.

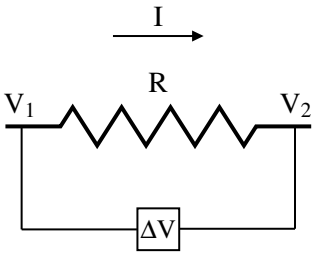

Figure 2.4: Current flow through an electrical resistor.

$$R = \frac{\Delta V}{I} \tag{2.17}$$

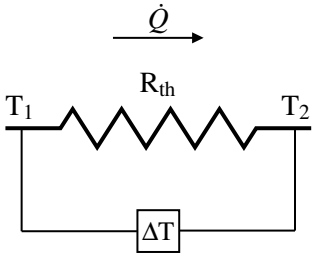

Figure 2.5: Heat flow through an object.

$$R_{\text{th}} = \frac{\Delta T}{\dot{Q}} \tag{2.18}$$

$$\therefore R_{\text{th}} = \frac{L}{k \cdot A} \tag{2.19}$$

In Figure 2.6, an example of a wall with four layers exposed to two different temperatures, on the outer surfaces of material A and D (T_{high} and T_{low}, respectively) is shown. The temperatures on the contact surface between layers are not known, and are represented by T_1, T_2 and T_3. Since the materials are all in series, just as in the electricity realm, it is possible to calculate an effective resistance, R^*, by adding all resistances. This method is interesting, because it simplifies the calculations, when there are many materials and layers. In fact, a new wall with the same thickness but made up of only one hypothetical material with a resistance equal to R^* when exposed to the same temperature difference, would have the same heat transfer rate, as is shown in Figure 2.7.

The more conductive a material is, the smaller the slope of the temperature distribution function, given that the material will have approximately the same temperature in all its volume. On the other hand, materials with smaller conductivity levels, like insulators, are good at preserving a temperature gradient, so the slope is understandably bigger.

Higher values of thermal resistance lead to lower values of heat transfer rate and, therefore, to the recovery of a smaller amount of wasted heat. A way of decreasing the thermal resistance is by

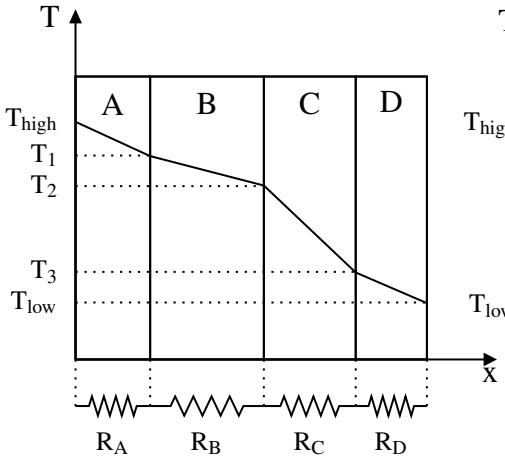

Figure 2.6: Temperature profile of a wall with several flat layers.

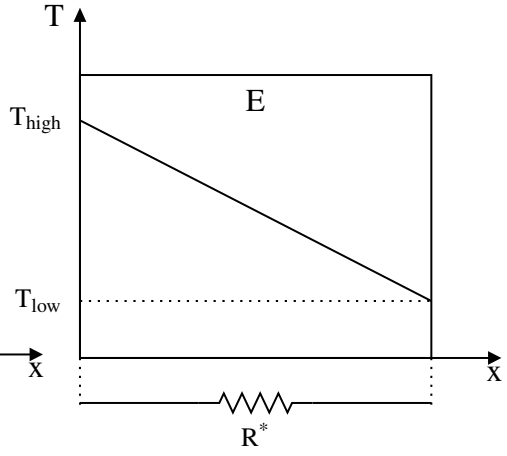

Figure 2.7: Temperature profile of the equivalent material.

manipulation of the parameters of Equation 2.19.

There are, therefore, three possible routes that allow the change of the thermal resistance.

The first one revolves around the choice of materials, by choosing the most suitable state-of-the-art materials. This way, the intrinsic property of conductivity can be changed to the desired values. However, a vast majority of these materials are still in development, and information on their properties can be difficult to find. For this reason, this scenario can hardly be analysed through a theoretical perspective. Another possible option is changing the thickness of each layer and finding an optimal combination of thicknesses values to reach a lower value of R_{th}. Thirdly, it is possible to alter the area of the layers or, in other words, the product of width and length of each material, in order to increase this parameter.

Therefore, the more suitable ways of modifying the thermal resistance to desired values is through the alteration of the second and last aspects. In other words, it is the geometrical optimisation of the thermoelectric device that can lead to the evaluation and optimisation of its performance.

2.6.2 Convection

The process of convection is another heat transfer mechanism, which is the result of the interaction between the surface of a solid and a circulating fluid at a different temperature. This process is divided into forced convection, which occurs when the motion of the fluid is induced by an external source, such as wind or a fan, and natural convection, when the difference in buoyancy in the fluid, caused by the temperature gradient within the fluid, is the principal cause of the fluid movement [38].

For both convection processes, the steady-state heat transfer rate depends on the surface area, the temperature of the surface of the solid, T_{surf}, the fluid temperature, T_∞ and the convection

coefficient, h_{conv}, expressed in $W\,m^{-2}\,K^{-1}$. Once more, since the heat transfer occurs from the highest to the lowest temperature, it is possible to define Equation 2.20.

$$\dot{Q} = h_{conv} \cdot A \cdot (T_s - T_\infty) \tag{2.20}$$

2.7 Evaluation of performance

Understanding the physical phenomena that occur in an operational thermoelectric generator, it is now important to understand how to evaluate its efficiency. To assess the ability of converting waste heat into electricity, the materials that constitute the generator are theoretically analysed in Subsection 2.7.1 as well as the whole generator and the conditions it works in, in Subsection 2.7.2 and Subsection 2.7.3.

2.7.1 Figure of merit

It is important to underline that not all materials have relevant levels of the thermoelectric effect based on their atomic structure. A coarse way to divide materials by their conductivity is in three groups: Conductors, Semiconductors and Insulators. It could be thought that the p- and n-type materials to use in the legs would be good conductors, to increase the mobility of the charged particles, producing a higher voltage. However, as will be seen in this Section, these materials must be semiconductors because of the conflicting properties that rule the Seebeck effect [24].

In fact, the most used parameter to evaluate the performance of a thermoelectric material is its figure of merit, z, expressed in K^{-1}. The figure of merit translates how well a certain material generates power, so the higher the z, the better the material will perform. It is usual, however, to represent this as an non-dimensional number, zT, being called the dimensionless figure of merit.

To calculate this non-dimensional number, expressed in Equation 2.21, it is necessary to know the Seebeck coefficient, expressed in VK^{-1}, the temperature, in K, the electrical conductivity, σ, in $S\,m^{-1}$ (the S stands for Siemens which is equivalent to Ω^{-1}) and the thermal conductivity, expressed in $W\,K^{-1}$.

$$zT = \frac{S^2 \cdot \sigma \cdot T}{k} \tag{2.21}$$

Equation 2.21 originated the concept of thermoelectric power factor, which is simply $S^2\sigma$ and it is expressed in $W\,m^{-1}\,K^{-2}$ [37].

Analysing the calculation method for the figure of merit, a good thermoelectric material must have a high electrical conductivity, low thermal conductivity and a high Seebeck coefficient. In fact, a higher electrical conductivity allows for a lower Joule heating, since the resistive heat produced is unwanted and lowers the efficiency of the process. Furthermore, a lower thermal conductivity is a good quality in order to preserve the temperature gradient and not its decay, which would result in a lower potential difference. Additionally, a higher Seebeck coefficient

maximises the conversion of heat into useful power, the main reason for the use of these devices [1, 22, 37].

However, optimising these three parameters is not easy because they are interdependent properties. In other words, the calculation of each individual property requires the use of the same variables.

First, an expression for the Seebeck coefficient was developed by Snyder et al. (2008) and can be seen in Equation 2.22 [24].

$$S = \frac{8\pi^2 \cdot k_B^2}{3e \cdot \mathbf{h}^2} \cdot m^* \cdot T \cdot \left(\frac{\pi}{3\mathbf{n}}\right)^{2/3} \tag{2.22}$$

In Equation 2.22, k_B is the Boltzmann constant (approximately equal to $5.67 \cdot 10^{-8}\,\mathrm{W\,m^{-2}\,K^{-4}}$), e is the electron charge (roughly $1.602 \cdot 10^{-19}$ C for positive charges and $-1.602 \cdot 10^{-19}$ C for negative ones), **h** is the Planck constant (approximately $6.626 \cdot 10^{-34}\,\mathrm{m^2\,kg\,s^{-1}}$), m* is the effective mass [1] , in kg, **n** is the carrier concentration, in $\mathrm{m^{-3}}$, and T is the temperature, in K.

Furthermore, the electrical conductivity is calculated with the carrier concentration, electron charge and the particle mobility, μ, and it is evident in Equation 2.23 [3].

$$\begin{aligned} \sigma &= \frac{1}{\rho} \\ &= \mathbf{n} \cdot e \cdot \mu \end{aligned} \tag{2.23}$$

Moreover, the electrical and thermal conductivity are intimately related, and their association can be made with Wiedemann-Franz Law, defined in Equation 2.24. Establishing that the thermal conductivity of a material is composed by electron and phonon mobility components, this law establishes that the electronic portion of the thermal conductivity, k_{e^-}, is influenced by the electrical conductivity. Additionally, as seen in Equation 2.25, Lo represents the Lorenz number, which depends on the material properties [40].

$$\frac{k_{e^-}}{\sigma} = Lo \cdot T \tag{2.24}$$

$$Lo = \frac{\pi^2}{3} \cdot \left(\frac{k_B}{e}\right)^2 \tag{2.25}$$

Looking at Equation 2.22, in order to maximise the Seebeck coefficient of a material, and therefore enhance its conversion of thermal energy to electricity, one would have a large effective mass and a low carrier concentration. However, the decrease of the carrier concentration would lead to a higher electrical resistivity and, therefore, a lower flow of particles, as can be deduced

[1] The effective mass, a concept used in theoretical physics, is a measurement of the apparent mass of a particle when subjected to a force or, in this particular case, a thermal distribution, as a result of the band theory of solid state particles. For most cases, this value can be assumed as constant for a given material [39, p. 197-202].

from Equation 2.23. Finally, according to the Wiedmann-Franz Law, the decrease of the electrical conductivity would lead to the reduction of the thermal conductivity for the same temperature.

Therefore, the figure of merit and the power factor are two conflicting and interdependent properties, and to find an equilibrium among them, very conductive materials cannot be chosen. Taking into consideration that insulating materials do not exhibit enough values of thermal and electrical conductivity, the ideal materials for thermoelectric devices are semiconductors. Bubnova et al. (2012) made a symbolic and simple comparison between four classes of materials according to their electrical and thermal conductivities, as seen in Figure 2.8 [41].

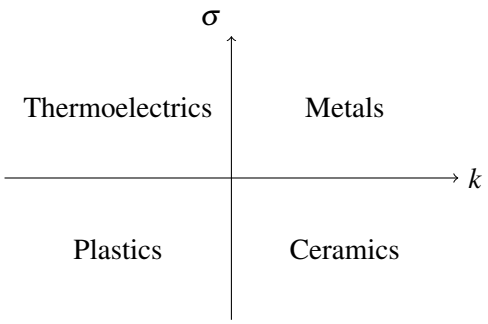

Figure 2.8: Electrical and thermal conductivities of some materials. Adapted from [41].

As a matter of fact, the thermal conductivity and electrical conductivity are, in a physics' point of view, the movement of phonons and electrons, respectively. To be enhanced, a semiconductor material needs, therefore, to allow the propagation of electrons, but retard the propagation of phonons, and such process can be done by altering the crystalline structure in nanoscale [26, 37, 41, 42]. The state-of-the-art methods of enhancement of thermoelectric (TE) properties are presented in Section 3.3.

In order to visualise the independence of the properties in question, Snyder et al. (2008) plotted $S^2\sigma$, σ, S, k and zT as a function of the carrier concentration, for Bi_2Te_3, a semiconductor material, and the graph is presented in Figure 2.9 [24].

In Figure 2.9, the figure of merit and the power factor reach their peak levels at different carrier concentration values. However, as stated previously, zT is the best parameter to describe thermoelectric materials and, from the previous Figure, the ideal carrier concentration that maximises the figure of merit in this case is between $10^{19}\,cm^{-3}$ and $10^{20}\,cm^{-3}$.

According to the current advances in this technology, however, it is considered that for values of zT close to 1, as is the case of Figure 2.9, the thermoelectric devices are not sufficiently efficient. Moreover, researchers diverge on what the minimum value of the figure of merit should be in order for a given TEG to lead to a feasible increase of energy recovery. For instance, according to Twaha et al. (2016), the device is only efficient for values of zT approximately equal to 2 [22], whereas L. Bell (2008) states that a figure of merit equal or greater than 1.5 is sufficient to guarantee the efficiency of the thermoelectric device [43].

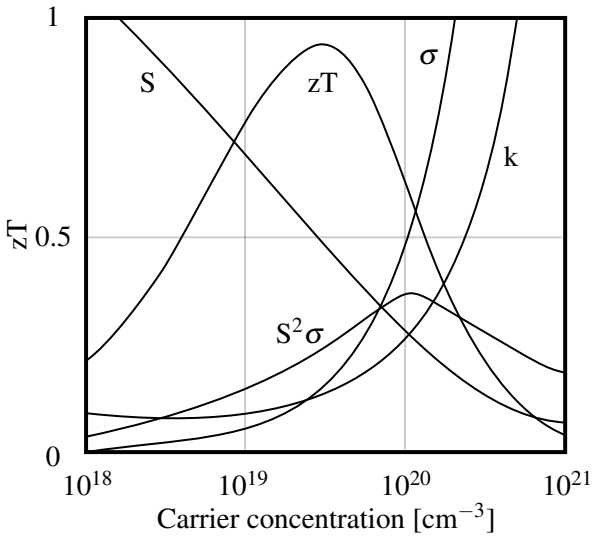

Figure 2.9: Thermoelectric parameters as a function of the carrier concentration. Adapted from [24].

2.7.2 Thermal and electrical parameters

In order to obtain the efficiency of the thermoelectric generator, it is required to know parameters such as heat transfer rate, current, voltage and electrical power, since they are the basic parameters of this technology.

There are two different types of heat transfer rates that contribute to the generation of the current in the terminals of the thermoelectric unit: $\dot{Q}_{high}$ is the thermal power absorbed from the heat sink, which is at a constant temperature equal to T_{high}, and $\dot{Q}_{low}$ is the rejected heat transfer rate from the TEG to the heat sink, at a corresponding temperature of T_{low}, usually the atmospheric temperature. As seen in Figure 2.10, given the symmetry of the generator, it is possible to assume that each leg rejects half of the total emitted heat.

Performing an energy balance in the hot junction and the cold junction between the legs and the conductive material, resorting to the First Law of Thermodynamics, it is possible to find the expressions to calculate $\dot{Q}_{high}$ and $\dot{Q}_{low}$, respectively. Because of the already mentioned effects, and assuming the complete thermal and electrical isolation of the surfaces of the TEG, the number of different heat flows that occur in the generator increases to four.

First, $\dot{Q}_{high}$ and $\dot{Q}_{low}$ need to be accounted. Secondly, there is the Joule heat transfer rate, $\dot{Q}_J$, calculated in Equation 2.26, that happens due to the current flow and the internal resistance of the thermoelectric materials. The latter property, R_{int}, is calculated knowing the resistivity, the inverse of the thermal conductivity, length and cross-sectional area of each p- and n-type legs, identically as seen in Equation 2.19. It is presented in Equation 2.27, where the indexes p and n correspond to the properties of p- and n-type legs, respectively.

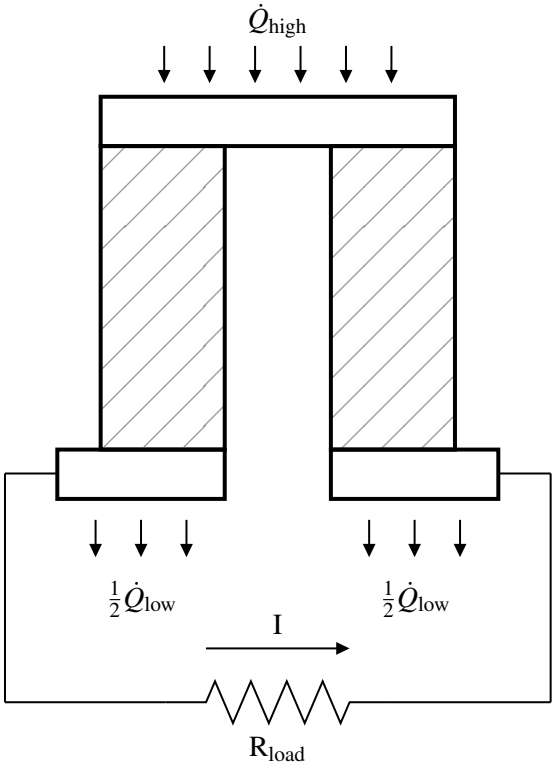

Figure 2.10: Thermoelectric unit in a circuit. Adapted from [22].

$$\dot{Q}_J = I^2 \cdot R_{int} \tag{2.26}$$

$$R_{int} = \frac{\rho_p \cdot L_p}{A_p} + \frac{\rho_n \cdot L_n}{A_n} \tag{2.27}$$

Thirdly, it is necessary to take into account the conduction heat transfer rate, $\dot{Q}_{\text{cond}}$, that flows through the semiconductor legs through conduction. An easier way to calculate the conduction heat is by introducing the concept of conductance, K, the inverse of the internal resistance calculated in Equation 2.29, expressed in Ω^{-1} [1].

$$\dot{Q}_{cond} = (T_{high} - T_{low}) \cdot K \tag{2.28}$$

$$K = \frac{k_p \cdot A_p}{L_p} + \frac{k_n \cdot A_n}{L_n} \tag{2.29}$$

Finally, there is the Peltier heat transfer rate, $\dot{Q}_{\text{P}}$, that is emitted in the hot surface and absorbed in the cold junction to preserve their temperature as a result of the thermoelectric effect. It can be simply calculated in Equations 2.30 and 2.31, for the hot and cold junctions, respectively [22, 32, 35, 36].

$$\dot{Q}_{P_{high}} = S \cdot I \cdot T_{high} \tag{2.30}$$

$$\dot{Q}_{P_{low}} = S \cdot I \cdot T_{low} \tag{2.31}$$

Performing an energy balance in 2.32, the expression used to calculate $\dot{Q}_{\text{high}}$ is found in Equation 2.33 [1, 19].

$$\dot{Q}_{\text{high}} + \frac{1}{2} \cdot \dot{Q}_J - \dot{Q}_{cond} - \dot{Q}_{P_{high}} = 0 \tag{2.32}$$

$$\therefore \dot{Q}_{\text{high}} = -\frac{1}{2} \cdot I^2 \cdot R_{int} + (T_{high} - T_{low}) \cdot K + S \cdot I \cdot T_{high} \tag{2.33}$$

Similarly, the outcome of the energy balance in the cold junction, presented in Equation 2.34, leads to Equation 2.35, used to calculate $\dot{Q}_{\text{low}}$ [1, 19].

$$\dot{Q}_{\text{low}} - \frac{1}{2} \cdot \dot{Q}_J - \dot{Q}_{cond} - \dot{Q}_{P_{low}} = 0 \tag{2.34}$$

$$\therefore \dot{Q}_{\text{low}} = \frac{1}{2} \cdot I^2 \cdot R_{int} + (T_{high} - T_{low}) \cdot K + S \cdot I \cdot T_{low} \tag{2.35}$$

From Figure 2.10, it is concluded that the output power can be calculated as the product between the current squared, I^2, and the load resistance, R_{load}, according to the component that is going to be powered by the thermoelectric generator, through Equation 2.4.

In fact, understanding that the device is a heat engine, the generator can also be represented as a generic power cycle, represented in Figure 2.11.

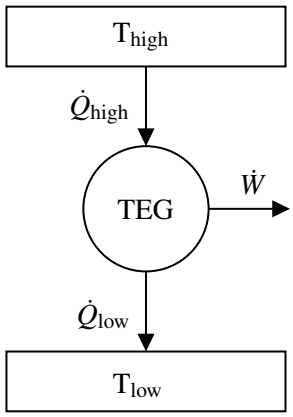

Figure 2.11: Simplified representation of thermoelectric generator.

Therefore, applying the First Law of Thermodynamics, it is concluded that the output power, represented as $\dot{W}$ in Figure 2.11, can also be calculated as the difference between $\dot{Q}_{\text{high}}$ and $\dot{Q}_{\text{low}}$. Furthermore, this expression, shown in Equation 2.36, can be completed when combined with Equations 2.33 and 2.35, as seen in Equation 2.37.

$$\dot{W} = \dot{Q}_{\text{high}} - \dot{Q}_{\text{low}} \therefore \tag{2.36}$$

$$= S \cdot I \cdot (T_{high} - T_{low}) - I^2 \cdot R_{int} \tag{2.37}$$

From Ohm's Law and Joule's First Law, the voltage and the current can be calculated through Equation 2.38 and 2.39, respectively [1].

$$V = S \cdot (T_{high} - T_{low}) - I \cdot R_{int} \tag{2.38}$$

$$I = \frac{S \cdot (T_{high} - T_{low})}{R_{int} + R_{load}} \tag{2.39}$$

On the thermoelectric module, the voltage is the difference between the Seebeck voltage, resultant of the Seebeck effect, and a voltage which depends on the internal resistance of the materials, as well as the current that flows through the device [1, 34]. It is now finally possible to calculate the efficiency of the generator.

2.7.3 Efficiency

The efficiency of a heat engine is the ratio between the produced electricity and the energy that needs to be provided to the device. For the theoretical Carnot cycle, the Carnot efficiency η_{Carnot} depends only on the natural boundaries, in other words, the existing temperature gradient from which the energy is going to be recovered. Unlike the real thermodynamic cycles, the Carnot cycle does not witness internal irreversible effects of loss of useful energy [44, 45], like thermal conduction and Joule heat [46]. The Carnot efficiency is a basic parameter used to understand the maximum theoretical potential of the technology. It is calculated in Equation 2.40 [12, 24, 42, 47].

$$\eta_{Carnot} = \frac{T_{high} - T_{low}}{T_{high}} \tag{2.40}$$

For a thermoelectric generator, the efficiency is the ratio between $\dot{W}$ and $\dot{Q}_{\text{high}}$, the heat extracted from the heat source. Introducing the concept of m, the ratio between the load resistance and the internal resistance defined in Equation 2.27, a new expression for $\dot{W}$ and $\dot{Q}_{\text{high}}$ can be obtained to simplify the calculation of the efficiency. These new equations are equivalent to the ones obtained previously and are presented in Equations 2.42 and 2.43 [36, 48].

$$m = \frac{R_{load}}{R_{int}} \tag{2.41}$$

$$\dot{W} = m \cdot \frac{S^2 \cdot (T_{high} - T_{low})^2}{(1+m)^2 \cdot R_{int}} \tag{2.42}$$

$$\dot{Q}_{\text{high}} = -\frac{1}{2} + K \cdot \frac{(1+m)^2 \cdot R_{int}}{S^2 \cdot (T_{high} - T_{low})} + \frac{T_{high} \cdot (1+m)}{T_{high} - T_{low}} \tag{2.43}$$

Dividing Equations 2.42 and 2.43, the efficiency is given by Equation 2.44 [36, 48].

$$\eta = \frac{T_{high} - T_{low}}{T_{high}} \cdot \frac{m}{-\frac{1}{2} \cdot \frac{T_{high} - T_{low}}{T_{high}} + \frac{K \cdot R_{int}}{S^2 \cdot T_{high}} \cdot (1+m)^2 + (1+m)} \tag{2.44}$$

From the previous Equation, it is noticeable that the efficiency of the generator is the product between the Carnot efficiency and the efficiency of the geometry, material and conditions of the generator. Additionally, it is possible to understand that the conversion efficiency is directly proportional to the leg length, but inversely proportional to the cross-sectional area of the legs [49]. Moreover, it is deductible that the efficiency increases with the temperature gradient, just like the Carnot efficiency. The hotter the heat source or the colder the heat sink, the better the thermoelectric generator will perform, given that there is more waste energy to be recovered.

Additionally, it is possible to simplify Equation 2.44 even further. Looking at the denominator, the term $\frac{K \cdot R_{int}}{S^2 \cdot T_{high}}$ is none other than the inverse of the non-dimensional figure of merit for the temperature of the heat source. The Equation can be simplified into Equation 2.45 [36].

$$\eta = \eta_{Carnot} \cdot \frac{m}{-\frac{1}{2} \cdot \eta_{Carnot} + \frac{(1+m)^2}{zT_{high}} + (1+m)} \tag{2.45}$$

It is apparent from Equation 2.45 that the efficiency of a thermoelectric generator is closely linked to the figure of merit of the material, such as the Seebeck coefficient and the thermal and electrical conductivities, as well as the ratio between the load and the internal resistances and finally the temperature gradient the generator is exposed to.

However, the thermoelectric generator is a device that allows the recovery of energy from an already existing source. In other words, the heat source is set at a non-adjustable temperature and the heat sink is usually the ambient temperature. In addition, in a practical scenario, as will be seen in Section 3.2, each semiconductor material has an optimum particular range of temperatures in which it excels its performance, so an increase of the temperature gradient may not necessarily lead to more generated electricity. Therefore, η is mostly dependent on z and m.

For the optimisation of the efficiency, the figure of merit should be elevated or, in other words, the product of the internal resistance and the conductance should be minimised. This approach in the optimisation problem can only be done when the material intrinsic properties can be manipulated synthetically.

Creating the variables γ_p and γ_n as the ratio between the cross-sectional area and the length of the p- and n-type legs, respectively, the geometrical properties, the ones that are going to be adjusted in the design optimisation, can be related, in Equation 2.46 and 2.47, respectively.

$$\gamma_p = \frac{A_p}{L_p} \tag{2.46}$$

$$\gamma_n = \frac{A_n}{L_n} \tag{2.47}$$

Multiplying Equations 2.27 and 2.29 and replacing Equations 2.46 and 2.47, $K \cdot R_{int}$ becomes a function of γ_p and γ_n as well as the mechanical properties of thermal conductivity and electrical resistivity. Calculating the minimum of $K \cdot R_{int}$, the optimum ratio between γ_p and γ_n that leads to the maximum figure of merit is found, calculable with Equation 2.49.

$$\frac{d(K \cdot R_{int})}{d(\frac{\gamma_n}{\gamma_p})} = 0 \therefore \left(\frac{\gamma_n}{\gamma_p}\right)_{optimum} = \sqrt{\frac{\rho_n \cdot k_p}{\rho_p \cdot k_n}} \therefore \tag{2.48}$$

$$z_{max}\Big|_{\left(\frac{\gamma_n}{\gamma_p}\right)_{optimum}} = \left(\frac{S}{\sqrt{\rho_p \cdot k_p} + \sqrt{\rho_n \cdot k_n}}\right)^2 \tag{2.49}$$

As mentioned previously, it is also possible to optimise the efficiency of the thermoelectric by adjusting the resistance ratio, m. In this case, the increase of the ratio decreases the efficiency of the thermoelectric conversion and, therefore, it is desired to find the optimal value of m to maximise η. Calculating the value of m for which the derivative of Equation 2.45 as a function of m is null, $m_{optimum}$ is established such that the efficiency is maxed [24]. This calculation is done in the set of expressions of Equation 2.50, where $\overline{T}$ represents the average temperature between T_{high} and T_{low}.

$$\begin{aligned} &\frac{d\eta}{dm} = 0 \therefore m_{optimum} = \sqrt{1 + z \cdot \overline{T}} \therefore \\ &\eta_{max} = \eta_{Carnot} \cdot \frac{\sqrt{1 + z \cdot \overline{T}} - 1}{\sqrt{1 + z \cdot \overline{T}} + \frac{T_{low}}{T_{high}}} \end{aligned} \tag{2.50}$$

By evaluating Equation 2.50, the maximum practical efficiency of the thermoelectric generator is equal to the Carnot efficiency if the figure of merit is infinite [50]. Finally, it is possible to calculate the maximum electrical output, once again by calculating the optimum m that maximises $\dot{W}$, using Equation 2.52 [19].

$$\frac{d\dot{W}}{dm} = 0 \therefore m_{optimum} = 1 \therefore \tag{2.51}$$

$$\dot{W}_{max} = \frac{1}{4} \cdot \frac{S^2 \cdot (T_{high} - T_{low})^2}{R_{int}} \tag{2.52}$$

$$\eta|_{\dot{W}\max} = \frac{1 - \left(\frac{T_{low}}{T_{high}}\right)}{2 - \frac{1}{2} \cdot \left(1 - \frac{T_{low}}{T_{high}}\right) + \frac{4 \cdot \frac{T_{low}}{T_{high}}}{z \cdot T_{low}}} \tag{2.53}$$

As seen from the results, for an optimum value of the resistance ratio of one, the internal resistance of the model must be equal to the load resistance [27, 32, 34, 36, 51, 52, 53].

Interestingly enough, the maximum power output does not correspond to the produced power at maximum efficiency as seen in Equation 2.53, obtained by calculating η for the maximum

power output, $\eta|_{W_{max}}$. In applications for heat recovery, it is more interesting to extract the maximum power possible instead of having the device work at maximum efficiency [7].

Chapter 3

State of the art

In order to develop the model of the thermoelectric generator, it is necessary to evaluate the already existing solutions. Therefore, an analysis of literature of several research projects took place, which particularly and generally focused on thermoelectric devices and their characteristics, such as materials and their treatment, geometry and manufacturing processes.

3.1 Thermoelectric devices

The use of thermoelectric generators is associated with several advantages. For instance, given the absence of emission of pollutants to the atmosphere, this technology is environmentally friendly, a relevant characteristic for the current energy paradigm [9, 45, 54]. Secondly, TEGs have no moving components, which grants them low levels of maintenance, reducing operation costs and even reducing sound pollution [1, 36, 45, 49, 52, 54]. Additionally, these devices are wireless, autonomous, portable [43] and are also lightweight [32]. Moreover, the devices are easily adaptable and scalable to the energy requirements in each particular situation [5, 34, 45, 55]. Finally, the thermoelectric devices can work in two different ways: producing electricity by taking advantage of a temperature gradient, the case of TEGs, or by inducing a desired temperature difference by consuming electricity, the case of Thermoelectric Coolers (TECs) or Thermoelectric Heaters (TEHs), depending on the desired effect [11, 22, 24].

However, the thermoelectric process has a significant disadvantage: in fact, the conversion process of recovering waste heat is not a very efficient method when compared to other heat engines, especially well-established power cycles [5, 27]. As seen in Figure 3.1, the efficiency is quite low, between 5% and 7%, when the heat sink is set at ambient temperature [22, 47].

Despite the worse results in comparison with other technologies, the current scientific efforts of material research, design geometry, modelling and manufacturing, as well as the increase of the number of uses of this technology, have been strong measures to its further development, having the overall efficiency increased in just a few decades [22, 32, 52]. As seen in Section 1.2, with the

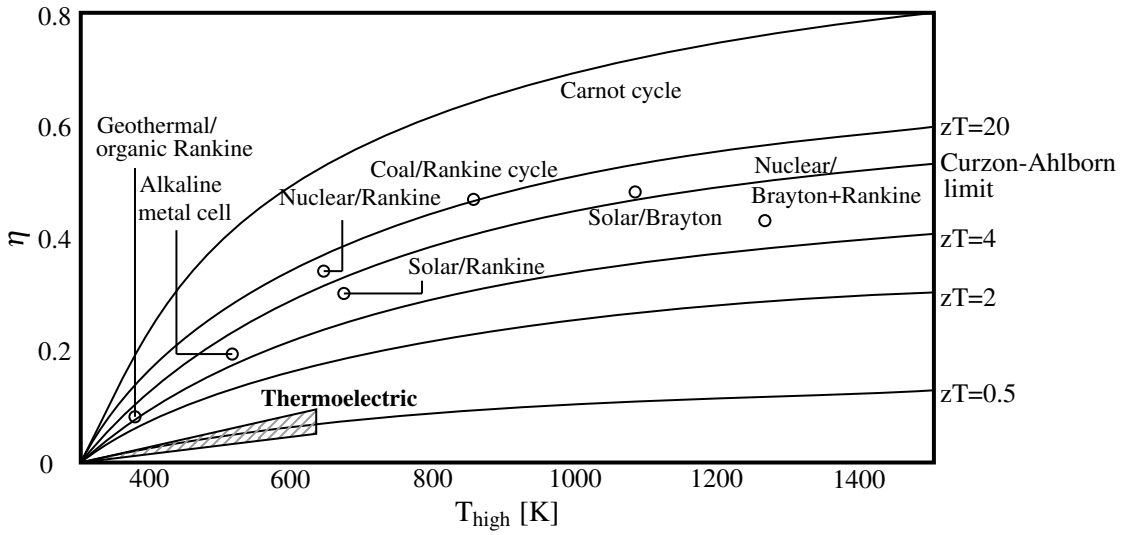

Figure 3.1: Power generation efficiency of several heat engines. Adapted from [47].

advances in technology, thermoelectric generators and coolers/heaters have been able to integrate many scientific researches in a range of areas, like Electronics, Medicine, Engineering, Textile, Automotive and Aeronautical, in a successful manner, providing characteristics unmatched by other more powerful heat engines.

The thermoelectric generators consist of an array of thermoelectric units, such as the one seen in Figure 2.10, connected at the bottom. However, the thermoelectric units can be designed in several other ways, according to the desired application. In fact, the most common dispositions are vertical and planar, shown, respectively, in Figures 3.2 and 3.3 [56].

As opposed to the vertical display, the planar design, considered in this project, is thinner and, therefore, more easily printed onto a substrate. A planar device exhibits less mechanical shear stress, making it withstand flexion and torsion conditions, resulting in a device which is adaptable to stretchable and bendable environments. Moreover, it requires less material than a vertical design. The planar thermoelectric devices are mostly used as wearable parts, since they exhibit a greater flexibility and occupy less volume [5, 18, 19]. However, the planar generator requires a lot of space in one dimension because it can hardly be folded. In contrast, vertical generators can be arranged to occupy less space, as illustrated in Figure 3.4 [22, 35].

As stated in Section 2.7.1, the non-dimensional figure of merit is the best performance indicator of the semiconductor materials. This parameter depends on the properties of the materials, which in turn depend on the crystalline structure, which is significantly influenced by the material processing. Additionally, knowing that the geometric imperfections have a bigger impact in these typically small devices, the manufacturing of the devices needs to have good precision and respect very tight tolerances. Finally, the fabrication procedure is ultimately aided by numerical analysis and computer simulation of the device in operation conditions, in order to save time and resources. Therefore it is important to know the materials, the synthesising, the computational analysis and the fabrication of the state-of-the-art devices.

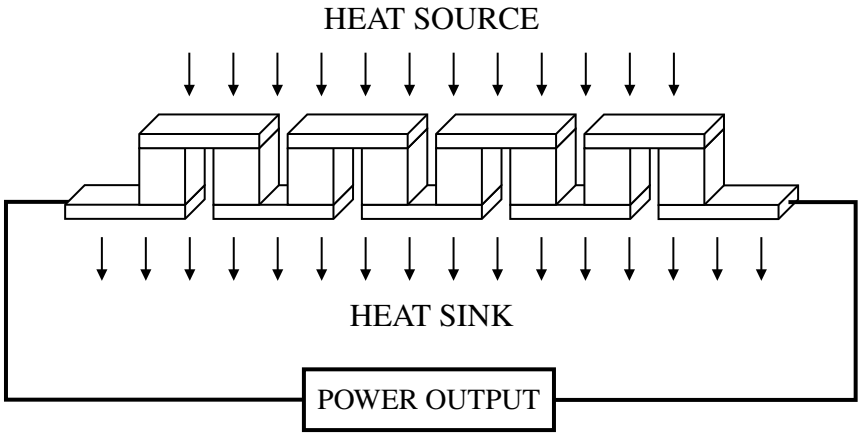

Figure 3.2: Vertical generator. Adapted from [56].

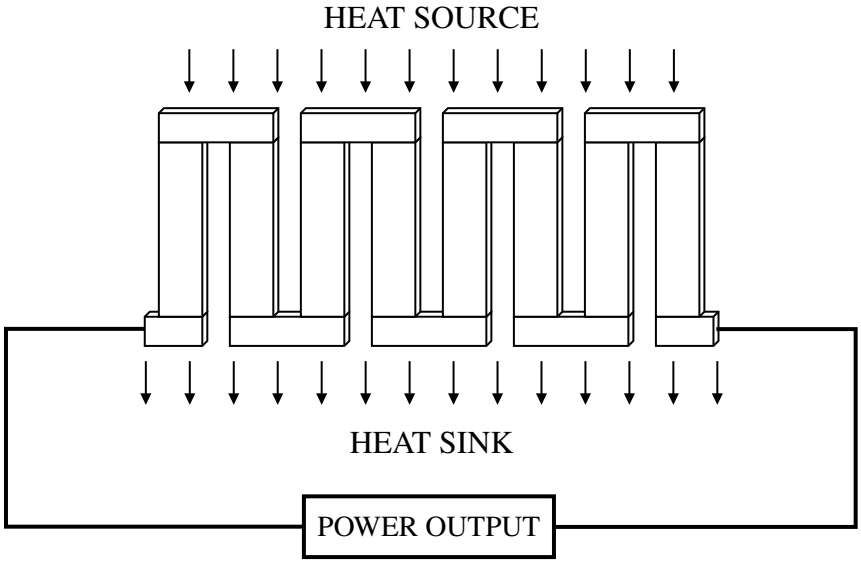

Figure 3.3: Planar generator. Adapted from [56].

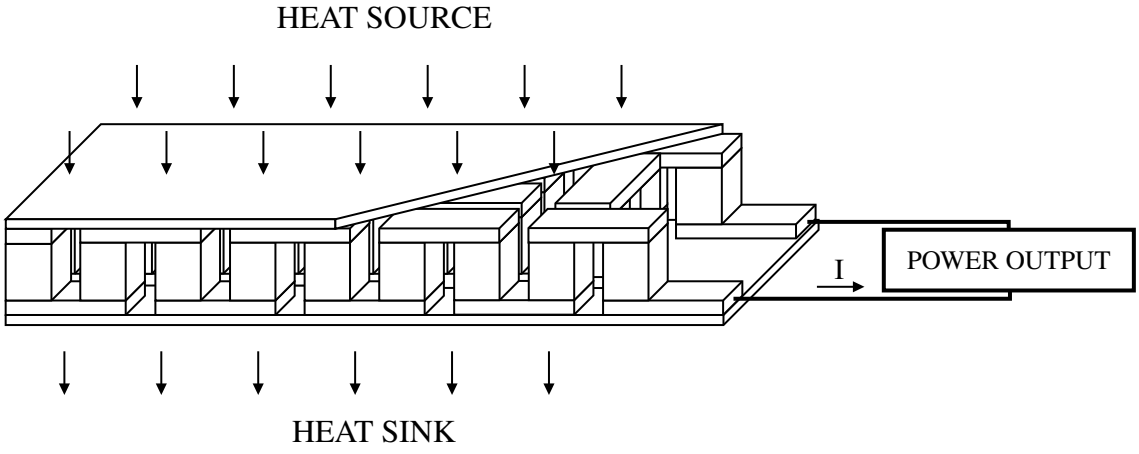

Figure 3.4: Compact vertical generator. Adapted from [35].

3.2 Materials

Semiconductors materials are used in thermoelectric processes because they have a great balance between the Seebeck coefficient, electrical and thermal conductivities. According to Yao et al. (2019), Figure 3.5 illustrates the most used materials in thermoelectric research of the scientific community [46].

In general, TE materials can be classified in different aspects. For instance, thermoelectric materials are classified in three groups, according to the temperature range their thermoelectric performance excels in. Firstly, there are the low temperature TE materials, with a temperature range from 300 K to 500 K; secondly, the medium temperature thermoelectric materials, which posses an optimum range between 500 K and 900 K; finally, the high temperature TE materials are characterised for exhibiting peak figure of merit levels in temperatures above 900 K [56].

Moreover, semiconductor materials can also be organic and inorganic. In fact, organic semiconductor materials are promising because they carry the advantages of being lightweight, flexible and economical, but have significantly lower figure of merit values than the inorganic materials [57], so only the latter materials are going to be studied in this project.

However, inorganic semiconductors can also be characterised by their crystalline composition and structure. In fact, a semiconductor material can be distinguished as chalcogenide, silicide, half-Heusler, skutterudite, clathrate or oxide [6, 57]. Naturally, there are other emerging materials with potential to be implemented in generators, such as electronically conducting polymers, graphene and carbon nanotubes (CNT) [26].

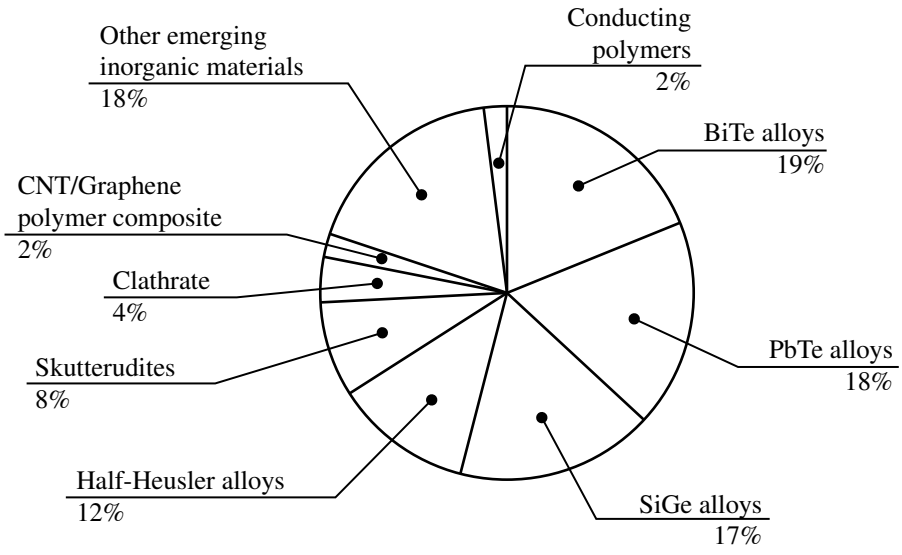

Figure 3.5: Use of semiconductor materials in scientific research of TEG. Adapted from [46].

Baranowski et al. (2012) collected information about the technological advances of certain thermoelectric materials, and the variation of the figure of merit with the working temperature for state-of-the-art p-type and n-type semiconductors is shown in Figure 3.6 and 3.7, respectively

[55]. Additionally, Table 3.1 illustrates the cost of some materials in raw and pure form [6], which can be linked to their potential and abundance of these materials.

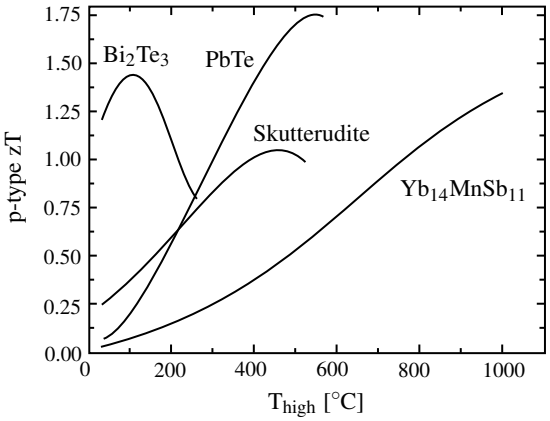

Figure 3.6: Figure of merit of p-type semiconductors. Adapted from [55].

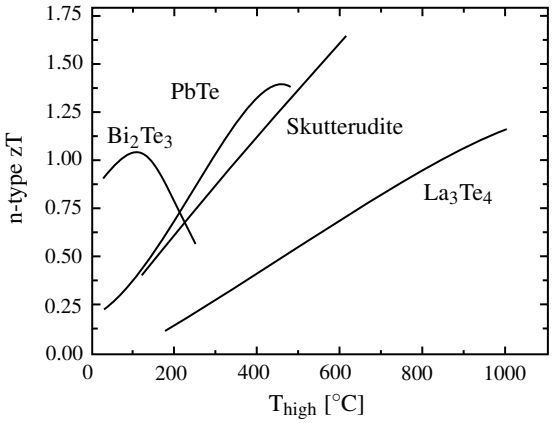

Figure 3.7: Figure of merit of n-type semiconductors. Adapted from [55].

Table 3.1: Cost of raw and pure thermoelectric materials. Adapted from [6].

Material family	Material composition	Cost of raw material [€· kg^{-1}]	Cost of pure material [€· kg^{-1}]
Chalcogenide	Bi_2Te_3	102	746
	PbTe	46.3	93
	$AgPb_{18}SbTe_{20}$	78	537
Silicide	$Si_{0.8}Ge_{0.2}$	343	6550
	$Mg_2Si_{0.85}Bi_{0.15}$	6.5	177
Half-Heusler	$Ti_{0.8}Hf_{0.2}NiSn$	10.2	491
Skutterudite	$Yb_{0.2}In_{0.2}Co_4Sb_{12}$	22.2	189
Clathrate	$Ba_8Ga_{16}Ge_{28}Zn_2$	569	3675
Oxide	$(Zn_{0.98}Al_{0.02})O$	1.9	46.3

3.2.1 Chalcogenides

The first group of materials, where BiTe and PbTe are included, is used in about 37% of scientific research [46]. In this class, materials with elements from group 16 of the periodic table are included, therefore, tellurides, sulfides, selenides and polonides belong in this category [6].

Bismuth Telluride, BiTe, is a well established semiconductor and the most used in thermoelectric devices, either generators or Peltier coolers/heaters. This low temperature thermoelectric material exhibits a better performance at room temperature usage, with an optimum average temperature range between 0 °C and 150 °C [14, 56]. Given this thermal characteristic, this material has been studied intensively since the interest for this technology grew in the scientific community

in the late half of the 20th century, where the number of papers on the semiconductor materials increased significantly [58].

Bismuth is a group 15 element of the periodic table, making it a pnictogen. Unlike the other heavy metals, Bi is non-toxic. Additionally, it is one of the elements with the lowest thermal conductivity values since it has a low number of free electrons. Furthermore, Bi has some of the highest electrical resistivity levels in the periodic table. This material is the seventieth most abundant in the world. On the other hand, tellurium, Te, is a rare element on earth, with an abundance level that is similar to neon [59]. This metal exhibits good electrical conductivity levels, resulting, when allied with other semiconductor elements, in a promising material.

Lead telluride, PbTe, is a semiconductor material with an elevated figure of merit, as illustrated by the graph of Figure 3.6 [55]. Apart from bismuth telluride, Te-based semiconductor materials are the most indicated for medium temperature applications [24, 56] and have been used by NASA in space probes [6].

3.2.2 Silicides

The second group of materials are the silicides, which are applied in generators exposed to higher temperatures. Silicon-germanium, SiGe, the most common silicide, is an interesting semiconductor material because it is able to maintain acceptable performance levels at temperatures around 1000 °C because the materials withstand thermal stress without degrading [6]. This material is mostly used in power supplying components for space exploration and planetary missions. In fact, NASA has implemented this material in the RTG that powers the Voyager 1, Voyager 2, Galileo, New Horizons and, together with the European Space Agency, the Ulysses and Cassini spacecrafts [17, 56, 60]. Due to its excelling performance levels, SiGe is one of the most expensive thermoelectric materials [6].

3.2.3 Half-Heuslers

Thirdly, there are the half-Heuslers and their alloys. These materials, like the silicides, are more suitable to higher temperature applications [6], and comprise a simple cubic crystalline structure [24]. Due to possessing inter-metallic compounds in their crystalline structure, these materials have a high thermal conductivity and Seebeck coefficient. However, with the enhancement methods that will be explained further, it is possible to decrease k [6, 26].

3.2.4 Skutterudite and Clathrates

Additionally, Skutterudite is a material discovered in 1845 in Norway, named after the region where it was first found. Its general formula is AB_3, with A and B being a transition element and an element from group 15, respectively. This material family revealed itself to be promising, particularly $CoAs_3$, $FeAs_3$ or $NiAs_3$, due to the high particle mobility, low electrical resistivity and elevated Seebeck coefficient [3].

This family of materials, as well as clathrates, has a very complex cage-like crystal structure [37] with voids on the inside which, thanks to nanotechnology, can be filled with particles of immense electrical conductivity levels, increasing the overall thermoelectric efficiency, through methods which are going to be mentioned in Section 3.3 [6, 24, 26]. However, the properties of the overall system are different for each filling compositions and are difficult to predict [3].

3.2.5 Oxides

Finally, there are the oxides semiconductor materials. Without synthetic alteration of the structure, these materials are deemed as inferior thermoelectric materials, because of their low particle mobility and high thermal conductivity [47]. However, the tuning of their properties has led to the increase of their thermoelectric performance at higher temperatures. Therefore, researchers are still studying techniques to further enhance this abundant and thermally stable family of materials, in order for its implementation to be cost-effective [24].

3.2.6 Substrate materials

The substrate, where the planar thermoelectric generators are placed, are usually made from a flexible material, which varies according to the desired application. For instance, Park et al. (2017) produced a flexible thermoelectric generator implemented on a wristband in order to take advantage of body heat to produce electricity, and placed the TEG on a layer of polyimide which was proven to excel mechanically [61]. Likewise, Zhu et al. (2018) created a small flexible planar generator onto a paper-based substrate, producing, then, a lightweight thermoelectric generator [62]. Furthermore, Lu et al. (2016) was able to fabricate a generator and integrate it into silk [63], and reported that the 100 load cycles applied to the generator did not impact its performance. In addition, Elmoughni et al. (2019) was able to create a prototype of a flexible thermoelectric knitted onto fabric [64]. As tested by Elmoughni et al. (2019), the usage and cleaning of the fabric the wearable thermoelectric generator was placed on led to significant increases of the internal resistance, and a corresponding deterioration of the performance. Nonetheless, the condition of flexibility was not affected by the maintenance procedures [64].

Additionally, the substrate material needs to withstand bending and twisting to provide the generator the required structural support [65]. Therefore, the mechanical properties of polymeric films are relevant. For instance, the flexural modulus measures the flexibility of polymeric materials, and lower values of this property are a synonym of a greater flexibility [66].

Moreover, the thermal properties of the substrate are also relevant. In fact, the contact surface area between planar thermoelectric generators and their substrate is higher than a generator with a vertical design, which leads to more dissipated heat. Therefore, in order to minimise this undesired effect, the substrate material needs to have low values of thermal conductivity [67, 68], as well as good dimensional stability at higher temperatures, by having a low coefficient of thermal expansion [66]. Finally, the substrate material should be inert to avoid chemical reactions with

the environment and the other materials of the generator, as well as an electric insulating material [69].

3.3 Enhancement of thermoelectric properties of materials

With the advances of technology, the currently used semiconductor materials are heavily synthesised to enhance their properties, through their alloyment with other elements [24]. Additionally, the crystalline structure of thermoelectric materials could be complemented with nanoparticles or nanostructures, like carbon nanotubes, in order to scatter the phonons and decrease the thermal conductivity as a result, without affecting the regular flow of electrons. However, nanostructuring is not going to be approached in this project due to its complexity [37].

Melt-and-growth is a commonly adopted process for mechanically alloying semiconductors. For this practice, it is first necessary to mix pure powders of each separate element in the chosen proportions into a container. If necessary, the powder can be ball milled, in order to reduce the dimensions of the particles. Then, the mixture is put in a vacuum, to stop the surrounding air, specially the oxygen and water components, from interacting with the powders. Afterwards, the mixture is exposed to a heat treatment and it is melted and annealed in a period of time between 72 and 96 hours, in order to achieve the desired microstructure [26, 70].

Gayner et al. (2016) measured thermoelectric properties, such as S, σ, k and zT, of $Si_{0.8}Ge_{0.1}$ at 27 °C being unannealed, annealed at 1345 °C and annealed at 1365 °C, and the results are presented in Table 3.2 [26]. It is visible in Table 3.2 that the Seebeck coefficient increased when the material was annealed, while the conductivities decreased. However, the figure of merit increased, indicating that annealing at higher temperatures is beneficial. Comparing the annealed semiconductors, the increase of the annealing temperature led to the reduction of the S and k and the raise of the electrical conductivity.

Table 3.2: Influence of annealing $Si_{0.8}Ge_{0.1}$ at 27 °C. Adapted from [26].

Process	Property at 27 °C			
	S [$\mu V K^{-1}$]	σ [$S cm^{-1}$]	k [$W m^{-1} K^{-1}$]	zT
Unannealed	140	1052	9.73	0.0636
Annealed at 1345 °C	155	768	7.67	0.0722
Annealed at 1365 °C	151	845	6.00	0.0964

In Figure 3.8, the figure of merit values of some alloys of the previously indicated materials are presented [3].

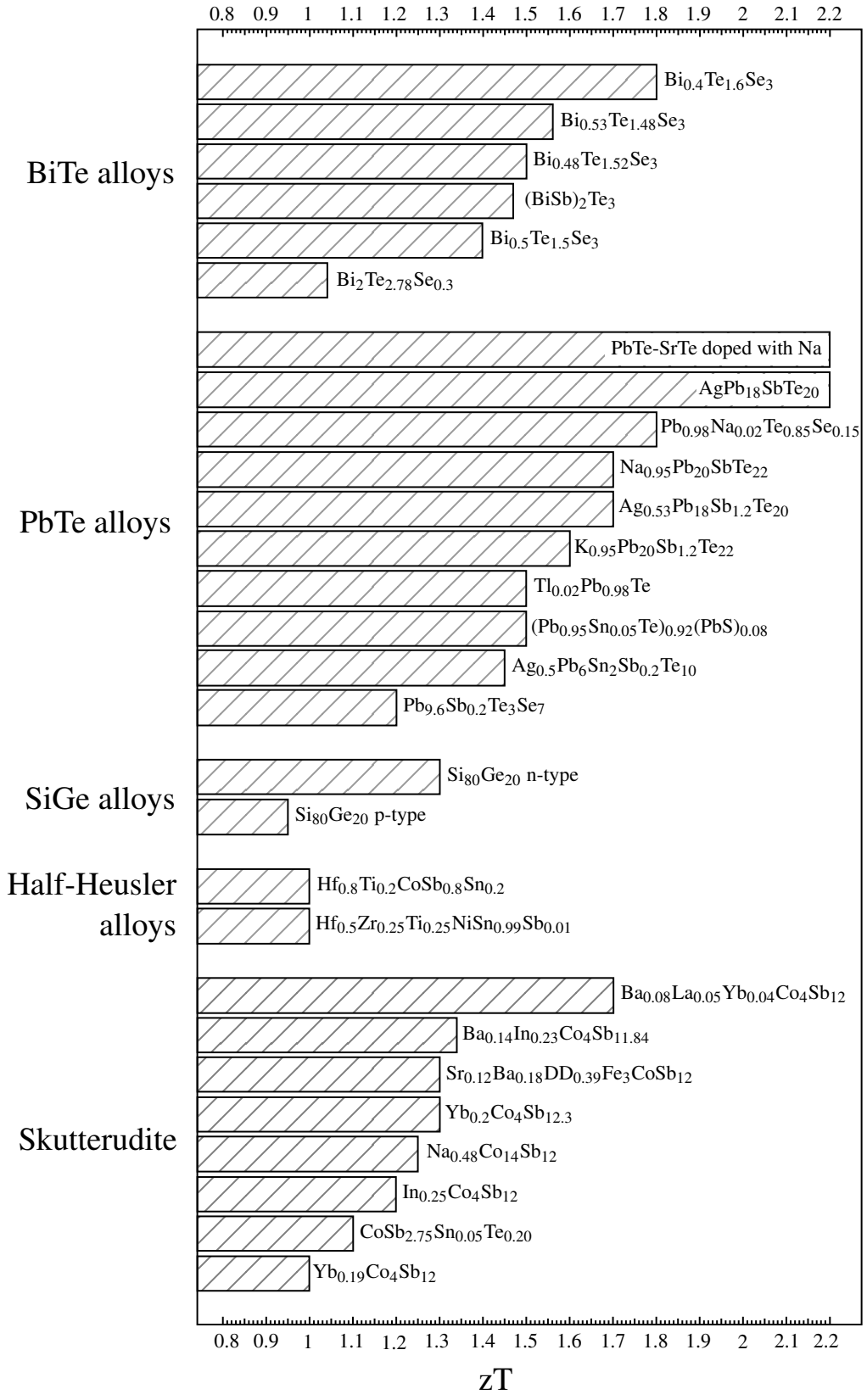

Figure 3.8: Figure of merit of several semiconductor materials. Adapted from [3].

3.4 Manufacturing processes

The manufacturing processes are responsible for transforming the heavily synthesised materials into thermoelectric generators. Once more, there are several possible methods, even though only a small range is adequate for the production of thermoelectrics which resemble the generators studied by this project. However, in certain cases, it is also possible to adapt some already established manufacturing processes, such as flexography or screen-printing, in order to manufacture thermoelectric generators onto fabrics [53].

For flexible thermoelectric generators, dispensing is a method of additive manufacturing which consists on the deposition of material onto a substrate. Dispenser printing machines have higher levels of resolution, around 1 µm and are easily programmable to print small and complex geometries [53, 71, 72]. Additionally, this additive manufacturing process has the advantage of not producing significant waste products [53].

The printed material comes in the form of an ink, which means the semiconductor materials are embedded into a resin component, providing it a suitable viscosity to be printed by this technique. In addition to these two primary materials, there are also minor additives which increase the quality of the printed product and promote the homogenisation of the mixture. Therefore, the creation of the thermoelectric inks is a meticulous process, since the proportions between the binding, the semiconductor and the additive materials need to be adequate in order to guarantee a working final product. Moreover, it is also necessary to have conductive inks to print the bridges between semiconductor units. However, there are commercially available conductive inks with elevated levels of conductive properties and, therefore, it is possible to skip the formulation for conductive inks.

The printing process is phased, since the printing of several materials needs to be sequential. First, the conductive materials are printed in the substrate, followed by the semiconductor materials. An advantage of using inks is the fact that they are printed at lower temperatures, usually around 60 °C, significantly reducing the input energy and the cool-down period other higher energy methods require and, consequently, the required manufacturing time [53]. However, it is advisable to perform a rheological analysis of the inks, usually carried by a finite element software, in order to predict possible problems during the printing process, since the viscosity of the materials is lower at lower temperatures [69].

The dispensing of the ink can occur through two methods, depending on the available equipment. On one hand, the ink can be extruded from the nozzle in a continuous manner, producing a filament of ink, shown in Figure 3.9. On the other hand, the deposition of the ink can also be performed through falling ink droplets, as presented in Figure 3.10. The continuous method is indicated for objects with tighter dimensional tolerances, since the deposition of the ink is more uniform, whereas the droplet deposition of ink is more rapid and indicated for objects which do not require precision [69].

Afterwards, if the properties of the materials are to be enhanced further, the device should undergo a curing process for several hours in an oven at temperatures surrounding 250 °C [53].

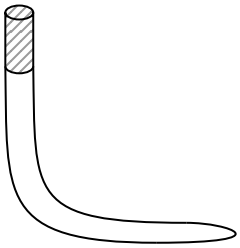

Figure 3.9: Continuous printing. Adapted from [69].

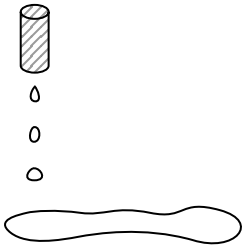

Figure 3.10: Droplet printing. Adapted from [69].

Finally, given that the thermoelectric generators are exposed to higher temperatures, the materials become damaged and oxidised over time, due to chemical reactions with air. A method of retarding the degradation of the generator material is coating its surface with an inert material that protects the generator without interfering with the thermoelectric process [73]. The protective coating, which can increase the useful life of a generator several days, are solvent-based or water-based, the former being more effective than the latter. In addition, the layer, that can be applied through a simple brushing or spraying process, has a thickness varying from 30 µm to 100 µm [74].

3.5 Simulation

Simulation is a commonly used tool to predict the behaviour of the desired thermoelectric generator in a realistic situation before producing it, reducing costs, by eliminating the need for building a prototype model and testing it in an experimental setup, as well as leading to an efficient design of the generator. The simulation revolves around using a modelling software to design the structure of the TEG, followed by its simulation in Finite Element (FE) software.

In fact, ANSYS is a commonly used software in the design and simulation of thermoelectric generators in literature, due to its multiphysic analysis of problems, accessible interface and immediate support. Using the software, it is possible to simulate the TEGs in the operative conditions. Naturally, there are simplifications and idealisations of the geometry and boundary conditions in the simulations that deviate between the obtained results and the ones which would be obtained in reality and can potentially be misleading.

ANSYS, the software used in this project, comprises several applications responsible for different parts of the simulation process. Firstly, Workbench is an application that acts as a base for the simulation process. As show in Figure 3.11, Workbench allows the analysis of various systems, such as structural, thermal, as well as thermal-electrical, essential for this project. Additionally, it is possible to perform more than one type of analysis, and ANSYS is capable of solving multiphysic problems.

As seen in Figure 3.11, the different applications are ordered the way they should be addressed and are easily accessible in the system tree. Additionally, the status of each application is visible, which is an indicator if the software has all the necessary information to perform the simulation procedures.

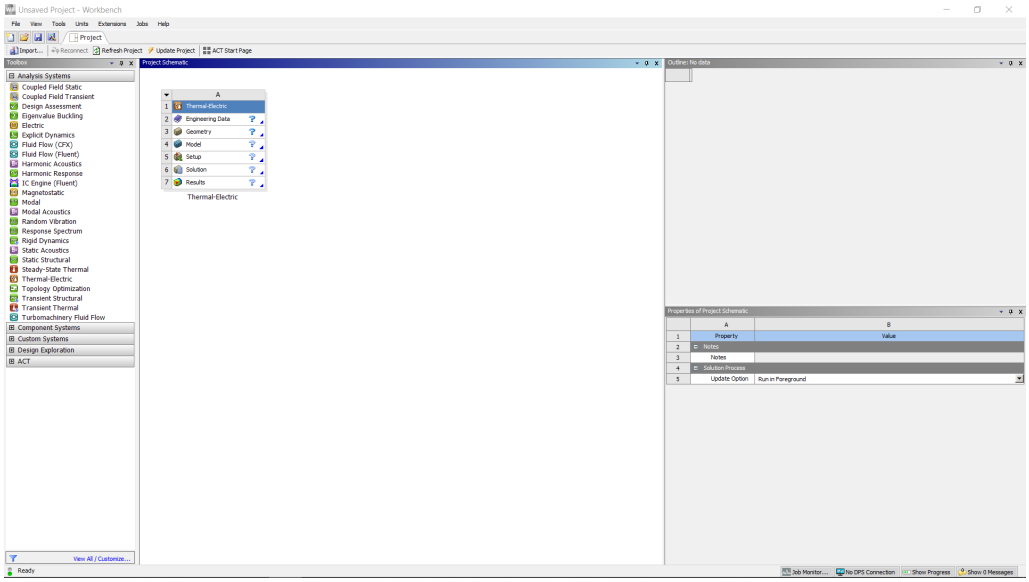

Figure 3.11: ANSYS Workbench application.

Firstly, the Engineering Data is the ANSYS application used to define the used materials and their properties. Figure 3.12 exhibits the definition of bismuth telluride.

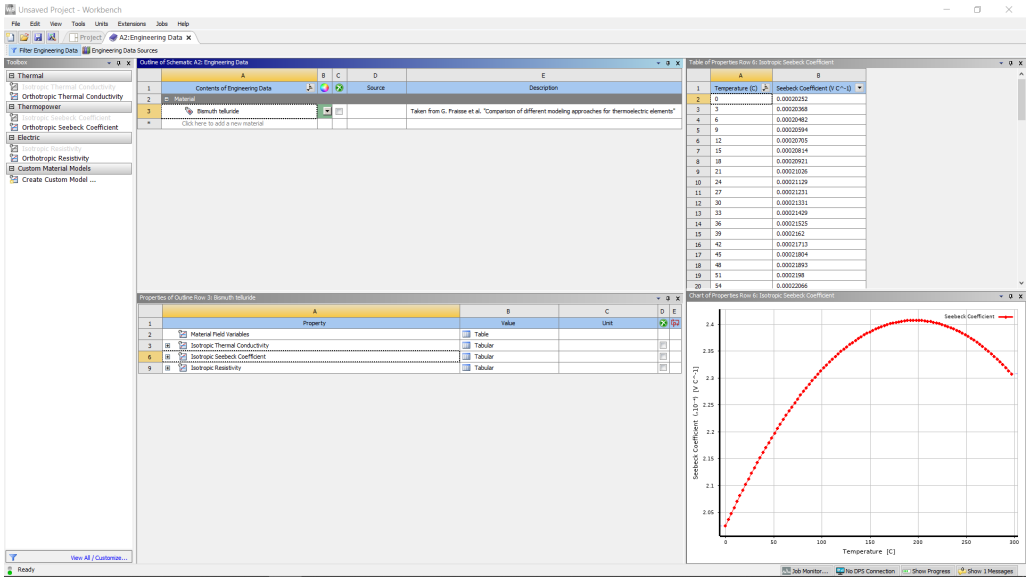

Figure 3.12: ANSYS Engineering Data application.

Since the chosen defined properties are temperature dependent, Engineering Data generates a plot of the input values in the form of a table. On the other hand, ANSYS has a material database included, which contains more commonly used materials in simulation processes.

Afterwards, the SpaceClaim application is used to model the geometry of the generator, as seen in Figure 3.13. In order to construct the three-dimensional model of the generator, each component has to be developed sequentially, and a common method is starting from a two-dimensional

sketch and afterwards extruding it into a solid, using the Pull tool. For more complex geometries, SpaceClaim possesses other building tools that could be more adequate. In addition to the design of the different components, it is also possible to establish geometric assembly conditions, such as alignment of different surfaces of different components. Furthermore, one can import files from various other design programs, such as SOLIDWORKS.

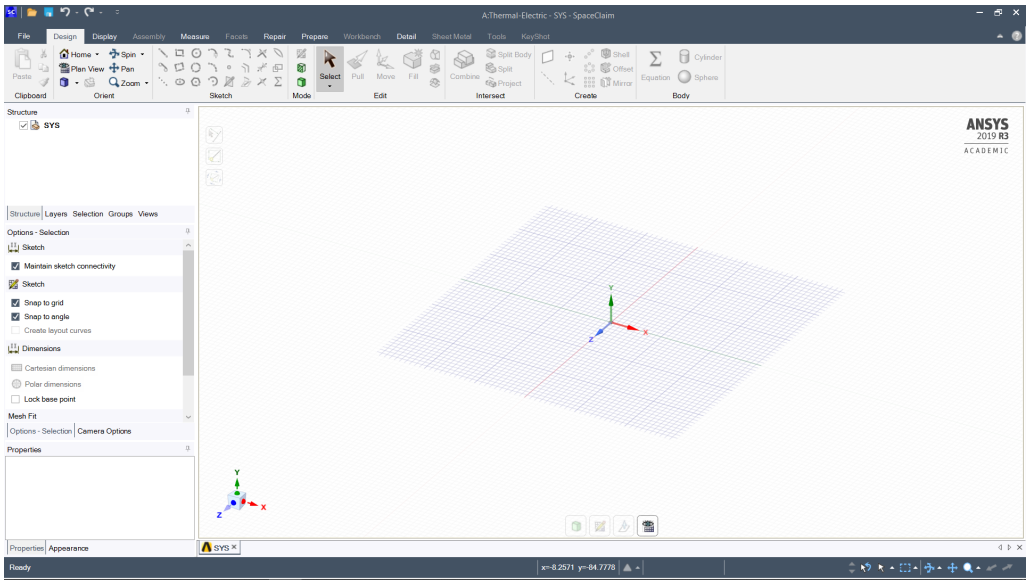

Figure 3.13: ANSYS SpaceClaim application.

Afterwards, the Mechanical application is used. This application is crucial to the definition of the simulation conditions of the model, and the presented outline tree indicates the order they must be defined in, visible in Figure 3.14. At first, it allows the association of the defined materials to the built components and the definition of the mesh used in the finite element analysis. Afterwards, the boundary conditions can be inserted, as well as the desired outcomes.

If the model had been parameterised in any parameter set in the previously shown applications, it would be possible to perform the finite element analysis parametrically, in the Parametric set, a tool of the Mechanical application, seen in Figure 3.15. In Parametric set, the input variables vary in a specified manner, and the outcome results are calculated in Workbench directly. Moreover, it is also possible to generate a plot of the obtained results, resorting to the response surface tool.

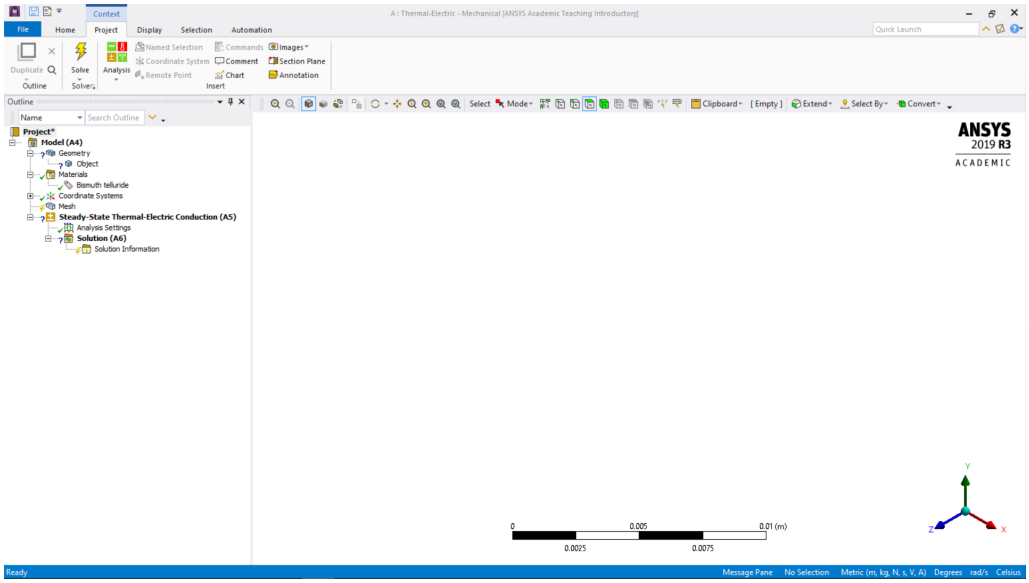

Figure 3.14: ANSYS Mechanical application.

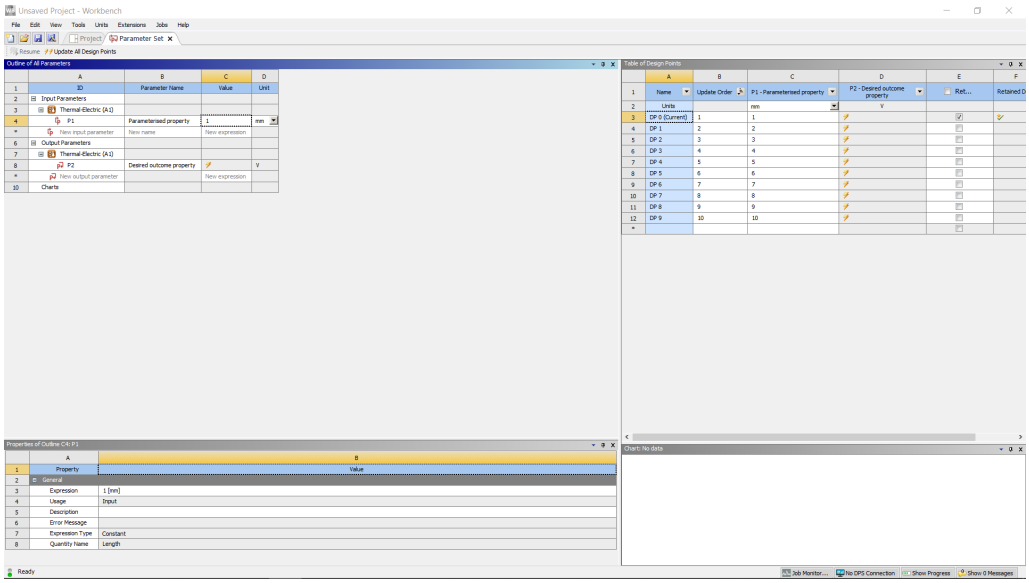

Figure 3.15: Mechanical Parametric set tool.

Chapter 4

Methodology

Already comprehending the theoretical phenomena that occur in a thermoelectric generator, as well as the current status of this technology, it is possible to proceed with the objective of this project. In this Section, the model of the TEG was designed with SpaceClaim, a design software of ANSYS 2019, and the Finite Element Method (FEM) was used to simulate the performance of the designed TEG, using ANSYS for this effect as well as for the parametric optimisation process.

The first step of the optimisation was the definition of the involved physical processes in the FEM software (Section 4.1.1), followed by the definition of the geometric parameters and the mathematical formulation of the thermoelectric properties of the materials used in each component of the TEG (Sections 4.1.2 and 4.1.3, respectively). Afterwards, the initial design of the device was achieved.

Subsequently, the numerical analysis took place resorting to the FEM. After finding a satisfactory mesh and establishing boundary conditions (in Sections 4.1.5 and 4.1.6, respectively), it was possible to obtain the temperature and voltage profiles.

Finally, to increase the feasibility of the generator, the output results needed to be maximised, which happened iteratively through the optimisation process of the defined geometrical parameters, in Section 4.3.

4.1 Simulation methodology

4.1.1 Definition of involved physical processes

As stated in Chapter 2, the stationary generation of electricity due to the existence of a temperature gradient is justified by the thermoelectric effect, into which heat transfer in solids and generation of an electrical field are encompassed. In ANSYS, the "thermal-electric" module was selected, since it is the one that best encompasses the involved phenomena.

4.1.2 Definition of global parameters

As stated previously, the efficiency of thermoelectric generators is highly influenced by its geometrical parameters, such as leg thickness, width and height, the pitch (the distance between the p- and n-type legs within a thermocouple) and the distance c, corresponding to half the distance between thermocouples. Additionally, it is important to know the impact that the height of the conductor and the thickness of the substrate layer, h_c and t_s, respectively, have in the output results.

Hence, Table 4.1 denotes the nomenclature of the defined geometrical parameters, and Figure 4.1 illustrates the technical drawing of a single TEG unit adjacent to the flexible substrate.

Table 4.1: Parameters of the model.

Nomenclature	Description
w_l	Leg width
h_l	Leg height
t	Generator thickness
p	Pitch
c	Distance between consecutive legs
h_c	Conductor height
t_s	Substrate thickness

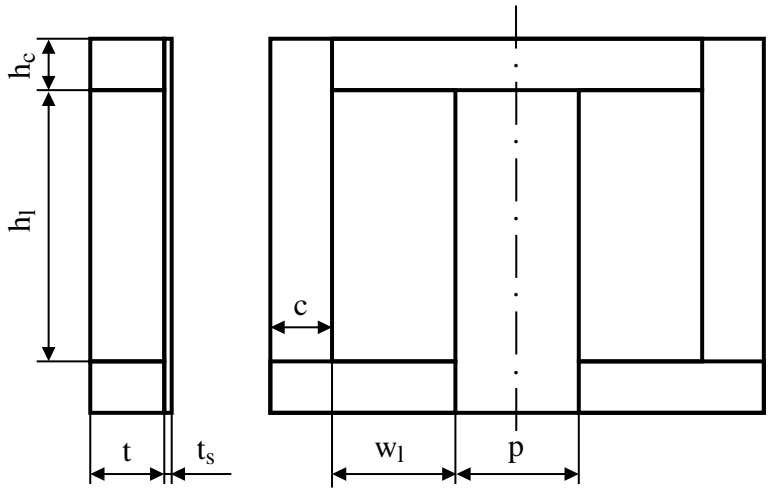

Figure 4.1: Parameterised technical drawing of a planar TEG unit.

4.1.3 Attribution of materials

The “legs” of the TEG unit are, as established before, made of a semiconductor material, and Bi_2Te_3 was chosen for being commonly used and well adapted to lower temperatures. Additionally, the bridge between the legs must be made of a highly thermal conductive material, silver being the chosen material. Finally, the unit is placed on a polymeric substrate, to have a solid

base; one of the most commonly used materials is polyimide, since its mechanical, electrical and chemical properties are ideal for the application, which is also used in this project.

Unlike silver and polyimide, bismuth telluride was not a predefined material in the material library of ANSYS. Therefore, this material was added to the library. However, since the Seebeck coefficient, the thermal conductivity and the electrical conductivity are all temperature-dependent properties of semiconductor materials, it was necessary to input the appropriate functions. Fraisse et al. (2013) approximated these thermoelectric parameters for bismuth telluride to the functions shown in Equations 4.1, 4.2 and 4.3 [75].

$$S(T) = (22224 + 930.6 \cdot T - 0.9905 \cdot T^2) \cdot 10^{-9} [\mathrm{V\,K^{-1}}] \tag{4.1}$$

$$k(T) = (62605 - 277.7 \cdot T + 0.4131 \cdot T^2) \cdot 10^{-4} [\mathrm{W\,m^{-1}\,K^{-1}}] \tag{4.2}$$

$$\sigma(T) = (5112 + 163.4 \cdot T + 0.6279 \cdot T^2)^{-1} \cdot 10^{10} [\mathrm{S\,m^{-1}}] \tag{4.3}$$

It is important to add that, for a correct simulation of real-life conditions, the n-type leg needs to have a negative Seebeck coefficient, equal in absolute value to the p-type one, equal to $S_{Bi_2Te_3}$. For that, a clone material of bismuth telluride was created, preserving every property except for the Seebeck coefficient, replaced with $-S_{Bi_2Te_3}$.

Replacing Equations 4.1, 4.2 and 4.3 in the expression to calculate the figure of merit, shown in Equation 2.21, zT of bismuth telluride can be calculated, through Equation 4.4. Figures 4.2, 4.3, 4.4 and 4.5 are plots of the four mentioned equations.

$$zT(T) = \frac{T \cdot (22224 + 930.6 \cdot T - 0.9905 \cdot T^2)^2}{10000 \cdot (62605 - 277.7 \cdot T + 0.4131 \cdot T^2) \cdot (5112 + 163.4 \cdot T + 0.6279 \cdot T^2)} \tag{4.4}$$

Through the analysis of Equation 4.4 and Figure 4.5, for the used approximation of the thermoelectric properties of Bi_2Te_3, the maximum figure of merit achieved is 0.806 at a temperature of 349 K, or approximately 76 °C.

It is noteworthy, from an analysis of the mentioned Figures, that the increase of the temperature gradient may not be beneficial to the overall performance. In fact, the Seebeck coefficient decreases for temperatures superior to approximately 470 K. From Equation 2.52, it was shown that the maximum power depends on the square of this coefficient and, therefore, the temperatures for the heat source and for the heat sink should be so that the device's performance is not adversely affected.

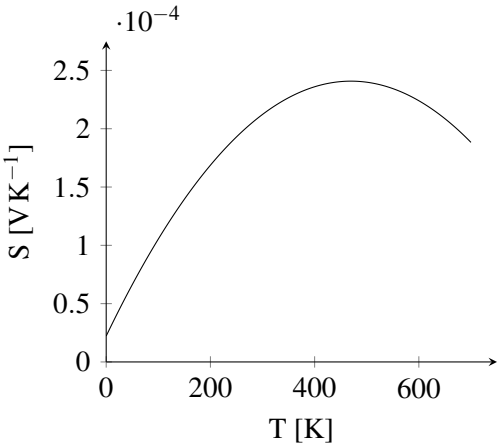

Figure 4.2: Temperature dependence of the Seebeck coefficient of Bi_2Te_3.

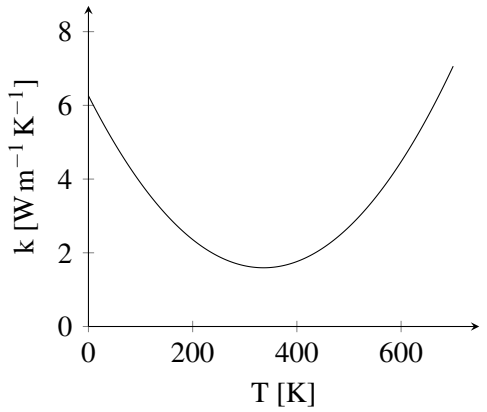

Figure 4.3: Temperature dependence of the thermal conductivity of Bi_2Te_3.

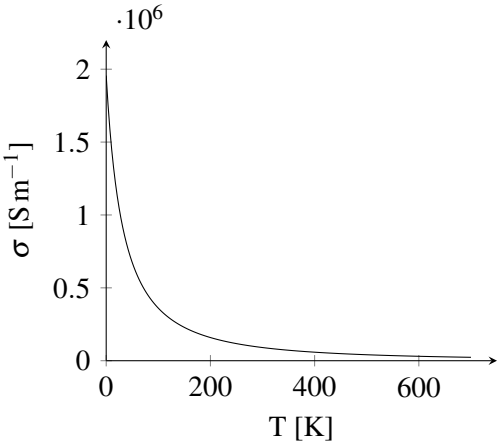

Figure 4.4: Temperature dependence of the electrical conductivity of Bi_2Te_3.

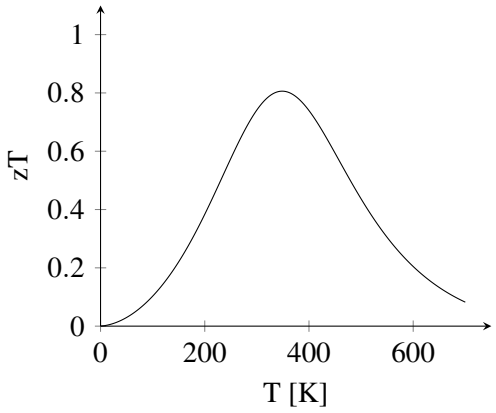

Figure 4.5: Temperature dependence of the figure of merit of Bi_2Te_3.

4.1.4 Initial design

Considering the previous aspects, the initial three-dimensional model of the planar flexible device can be constructed. The chosen dimensions mimic the design of Chen et al. (2011), which exhibited a good thermoelectric performance [53]. The design is shown in Figure 4.6 and the dimensions are shown in Table 4.2.

Table 4.2: Parameters of the initial design of the model.

Parameter	Value [mm]
w_l	0.64
h_l	5
t	0.09
p	0.36
c	0.18
h_c	0.8
t_s	0.0508

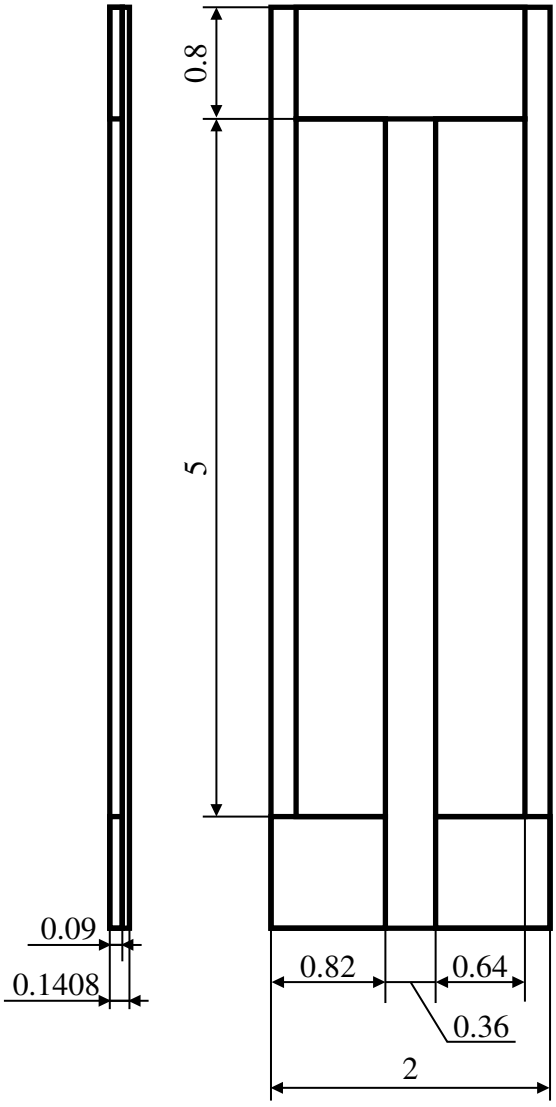

Figure 4.6: Initial design for the TEG (dimensions in millimetres). Adapted from [53].

4.1.5 Definition of mesh

The creation of a mesh is a step of the finite element method analysis, and it allows the simplification of a body into consecutive smaller polygonal bodies, in order to simplify the simulation. A greater detail of the mesh leads to more accurate results, creating a better approximation of reality, but also leads to slower processing time, undesired when the three-dimensional model is very detailed.

In this project, given the geometric simplicity of the model, a cubic mesh was chosen. For the used version of the numerical analysis software, the student version, the maximum number of elements allowed for the initial design is around 5308, which translates to an element size of 59 µm. This was the selected mesh for seemingly providing results that are the closest to reality.

In order to understand the validity of the chosen mesh and, consequently, of the obtained results, it is necessary to perform a mesh convergence study. This test is used to find the optimal combination of accuracy and computing power. In this study, ten meshes of different sizes, from coarse to refined, were applied to the model and the retrieved variables were then compared to each other to understand if the increase of the mesh quality leads to a satisfactory increase of the quality of the results. In fact, for a greater number of elements, the constant refinement may not lead to significant differences in the results, increasing the computational time unnecessarily. Table 4.3 exhibits the correlation between the size and quantity of elements for the current model.

Table 4.3: Relationship between size and quantity of elements.

Situation	I	II	III	IV	V	VI	VII	VIII	IX	X
Size [µm]	100	95	90	85	80	75	70	65	60	59
Quantity	980	1066	1247	2688	2876	3380	4032	4432	5264	5308

In the current project, the voltage was measured for meshes of different sizes. To take the mesh study a step further, three temperature gradients are going to be compared in order to understand if the mesh converges the same way from small to large temperature gradients. Maintaining the temperature of the heat sink constant and equal to 20 °C, the temperature of the heat source, T_{high}, was set as 30 °C, 260 °C and 500 °C, generating a temperature gradient of, respectively, 10 °C, 240 °C and 480 °C. Additionally, the computational time was measured, to understand its evolution with the increase of the number of elements. The output voltage and computational time for the three sets of temperature gradients are represented as a function of the number of elements in Figures 4.7, 4.8 and 4.9.

Analysing the results, it is possible to see that the voltage has a minimal variation in the three cases. In Figure 4.7, the smaller temperature gradient led to the computational time being the lowest of the three situations. Furthermore, in Figure 4.8 the computational time is higher than the previous situation, although it was for the temperature gradient of 480 °C that the computational time peaked, as seen in the graph of Figure 4.9.

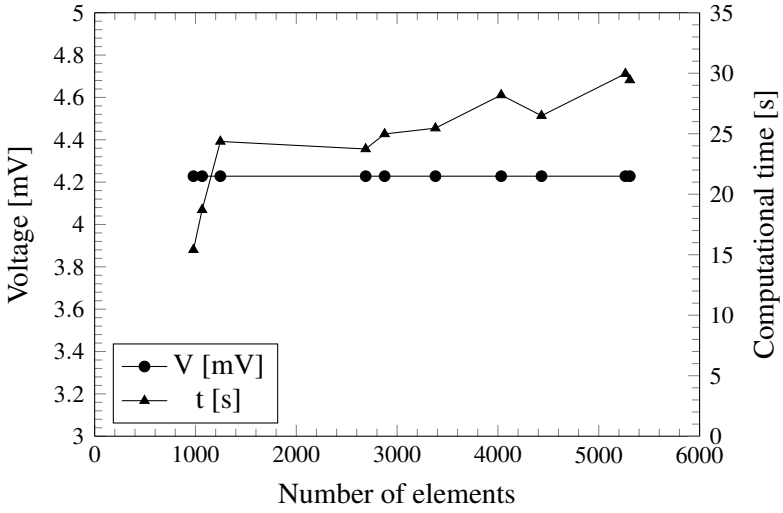

Figure 4.7: Evolution of voltage and computational time with mesh refinement for ΔT of 10 °C.

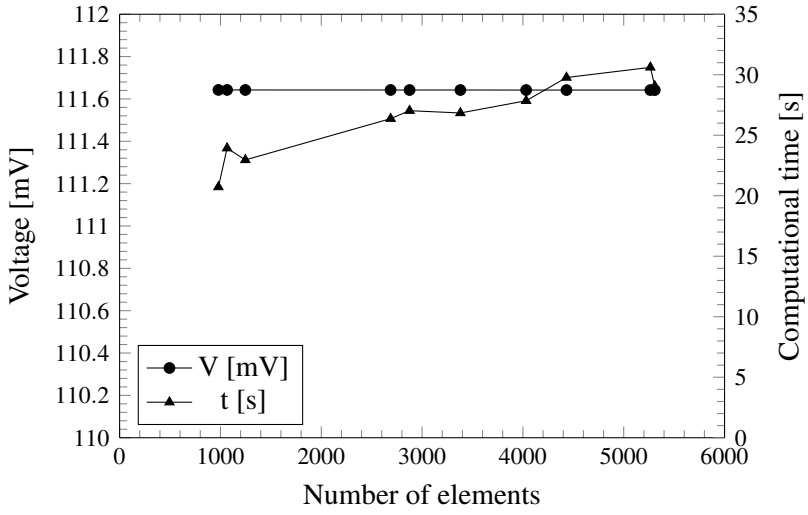

Figure 4.8: Evolution of voltage and computational time with mesh refinement for ΔT of 240 °C.

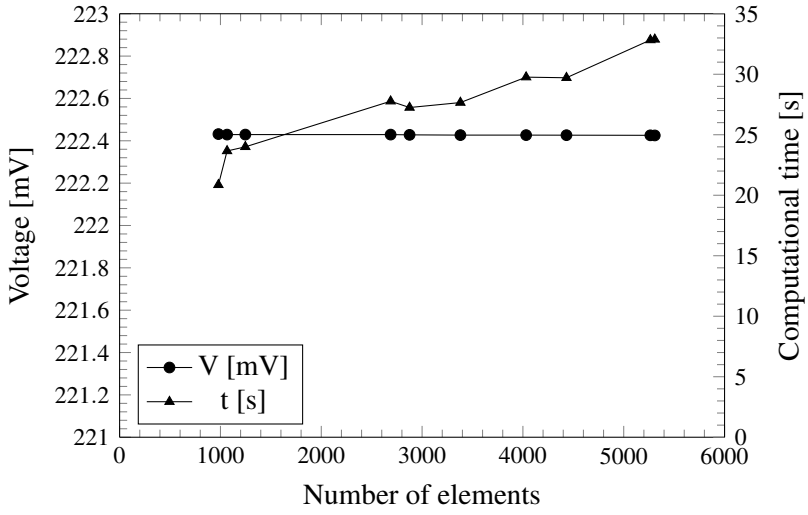

Figure 4.9: Evolution of voltage and computational time with mesh refinement for ΔT of 480 °C.

As a conclusion, the convergence test should be expanded towards finer meshes. However, given the relatively low computational time, the 59 µm sized mesh was deemed acceptable for the objectives of this project, as seen in Figure 4.10. Eventual incoherence between theoretical and numerical results is mostly due to the limitations of the student version of the used software, and could be diminished by the decrease of the element size in the finite element analysis.

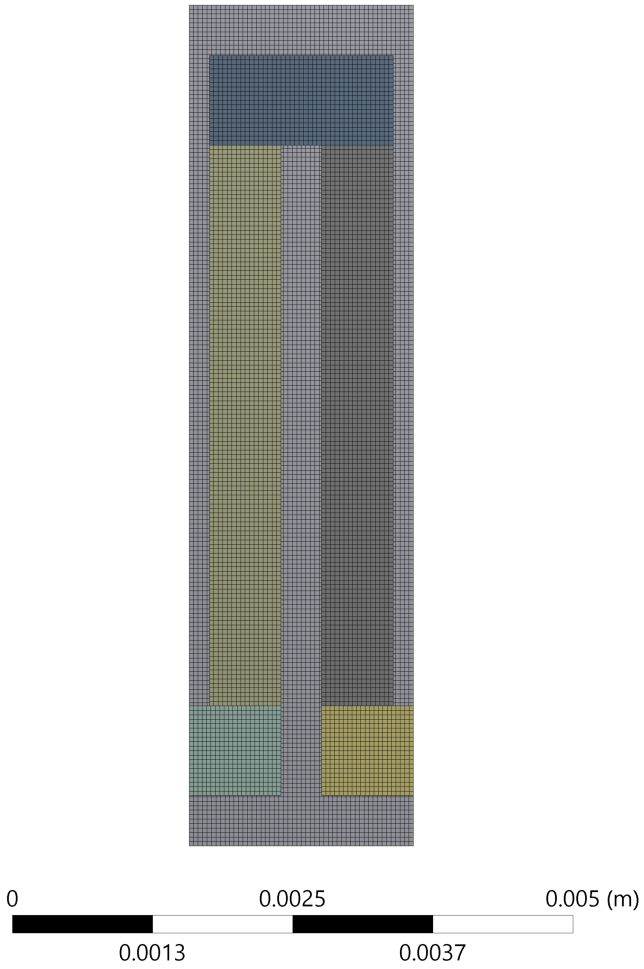

Figure 4.10: Initial design with applied mesh.

4.1.6 Definition of boundary conditions

As seen in Equation 2.1, it is mandatory to know T_{high} and T_{low} with the purpose of evaluating the produced voltage. In addition to these thermal boundary conditions, it is also important to define electrical conditions, as well as the conditions that concern to the heat transfer mechanisms, all required by the program.

Starting with the thermal boundary conditions, the temperature of the heat sink, T_{low}, was set as constant and equal to the ambient temperature of 20 °C. This temperature is applied to the bottom of the thermoelectric unit, as illustrated in Figure 4.11. For the temperature of the heat source, the top surface of the silver connector, T_{high} was set as 150°C, as shown in Figure 4.12.

Moreover, the thermoelectric unit was considered perfectly insulated in all the unmentioned remaining surfaces, meaning that no undesired heat or electricity is released through the unit, increasing its efficiency, and that the heat flow is only significant vertically. This boundary condition is clearly shown in Figure 4.13.

Lastly, the software expects the definition of one or more electrical boundary conditions. Generally, this condition is expressed by the definition of a ground condition, particularly in the surface of the thermoelectric generator that connects to the load resistance. As evidenced in Figure 4.14, a null voltage was applied to the indicated surface of the bottom left silver component. However, in case of several units connected in series, this boundary condition only applies to one of the units, particularly, the left most contact.

Every boundary condition except for the electrical one can be applied equally to every unit in a multiple unit thermoelectric generator.

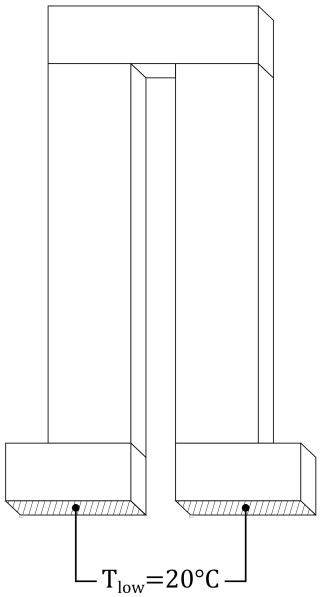

Figure 4.11: Surfaces at T_{low}.

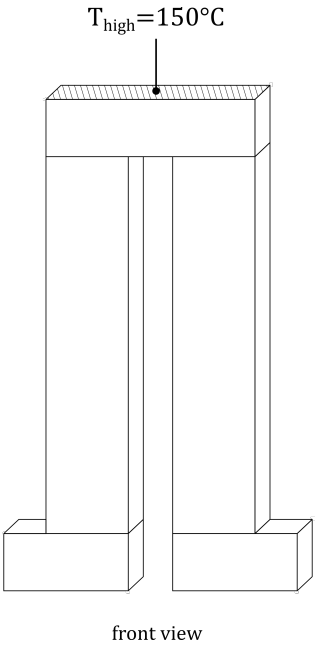

Figure 4.12: Surface at T_{high}.

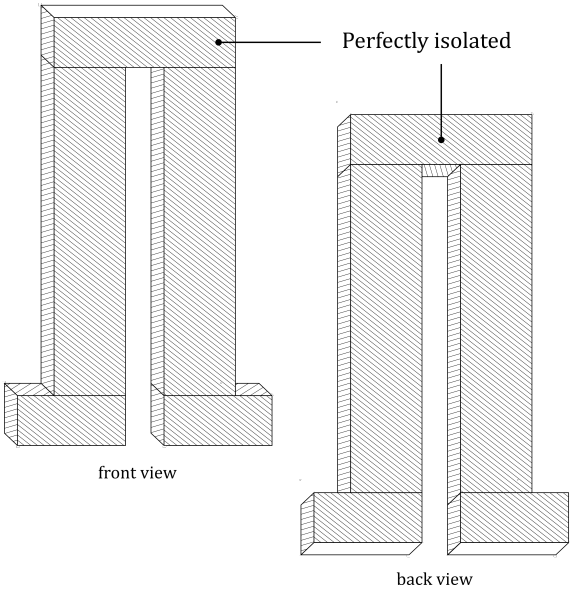

Figure 4.13: Insulated surfaces.

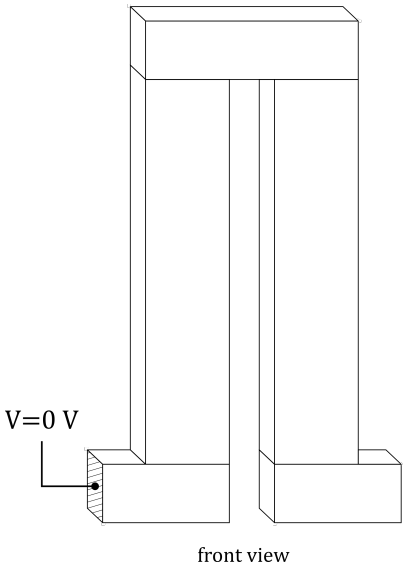

Figure 4.14: Electrical ground surface.

4.1.7 Assembly of a circuit

In order to measure electrical properties such as the current and the produced power, the TEG needs to be connected to the load resistance, whereas the voltage is measured in an open circuit. The circuit can be represented in a simple manner, as illustrated in Figure 4.15.

However, to assemble this circuit in ANSYS, it is mandatory to alter the model differently. In fact, it is necessary to create a third solid which connects the bottom contacts. This component is made from a generic material called "Load" and it only possesses the property of resistivity, ρ,

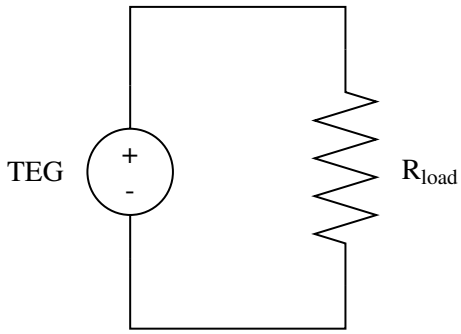

Figure 4.15: Electrical circuit used in the simulation process.

altered according to the chosen load resistance, acting as a resistance in the circuit. For instance, a generator with eight units inserted into a circuit in ANSYS is shown in Figure 4.16.

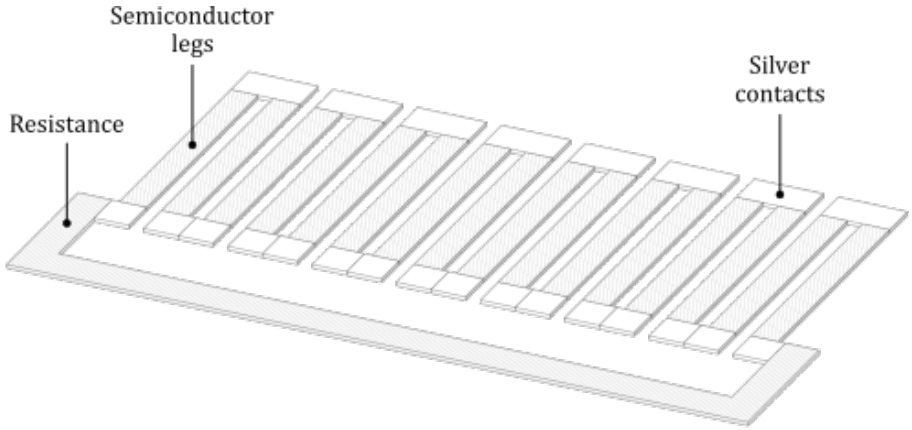

Figure 4.16: 8-unit TEG in a closed electrical circuit.

For the previous configuration, where the resistance has a constant cross-sectional area of 0.8 mm x 0.09 mm, ANSYS returns a total length of resistance equal to 20.76 mm. With these properties, the definition of the electrical resistance can be done by adapting Equation 2.27 into Equation 4.5.

$$R_{load} = \frac{\rho_{load} \cdot L_{load}}{A_{load}} \tag{4.5}$$

Preserving the geometry, the previous generator was connected to a load of varying resistance in order to find the maximum power the generator can produce. In theory, as seen previously, the optimal power occurs when the internal and the load resistances are equal, and these are the conditions in which the generators are desired to work in.

The load resistance varied between 0 Ω and 155 Ω, as a result of altering the resistivity from 0 Ωmm to 0.5 Ωmm in ANSYS, and the power and absorbed heat rate were measured for each resistance value. Later, the efficiency of the generator was calculated through the ratio of P and $\dot{Q}_{\text{high}}$. The results are shown in the graph of Figure 4.17.

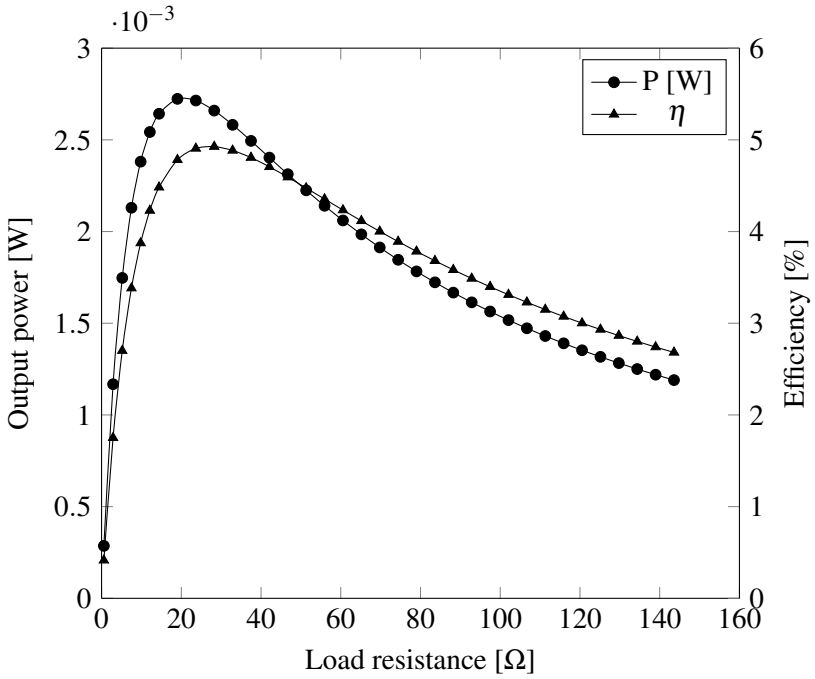

Figure 4.17: Output power and efficiency for a constant geometry and variable load resistance.

From Figure 4.17, it is seen that the maximum obtainable power is 2.724 mW, for a performance efficiency of 4.783%, when R_{load} is 19 Ω.

For the defined temperature range, the Carnot efficiency is equal to 30.7%, so it can be concluded that the initial design of the generator leads to a relatively low thermoelectric performance. If the device was working at a maximum efficiency condition, η would be equal to 4.926% when R_{load} is equal to 28.26 Ω. It is possible to confirm the assumption made in Section 2.7.3, where it was stated that the maximum power and the maximum efficiency do not occur for the same conditions.

4.2 Sensitivity analysis

For the purpose of understanding in which direction the model needs to be changed in order to be optimised, a sensitivity analysis was performed. In other words, small changes were applied to the model to understand their impact on several output variables.

To start, the number of units was altered. In fact, the increase of n in a generator leads to the increase of the semiconductor components where the thermoelectric process takes place, increasing the produced voltage, as well as the internal resistance, and both these values impact the output power, which should be maximised.

Then, the impact of the insulation of the model was analysed. In a practical scenario, the generator is coated with an inert material, acting as a protective layer of the generator, preserving

its useful life and decreasing the damage caused by thermal stress, as well as binding the generator to the flexible substrate.

On the other hand, the substrate is made from a polymeric material with low thermal conductivity and it acts as an obstacle to heat transfer due to this property, as well as decreasing the temperature dispersion [76]. Additionally, it would also work as an electric insulator, decreasing the losses to the environment and increasing the efficiency of the device. In Section 4.2.2, two main conditions were tested: a perfectly insulated model and a generator which exchanges heat with an environment at a constant temperature equal to 20 °C. For the two scenarios, the influence of the coating and substrate were studied.

Afterwards, geometrical properties were studied, in open and closed electrical circuits. As seen in Section 2.2, the produced voltage as a result of the thermoelectric process does not depend on any geometrical factors; in fact, V only depends on the TE material and the temperature gradient it is exposed to. Nonetheless, the internal resistance is affected by geometric changes, and since the electrical power depends on both, the geometry of the model must be analysed as well.

Finally, the dimensions of the conductor elements are going to be analysed. In fact, due to the high thermal conductivity, it is expected that the changes of the dimensions would not impact the performance of the generator, being the numerical simulation an easy confirmation method to prove this assumption.

In Appendix A, the different models used in this Section are presented with the complementary used mesh.

4.2.1 Number of units

The number of linked units in a generator was defined as indicated in Table 4.4, along with the used mesh size and the corresponding number of elements. The chosen size corresponds to the smallest allowed by the software version since the computational times are low.

Table 4.4: Relationship between mesh properties with the number of units.

Number of units	Mesh size [µm]	Number of elements
1	59	5308
2	88	5208
3	90	3741
4	100	3920
5	112	3940
6	128	3537
7	134	3794
8	150	3824
9	160	3710

As one would expect, the increase of the number of units leads to an increase of the elements to analyse, and understanding the limitations of the finite element analysis software, it was expected for the minimum size allowed to increase as well.

The output results, such as the open-circuit voltage and the absorbed heat rate on the surface in contact with the heat sink, at temperature T_{high} defined in Section 4.1.6, $\dot{Q}_{high}$, were transported into a scatter plot. These plots are represented in Figure 4.18 and Figure 4.19, respectively, as a function of the number of units defined for a each module.

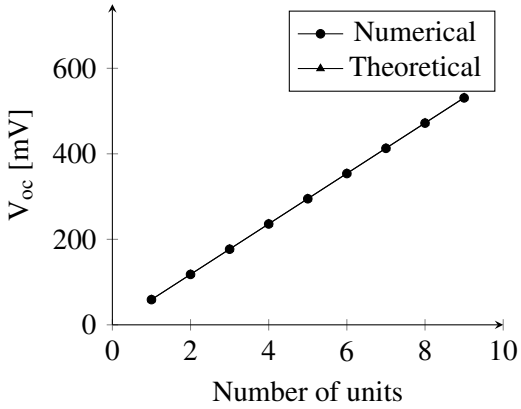

Figure 4.18: Open-circuit voltage as a function of the number of units in an open-circuit module.

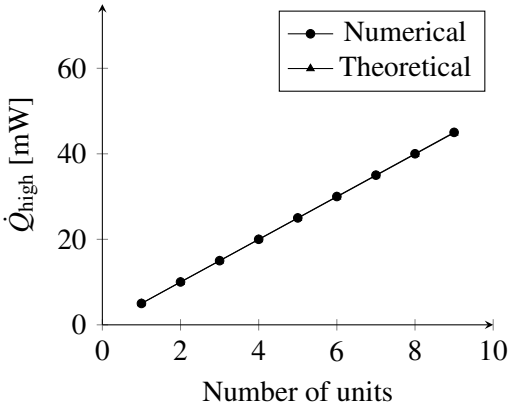

Figure 4.19: Absorbed heat rate as a function of the number of units in an open-circuit module.

As seen in Figure 4.18, the voltage has a linear behaviour. In other words, the output voltage is proportional to the number of units, as indicated by the theoretical principles. Similarly, the absorbed heat rate is also proportional to the amount of units in series, since the electrical resistivity and the thermal conductivity follow the same logic as the Seebeck coefficient.

The simulated and theoretical values of V_{oc} and $\dot{Q}_{high}$ differ by a 0.1% error, which means the simulation results are acceptable.

On the other hand, the 9 different models were integrated in a circuit, each connected to a resistance with variable R_{load}, in order to find the optimum value which leads to the maximum output power of the system. The measured output variables, P, $\dot{Q}_{high}$ and η, are represented as a function of the number of units and the load resistance in Figure 4.20, Figure 4.21 and Figure 4.22, respectively. From the Figures, the maximum output power and corresponding absorbed heat rate and efficiency were calculated, and represented as a function of n in Figure 4.23, Figure 4.24 and Figure 4.25, respectively. As previously explained, the condition of maximum power occurs when the load resistance is equal to the internal resistance.

From these graphs, it is possible to take several conclusions. First of all, looking at Figure 4.20, Figure 4.21 and Figure 4.22, the nine curves are similar in shape in each graph, meaning the evolution of the output parameters and the load resistance is equal regardless of the number of units.

On the other hand, by evaluating Figure 4.20, it is noticeable that the maximum power occurred for different values of R_{load}, both properties increasing with the number of units. In Figure 4.23, it is apparent that the maximum power and number of generator units evolve linearly, since both $\dot{Q}_{high}$ and V_{oc} have a linear behaviour, as evidenced by Figure 4.24 and Figure 4.18, respectively.

Similarly, as visible in the graph of Figure 4.21, the rate of the heat absorbed from the heat source decreased with the increase of the load resistance. Additionally, comparing with the obtained open-circuit values, the generator required a higher absorbed heat rate from the heat source, as it was predicted by Equation 2.33 and Equation 2.43.

In addition, according to the results shown in Figure 4.22, the efficiency of every generator peaked at different values of R_{load}, but this parameter never exceeded 5.63%. Looking at Figure 4.25, the efficiency for the optimum conditions of power generation can also be considered independent of the number of units in the generator, and equal to 5.5%. The efficiency of a thermoelectric generator mostly depends on the materials and working temperature range, so the oscillations in the obtained values could be minimised with a more detailed mesh.

Therefore, it is possible to conclude that the simulation results were in accordance with the theoretical principles, and that the increase of the number of units in a thermoelectric generator would positively increase the obtainable power.

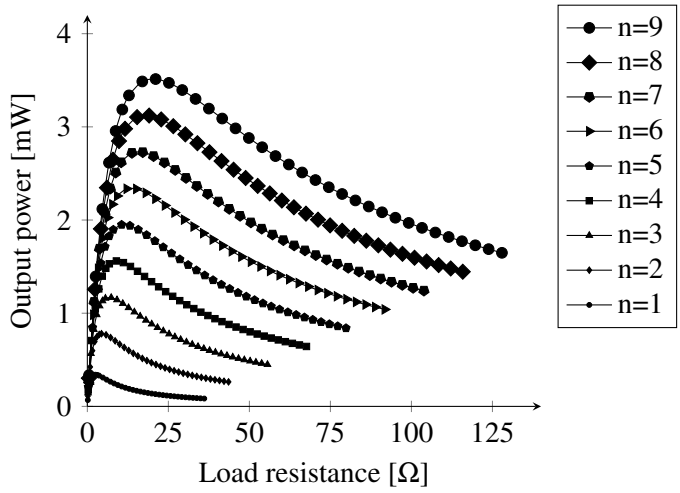

Figure 4.20: Output power for a constant geometry and variable n and R_{load}.

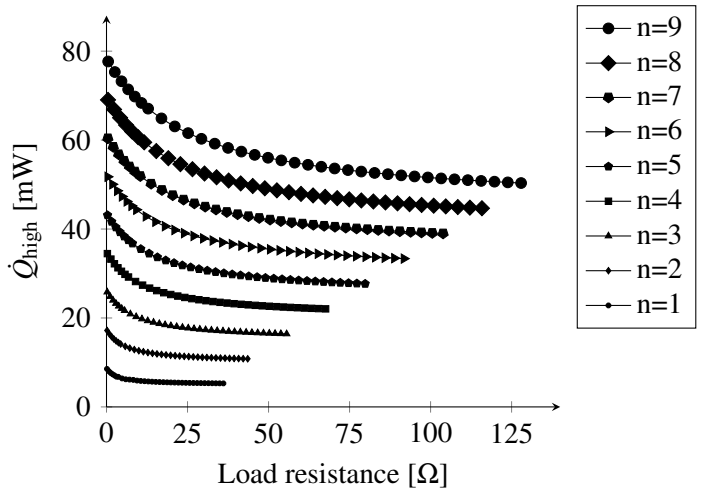

Figure 4.21: Absorbed heat for a constant geometry and variable n and R_{load}.

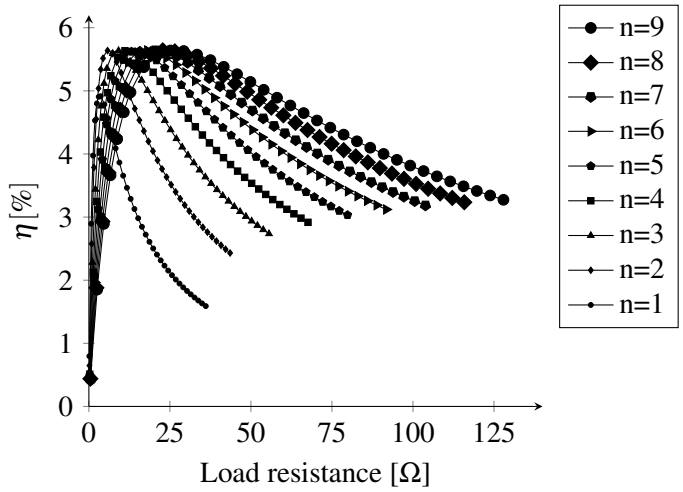

Figure 4.22: Efficiency for a constant geometry and variable n and R_{load}.

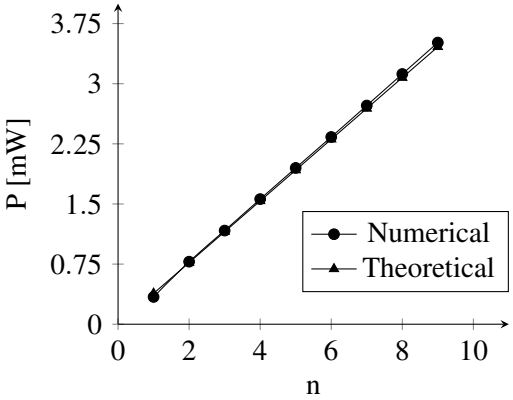

Figure 4.23: Evolution of the maximum output power as a function of the number of units in a closed circuit.

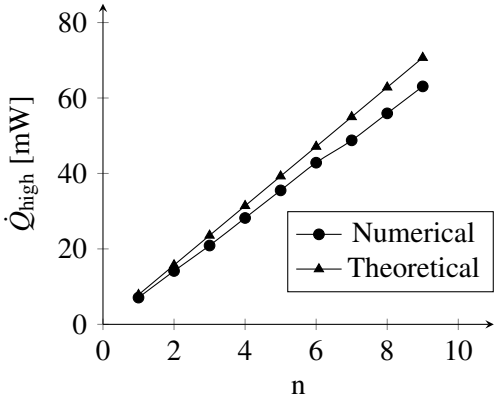

Figure 4.24: Evolution of the absorbed heat rate as a function of the number of units in a closed circuit.

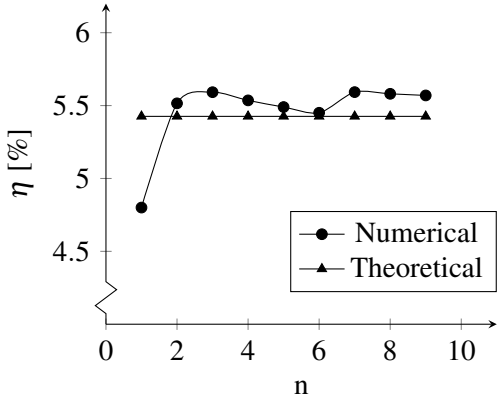

Figure 4.25: Evolution of the efficiency as a function of the number of units in a closed circuit.

4.2.2 Insulated model

Thermoelectric generators are exposed to elevated temperatures, resulting in the degradation of their materials. The deterioration of the generators is due to several chemical reactions with the environment, such as oxidation or sublimation. Although it is possible to improve the endurance of these materials with nanotechnology, according to Brostow et al. (2012), there are two easier possible ways to decelerate the degradation, such as surrounding the generator with an insulator filling and covering it with a thin coating layer of a protective material [73]. Given that the first presented solution is, for the current project, impractical due to the limited available space, the coating of the generator becomes the used tool to protect the materials.

In this Section, the chosen coating material was boron nitride, a commonly used inorganic material, integrated in a coating solution which protects surfaces from oxidation at elevated temperatures. The coating possesses an electrical resistivity of $1 \cdot 10^{14}\,\Omega\,\mathrm{m}$ [77] and an estimated thermal conductivity of $500\,\mathrm{W\,m^{-1}\,K^{-1}}$ [78].

The model was inserted into three environments, where the room temperature was set at 0 °C, 20 °C (which is equal to T_{low}) and 40 °C. Additionally, the condition of perfect insulation was removed, and a natural convection situation was installed, with a convection coefficient, equal to $5\,\mathrm{W\,m^{-2}\,K^{-1}}$, a typical value for natural convection. Moreover, the presence of the coating was analysed, and several thickness values of the protective layer were considered, specifically 0 µm, which translates to an uncovered model, 30 µm, 60 µm and 90 µm. Applying a 59 µm mesh on the model, the simulation process took place and, for the conditions of maximum power, the output parameters were calculated and are presented in Table 4.5.

Table 4.5: Impact of the coating on the thermoelectric performance.

T [°C]	Coat thickness [µm]	P [mW]	$\dot{Q}_{high}$ [mW]	η [%]
0 °C	0	0.366	14.89	2.46
	30	0.343	79.20	0.43
	60	0.325	142.4	0.23
	90	0.322	204.9	0.16
20 °C	0	0.362	13.73	2.63
	30	0.343	78.05	0.44
	60	0.325	141.1	0.23
	90	0.322	203.6	0.16
40 °C	0	0.357	12.57	2.84
	30	0.340	76.58	0.44
	60	0.325	139.8	0.23
	90	0.322	202.3	0.16

As seen in Table 4.5, the increase of the ambient temperature was responsible for the reduction of the produced power. In addition, the presence of the coating layer generated a slight decrease of the produced power of the generator, but it had a significant impact on the absorbed heat rate from

the heat source and, consequently, the efficiency. In fact, the coating adds a thermal resistance to the generator, and the increase of its thickness leads to a higher thermal resistance and, therefore, to lower dissipated heat, as shown in Equation 2.19.

4.2.3 Substrate material and thickness

As seen previously, the substrate material must be flexible and be able to withstand higher operating temperatures, while having low values of thermal conductivity, to reduce dissipated heat into the environment. In this Section, a thermal analysis of the substrate was done, by integrating a thermoelectric unit in the optimal closed circuit (where the load and the internal resistances were equal) in three environments set at 0 °C, 20 °C and 40 °C each. Additionally, similarly to Subsection 4.2.2 the condition of perfect insulation was replaced with a natural convection condition, with a convection coefficient of $5\,W\,m^{-2}\,K^{-1}$.

Additionally, the thickness of the substrates, t_s, was changed, in order to understand the impact of this dimension in the heat transfer perpendicular to the heat flow in the model.

The measure parameter was the heat flux, and the obtained results are presented in Table 4.6 and Table 4.7, for a substrate made of polyimide and cotton, respectively.

Table 4.6: Impact of polyimide substrate thickness in the thermoelectric performance.

T [°C]	t_s [mm]	$\dot{q}$ [$W\,m^{-2}$]
0 °C	0.0508	1935.638
	0.1016	1935.638
	0.1524	1935.638
20 °C	0.0508	1704.536
	0.1016	1704.536
	0.1524	1704.536
40 °C	0.0508	1619.038
	0.1016	1619.038
	0.1524	1619.038

Comparing the obtained results shown in Table 4.6 and Table 4.7, it is possible to conclude that the cotton substrate absorbs less heat than the polyimide, since the former has a lower thermal conductivity than the latter. Additionally, the thickness of the substrate did not influence the output results. Finally, the increase of the environment temperature resulted in a decrease of the dissipated heat to the substrate.

Table 4.7: Impact of cotton substrate thickness in the thermoelectric performance.

T [°C]	t_s [mm]	$\dot{q}$ [W m^{-2}]
0 °C	0.0508	1647.305
	0.1016	1647.305
	0.1524	1647.305
20 °C	0.0508	1431.315
	0.1016	1431.315
	0.1524	1431.315
40 °C	0.0508	1215.428
	0.1016	1215.428
	0.1524	1215.428

4.2.4 Unit thickness

Planar thermoelectric generators are thin structures, and their thickness is conditioned by the manufacturing process. In particular, the dispenser printing machines are keen on providing more customisation to the product because they have several nozzles with different dimensions.

In this Section, while maintaining every other dimension, the thickness of the legs and conductive connections of a single unit were altered, in order to understand if the use of a different nozzle in the dispenser machine can significantly impact the output parameters. The thickness of the model was changed between 100 µm and 500 µm in intervals of 50 µm. The results were measured and are presented in Figure 4.26 and Figure 4.27.

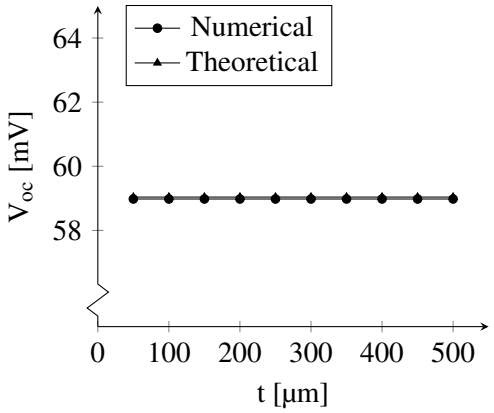

Figure 4.26: Open-circuit voltage as a function of the model thickness in an open-circuit module.

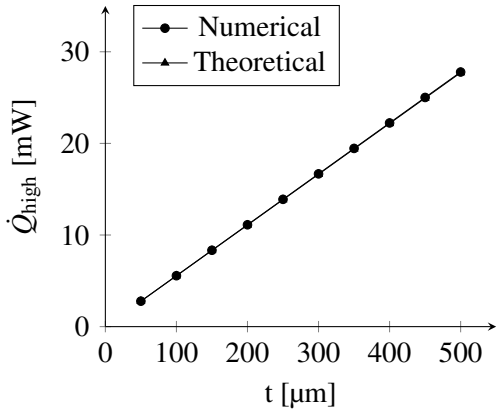

Figure 4.27: Absorbed heat as a function of the model thickness in an open-circuit module.

Observing the results, it is evident that the open-circuit voltage is not affected by the geometric parameters. In addition, the increase of the thickness of the generator and, proportionally, of the cross-sectional area led to the increase of the absorbed heat rate.

In a closed circuit for optimum resistance values, as seen from Figure 4.28, Figure 4.29, and

Figure 4.30, the output power, absorbed heat rate and efficiency were measured for the chosen values of the thickness of the model, respectively.

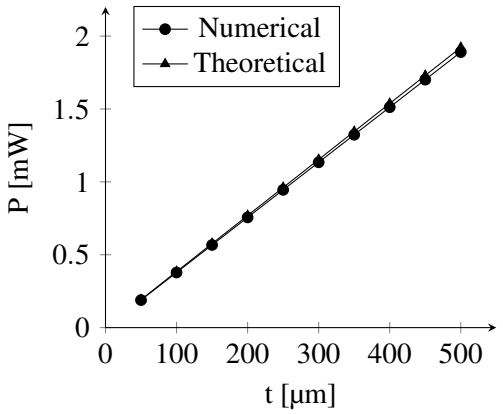

Figure 4.28: Evolution of the maximum output power and the model thickness.

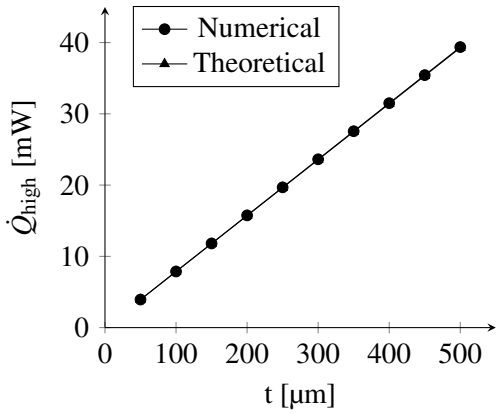

Figure 4.29: Evolution of the absorbed heat rate and the model thickness.

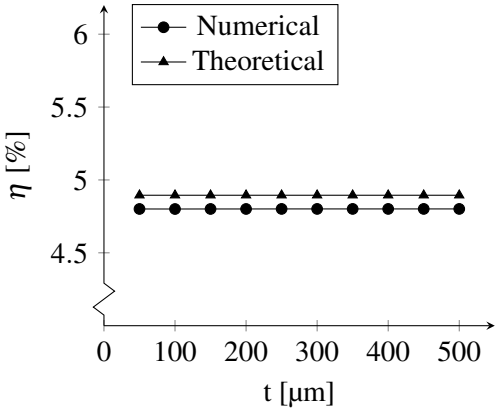

Figure 4.30: Evolution of the efficiency for maximum power and the model thickness.

Similarly to the results presented in Section 4.2.1, the power and absorbed heat rate exhibit a linear behavior with the increase of the thickness of the model. Additionally, according to the results shown in Figure 4.30, the efficiency at maximum power conditions was constant and equal to 4.80%.

Hence, it can be concluded that the simulation results could have been predicted by the theoretical equations, and the increase of the thickness of the model could lead to the increment of the output power.

4.2.5 Leg dimensions

As mentioned in Section 2.6.1.1, altering the cross-sectional area and length of the semiconductor legs is essential to optimising the performance of the generator. Firstly, the leg height was

analysed. For a unit, this parameter varied from 1 mm to 10 mm in intervals of 1 mm. As before, the open-circuit voltage and absorbed heat rate were measured and afterwards, the optimum load resistance was obtained for each case, and Figure 4.33, Figure 4.34 and Figure 4.35 show the maximum obtainable power and $\dot{Q}_{high}$ and η in the same state, respectively.

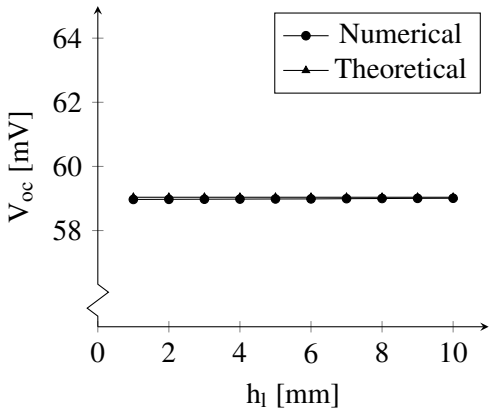

Figure 4.31: Open-circuit voltage as a function of leg height in an open-circuit module.

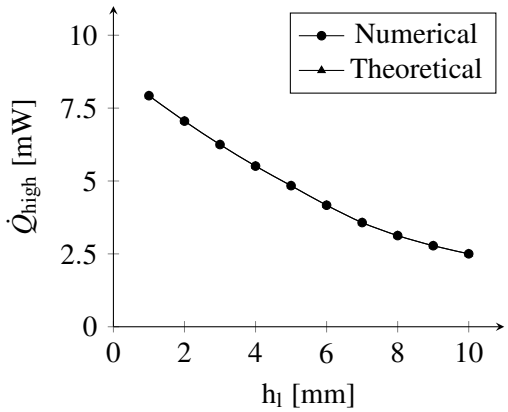

Figure 4.32: Absorbed heat as a function of leg height in an open-circuit module.

As seen previously, the increase of the height of the thermoelectric legs leads to the increase of the internal resistance of the generator, reducing the current as can be confirmed from the analysis of Equation 2.39. In fact, as seen from Equation 2.4, it is evident that the power depends on the square of the current, so a small decrease of the current can lead to significant changes to the former electrical property [79].

In order to alter the cross-sectional area of the legs, the width and the thickness can be altered individually or simultaneously. Preserving the thickness of the generator, the width of the legs of a single unit was altered between 0.1 mm to 0.8 mm in intervals of 0.1 mm. The silver top conductor was adjusted to fit the width of the two legs and the constant pitch. Respectively, the values of the open-circuit voltage and absorbed heat rate that were obtained are presented in Figure 4.36 and Figure 4.37.

With the obtained results of Section 4.2.4 and the ones in Figure 4.36 and Figure 4.37, it is possible, and maybe more interesting, to show the output parameters as a function of the cross-sectional area of the legs. Combining the results, where A ranged from 0.009 mm^2 and 0.32 mm^2, the voltage was not altered, the output power increased linearly and the efficiency remained constant.

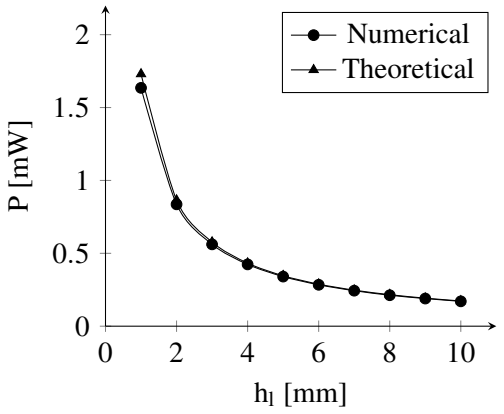

Figure 4.33: Evolution of the maximum output power as a function of the leg height in a closed circuit.

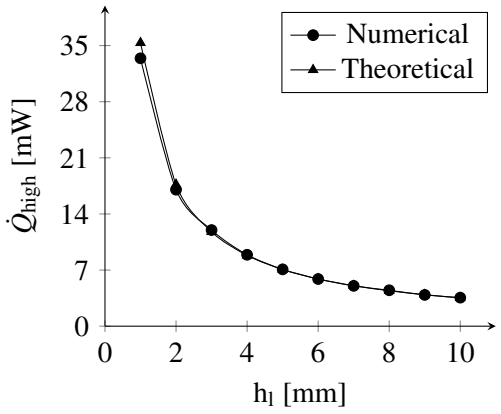

Figure 4.34: Evolution of the absorbed heat rate as a function of the leg height in a closed circuit.

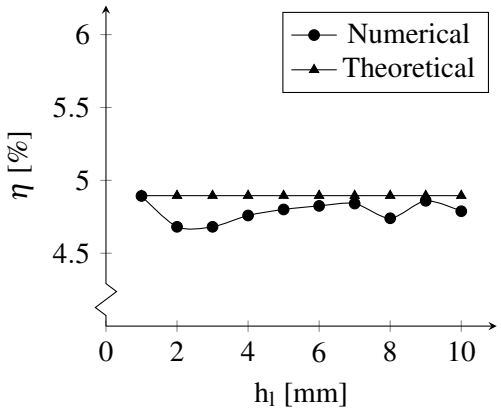

Figure 4.35: Evolution of the efficiency as a function of the leg height in a closed circuit.

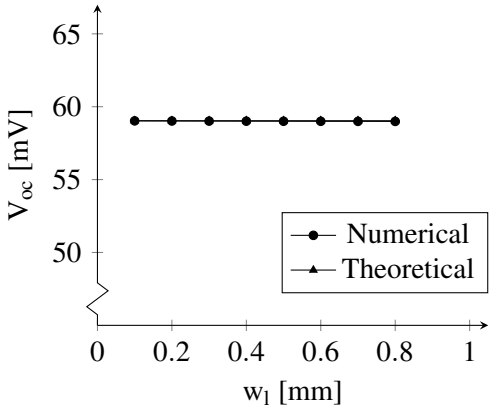

Figure 4.36: Open-circuit voltage as a function of leg width in an open-circuit module.

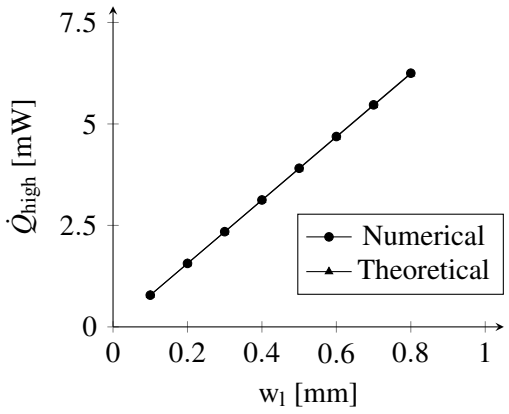

Figure 4.37: Absorbed heat as a function of leg width in an open-circuit module.

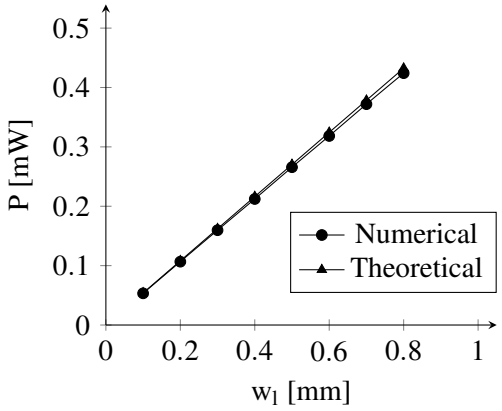

Figure 4.38: Evolution of the maximum output power as a function of the leg width in a closed circuit.

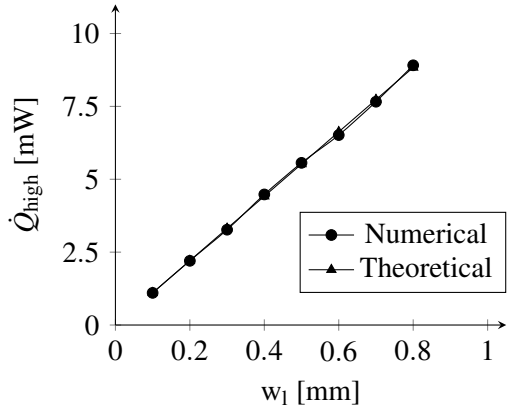

Figure 4.39: Evolution of the absorbed heat rate as a function of the leg width in a closed circuit.

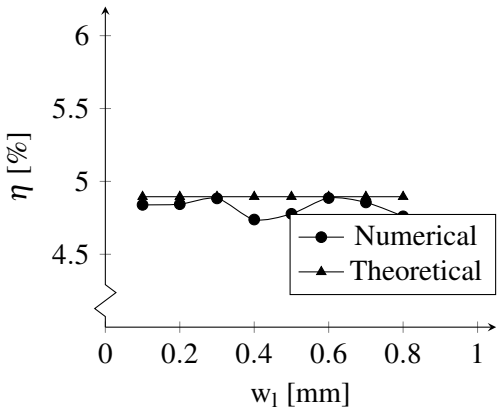

Figure 4.40: Evolution of the efficiency as a function of the leg width in a closed circuit.

4.2.6 Conductor dimensions

To end the sensitivity analysis, a study of the height and width of the silver conductors took place. These conductors serve as bridges between consecutive units, and their dimensions could affect the performance. Firstly, the height of the conductor elements was altered, ranging from 0.8 mm to 9.8 mm in equal intervals of 1 mm. In an open-circuit, V_{oc} and $\dot{Q}_{high}$ were measured and their values are represented in the graphs of Figure 4.41 and Figure 4.42, respectively.

Additionally, the parameter c and pitch were altered simultaneously. In order to change the distance between consecutive legs, the width of the bottom conductors changed from 0.82 mm to 5.82 mm and, in parallel, the width of the top conductor switched between 1.64 mm and 6.64 mm, both in equal intervals of 0.5 mm. Through the simulation process, V_{oc} and $\dot{Q}_{high}$ were measured and the results are presented in Figure 4.43 and Figure 4.44, respectively.

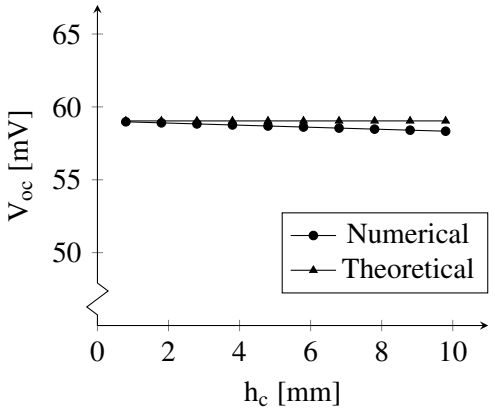

Figure 4.41: Open-circuit voltage as a function of conductor height in an open-circuit module.

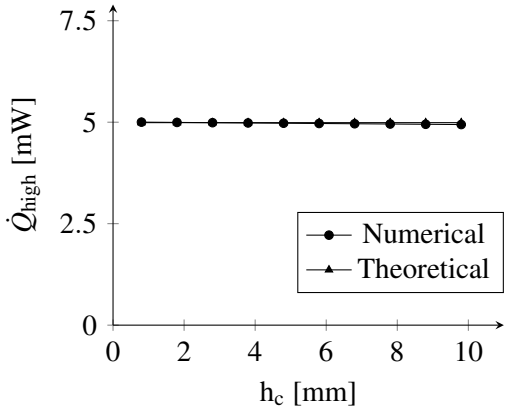

Figure 4.42: Absorbed heat as a function of conductor height in an open-circuit module.

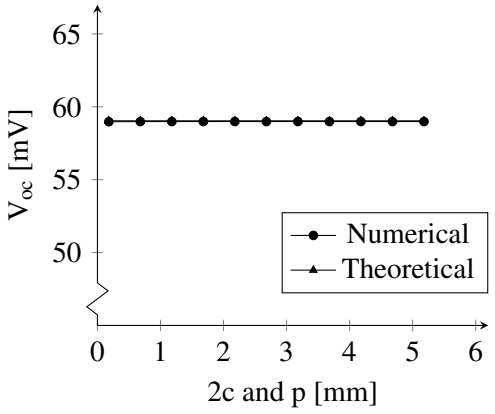

Figure 4.43: Open-circuit voltage as a function of conductor width in an open-circuit module.

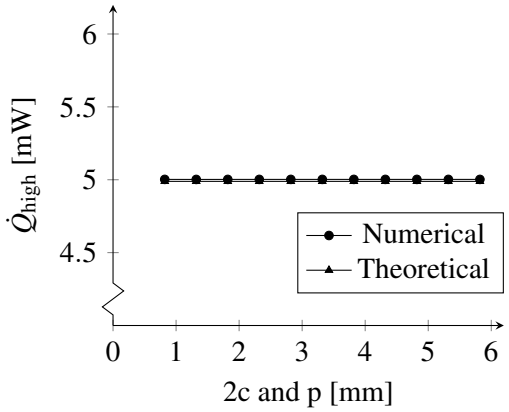

Figure 4.44: Absorbed heat as a function of conductor width in an open-circuit module.

Looking at the results, it can be observed that the height and width of the conductors did not impact the open-circuit voltage or heat transfer from the heat source. As shown previously, the heat-electricity conversion process is not affected by geometrical parameters. Additionally, the high levels of thermal conductivity of silver, approximately equal to $419\,W\,m^{-1}\,K^{-1}$ at room temperature, are far superior than the conductivity of bismuth telluride, which, in room temperature conditions, is roughly equal to $217\,W\,m^{-1}\,K^{-1}$. Hence, the magnitude of the thermal conductivity of silver leads to geometrical adjustments of the conductors to be negligible.

4.3 Optimisation methodology

Already visualising the implications of geometrical adjustments, it is finally possible to optimise the device, by establishing the conditions the generator is designed to work in.

In fact, the real thermoelectric generator is meant to power a device in a closed circuit. It is assumed that the device requires a minimum of 0.1 W and consumes an exact voltage of 5 V. Additionally, the generator is limited to a 10 cm x 10 cm area. Moreover, the thickness of the thermoelectric generator was fixed at 90 µm, conditioned by the dispensing valve of the available dispenser printer, as well as the substrate thickness equal to 50.8 µm made from polyimide. The constraints are condensed in Table 4.8.

Table 4.8: Thermal, geometrical and electrical constraints.

Thermal constraints	
Property	Value
T_{high}	150 °C / 423.15 K
T_{low}	20 °C / 293.15 K

Geometrical constraints	
Property	Value
A_{max}	10 cm x 10 cm
t	90 µm
t_s	50.8 µm

Electrical constraints	
Property	Value
V_{load}	5 V
P_{min}	0.1 W

The optimisation problem could be solved through a mathematical model. In fact, the mathematical formulation of an optimisation problem revolves around the definition of an objective function to be minimised or maximised and the existing constraints, in the form of either equality constraints or inequality constraints. Therefore, the current optimisation problem can be described with the Equations encompassed in Table 4.9, where the defined objective function is the difference between the internal and the load resistances, which should be minimised as much as possible, and the constraints translate the ones defined in Table 4.8.

Table 4.9: Formulation of the mathematical optimisation model.

minimise	$(R_{int}\text{-}R_{load})$
subject to	$T_{high} = 150\,°C$
	$T_{low} = 20\,°C$
	$A \leq 10\,cm x 10\,cm$
	$t = 90\,\mu m$
	$t_s = 50.8\,\mu m$
	$V_{load} = 5\,V$
	$P \geq 0.1\,W$

As seen in the previous sections, changing the number of units and the dimensions h_l and w_l of the legs is the best way to optimise the generator. Additionally, the parameter A_l/h_l, also represented as γ_l, was created, and it represents the ratio between the cross-sectional area of the legs and their height. Understanding that the thickness of the generator is always constant, γ_l can easily be converted into w_l/h_l of the thermoelectric legs. This way, one single parameter can symbolise two dimensions of the generator at once, facilitating the parametric optimisation process, specifically when the impact the number of units has on the power is being studied.

The parametric optimisation of the thermoelectric generator was done using two methods: theoretical and numerical. In order to create the theoretical optimisation process, several equations of Section 2.7 were applied in an EXCEL sheet and the Solver tool was used to obtain the final design of the generator considering the evidenced constraints in Table 4.8. In Appendix B, the used EXCEL spreadsheet is shown.

On the other hand, the optimised design obtained in the theoretical optimisation process can be verified resorting to a simulation software which uses finite element methods to solve the equations. In ANSYS, it is possible to parameterise several types of variables and, for the parametric optimisation of this particular project, specific variables of different natures were parametrised.

Firstly, the dimensions of the thermoelectric components was parametrised. Through the use of the Pull tool in SpaceClaim, which is able to extrude a solid a specified distance in any direction, the parameterisation of all dimensions is possible. Particularly, the width and the height of the legs were parametrised. In order to reduce the computational processing time, the geometric proportion of the silver contacts of the initial design were kept, since changes in their dimensions have a minimal impact on the performance of the generator, as evaluated in Section 4.2.6. In order to preserve the disposition of the generator, SpaceClaim allows the assembly of the different components and the definition of alignment conditions between two surfaces or objects. This way, the generator geometry is constantly updated to preserve its general configuration regardless of the applied changes.

Furthermore, in SpaceClaim, it is also possible to choose the number of objects present in one-dimensional array and parameterise such value. However, due to the complexity of altering the geometry of the resistance to preserve the configuration and the contact with the terminals of the generator, the number of units was manually changed, and the resistance adapted. Had the increase

of the number of units been accounted for in the numerical optimisation, the resistivity of the load would need to be parametrised in Engineering Data. In fact, since the resistance component in ANSYS possesses a constant cross-sectional area, in order to maintain the desired load value, there is a balance that needs to occur between the resistivity value and the changing resistance length, as seen in Equation 4.5.

Therefore, in total, it was only necessary to parametrise the height and the width of the thermoelectric legs, since the remaining properties were dependent on these variables. Table 4.10 presents the parametrised variables and their defined boundaries.

Table 4.10: Parametrised variables and their numeric limits.

Property	Lower bound	Upper bound	Increments
n	100	800	70
w_l	$1 \cdot 10^{-3}$ mm	5 mm	$1 \cdot 10^{-3}$ mm
h_l	$1 \cdot 10^{-3}$ mm	10 mm	$1 \cdot 10^{-3}$ mm

Through the combination of the different possible input values, ANSYS performed the parametric analysis and the data was collected and analysed in EXCEL, namely the maximum obtained open-circuit voltage, the absorbed heat rate from the heat source and the one rejected to the heat sink.

Chapter 5

Results and discussion

In this Section of the thesis, the parametric optimisation results, obtained via a theoretical and a numerical model are shown in Section 5.1 and Section 5.2, respectively, and their values were compared. Additionally, the final design is shown and discussed in Section 5.3.

5.1 Theoretical parametric optimisation results

Firstly, it is possible to obtain the necessary number of units connected in series in order to provide the desired voltage, given that the voltage is not affected by the dimensions of the generator. When the internal resistance matches the load resistance, the consumed voltage of the load, V_{load}, is half of the open-circuit voltage, as indicated by Equation 5.1 [80]. Therefore, V_{oc} must be 10 V.

$$\begin{aligned} V_{load} &= \frac{V_{oc} \cdot R_{load}}{R_{int} + R_{load}} \therefore \\ &= \frac{V_{oc}}{2} \end{aligned} \tag{5.1}$$

The legs of the thermoelectric have the same dimensions, meaning that the height, width and cross-sectional area of both thermoelectric legs are the same.

Using Equation 2.3, the two extreme temperatures are known and constant, presented in Table 4.8, as well as the function that expresses the Seebeck coefficient as a function of the temperature, defined in Equation 4.1, so the number of units is possible to calculate. By using these stated Equations, and equating the open-circuit voltage to 10 V, it is possible to conclude that the number of units must be 170, as shown in Equation 5.2.

$$
\begin{aligned}
V &= -n \cdot \int_{T_{low}}^{T_{high}} S(T) dT \therefore \\
-10 &= -n \cdot \int_{293.15\,\mathrm{K}}^{423.15\,\mathrm{K}} 2 \cdot \left[(22224 + 930.6 \cdot T - 0.9905 \cdot T^2) \cdot 10^{-9} \right] dT \therefore \\
n &= 169.38
\end{aligned} \tag{5.2}
$$

Afterwards, using Equation 4.5, Equation 2.27 and Equation 2.41, knowing that the optimal power occurs when the internal resistance is equal to the load resistance, it is possible to reach an equation to calculate γ_l.

Firstly, it is possible to simplify Equation 2.27 into Equation 5.3.

$$
\begin{aligned}
R_{int} &= \left(\frac{\rho_p \cdot L_p}{A_p} + \frac{\rho_n \cdot L_n}{A_n} \right) \therefore \\
&= 2 \cdot \frac{\rho_{Bi_2Te_3} \cdot h_l}{A_l}
\end{aligned} \tag{5.3}
$$

For the resistance ratio to be equal to the unit, R_{load} must be equal to R_{int}, as seen in Equation 5.4.

$$
\begin{aligned}
m &= 1 \therefore \\
R_{int} &= R_{load}
\end{aligned} \tag{5.4}
$$

Hence, utilising the previous Equations, the expression to obtain the ratio A_l/h_l is achievable and it is seen in Equation 5.5.

$$
\begin{aligned}
2 \cdot \frac{\rho_{Bi_2Te_3} \cdot h_l}{A_l} &= R_{load} \therefore \\
\frac{A_l}{h_l} &= \frac{2 \cdot \rho_{Bi_2Te_3}}{R_{load}}
\end{aligned} \tag{5.5}
$$

Admitting that A_{load} and L_{load} are defined in the construction of the model, it is necessary to know $\rho_{Bi_2Te_3}$ to then relate A_l/h_l to ρ_{load}. Using Equation 4.3, which describes the electrical conductivity of bismuth telluride, it is possible to obtain the resistivity, as it is seen in Equation 5.6.

$$\begin{aligned}
\rho_{Bi_2Te_3} &= \frac{n}{T_{high}-T_{low}} \cdot \int_{T_{low}}^{T_{high}} \frac{1}{\sigma(T)} dT \therefore \\
\rho_{Bi_2Te_3} &= \frac{170}{T_{high}-T_{low}} \cdot \int_{293.15\,\mathrm{K}}^{423.15\,\mathrm{K}} \left[(5112 + 163.4 \cdot T + 0.6279 \cdot T^2) \cdot 10^{-10}\right] dT \therefore \\
\rho_{Bi_2Te_3} &= 2.457\,041 \cdot 10^{-3}\,\Omega\,\mathrm{m}
\end{aligned} \tag{5.6}$$

Moreover, the maximum power produced by the generator must be, at least, equal to the necessary power of the load, of 0.1 W, as defined in Table 4.8. Recovering Equation 2.52, it is possible to obtain the required internal resistance 5.7.

$$\begin{aligned}
P_{max} &= \frac{1}{4} \cdot \frac{V_{oc}^2}{R_{int}} \therefore \\
0.1 &= \frac{1}{4} \cdot \frac{10^2}{R_{int}} \therefore \\
R_{int} &= 250\,\Omega
\end{aligned} \tag{5.7}$$

Therefore, the optimum ratio A_l/h_l can be calculated with Equation 5.8.

$$\begin{aligned}
\frac{A_l}{h_l} &= \frac{2 \cdot 2.457041 \cdot 10^{-3}}{250} \therefore \\
\frac{A_l}{h_l} &= \gamma_l = 1.965\,63 \cdot 10^{-5}\,\mathrm{m}
\end{aligned} \tag{5.8}$$

For a thickness of 90 µm, and preserving the geometrical proportion of c and p of the original design, it is possible to encounter an expression that relates the required width with the height of the legs. From the initial design, c and p corresponded to 28.125% and 56.25% of the width of the thermoelectric legs, respectively.

Allying to the geometric availability, specifically the available area defined in Table 4.8, the maximum possible dimensions for the generator can be found, with Equation 5.9. Since the width of the generator requires more attention than the corresponding height, due to limitations in the overall dimension of the TEG, it is considered the critical dimensional property to adjust in this problem.

$$
\begin{cases} \dfrac{A_l}{h_l} = 1.96563 \cdot 10^{-5}\,\mathrm{m} \\ w_{generator} \leq 0.1\,\mathrm{m} \end{cases} \therefore
$$

$$
\begin{cases} d_l \cdot \dfrac{w_l}{h_l} = 1.96563 \cdot 10^{-5} \\ n \cdot (2 \cdot w_l + 2 \cdot c + p) \leq 0.1 \end{cases} \therefore
$$

$$
\begin{cases} 90 \cdot 10^{-6} \cdot \dfrac{w_l}{h_l} = 1.96563 \cdot 10^{-5} \\ 170 \cdot (2 \cdot w_l + 2 \cdot 0.28125 \cdot w_l + 0.5625 \cdot w_l) \cdot 10^{-3} \leq 0.1 \end{cases} \therefore
$$

$$
\begin{cases} w_{l_{max}} = 0.1961\,\mathrm{mm} \\ h_{l_{max}} = 0.8979\,\mathrm{mm} \end{cases} \tag{5.9}
$$

Therefore, the leg width needs to be lower than 0.1961 mm and, consequently, h_l lower than 0.8979 mm. In Figure 5.1, the possible height and width values the legs can have are evident in the graph.

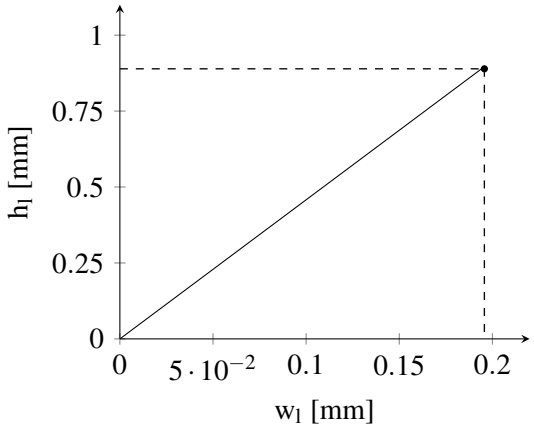

Figure 5.1: Theoretically admissible values for w_l and h_l of the generator legs.

For being a rounder number closer to the allowed limit, h_l was chosen to be equal to 0.89 mm, with a corresponding w_l of 0.194 mm. The final theoretical design of the generator is then found. Applying the theoretical principles presented in Chapter 2, it is possible to conclude that the final design of the generator has the required physical characteristics, as shown in Table 5.1.

Table 5.1: Properties of the theoretically optimised generator.

Property	Value
$A_{generator}$	100 mmx2.48 mm
V_{oc}	10.036 V
P	0.100 W
I	0.020 A
R_{int}	250.91 Ω
$z\overline{T}$	0.764
η	4.99%

5.2 Numerical parametric optimisation results

As seen in Subsection 4.3, the numerical optimisation through a parametric analysis is a valuable tool to verify the obtained theoretical results. With the different inputs, the numerical analysis was successfully performed and the output variables, such as maximum obtained voltage, the absorbed heat rate and the rejected one, were collected and the data was analysed in EXCEL.

The resulting scatter plot of the output power as a function of the number of units and the ratio A_l/h_l was interpolated into a surface and it is presented in Figure 5.2, as well as the line, represented in black, which intersects the plotted plane with the plane P=0.1 W, represented in orange.

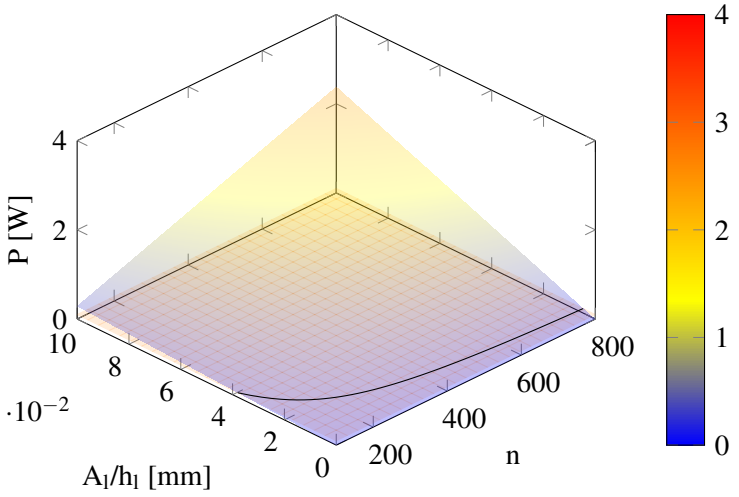

Figure 5.2: Output power for variable values of n and γ_l.

Analysing the results, it is possible to confirm that the increase of the number of units leads to the increase of the output power. Moreover, the increase of the ratio A_l/h_l, either through the increase of the width or the decrease of the height of the legs, also translates into the increase of power.

Additionally, it is also possible to conclude from Figure 5.2 that, when the output power is equal to the desired value, A_l/h_l is inversely proportional to the number of units. Furthermore, for

the required number of units, 170, the corresponding ratio is equal to $2.234\,721\,2 \cdot 10^{-2}$ mm. This result is similar to the one obtained in the theoretical optimisation, in Equation 5.8.

By considering only the results for the 170-unit generator, the output power was plotted as a function of the width and the height of the thermoelectric legs in Figure 5.3. Additionally, the necessary power, equal to 0.1 W, is shown for reference and the intersection between the two functions is exhibited in black. For better visibility, Figure 5.4 is the same graph with lower values on both the width and height axes.

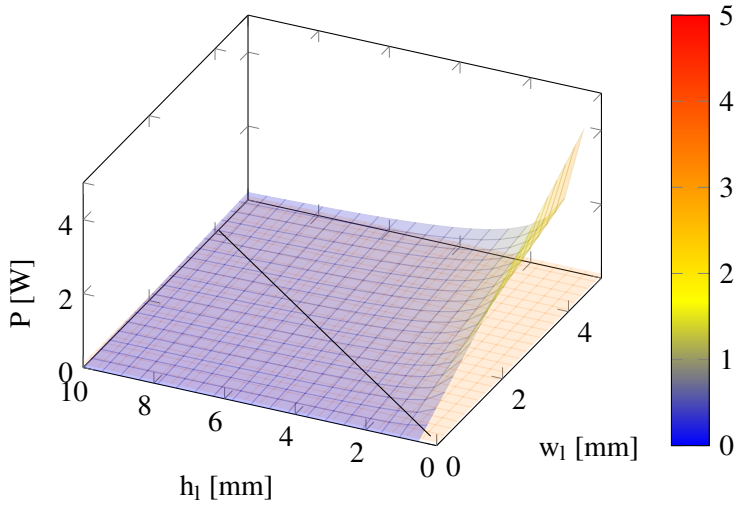

Figure 5.3: Output power for variable values of w_l and h_l.

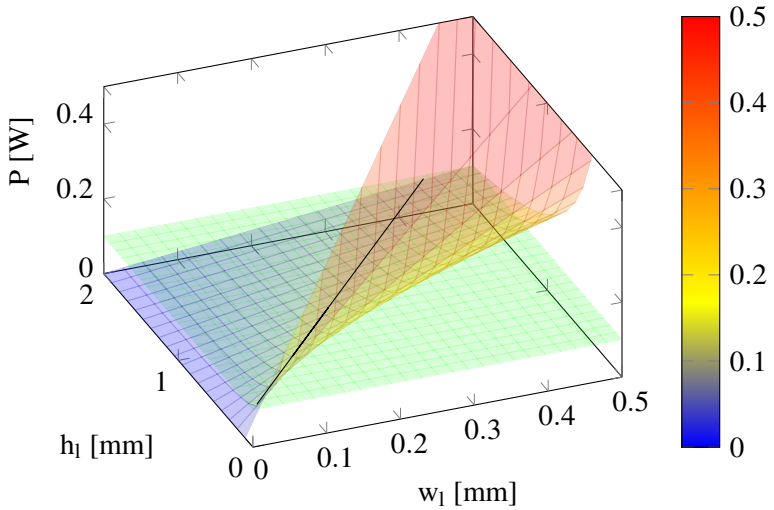

Figure 5.4: Output power for variable values of w_l and h_l detailed.

The power evolved linearly with the width, but in an inversely proportional way to the height of the thermoelectric legs. Intersecting the obtained interpolated plane and the one where the power is equal to 0.1 W, a line was obtained, meaning that, as seen in the theoretical optimisation, there

is a linear relationship between the dimensions of the generator in order to work at a maximum power condition.

The intersection line is plotted in a two-dimensional graph in Figure 5.5, and the signaled point represents the maximum admissible width and height of the semiconductor elements of the generator.

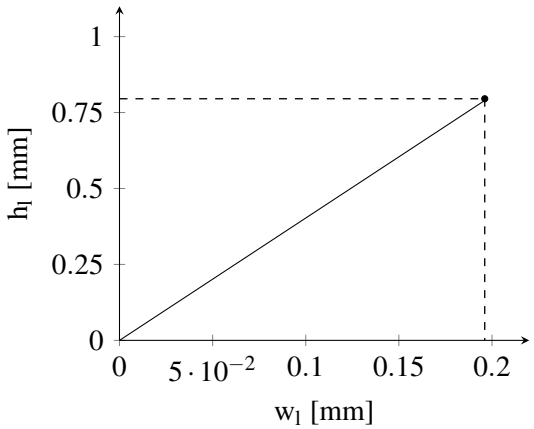

Figure 5.5: Numerically admissible values for w_l and h_l of the generator legs.

In this case, by choosing the theoretical width of 0.194 mm for the generator, the height of the legs should be equal to 0.765 mm. Therefore, the final numerically optimised design was found and it is similar to the theoretical one. In Table 5.2, the output parameters of the generator are displayed.

Table 5.2: Properties of the numerically optimised generator.

Property	Value
$A_{generator}$	100 mmx2.37 mm
V_{oc}	9.973 V
P	0.10 W
I	0.020 A
R_{int}	250.91 Ω
$z\overline{T}$	0.764
η	4.99%

5.3 Final design

In this Subsection, the final design of the generator is analysed. In fact, since the numerical and theoretical final generators have similar dimensions and output properties, it is possible to conclude that the two models efficiently performed the parametric optimisation procedure. In Figure 5.6, the design of one unit of the optimised 170-unit generator is presented and its dimensions are shown in Table 5.3.

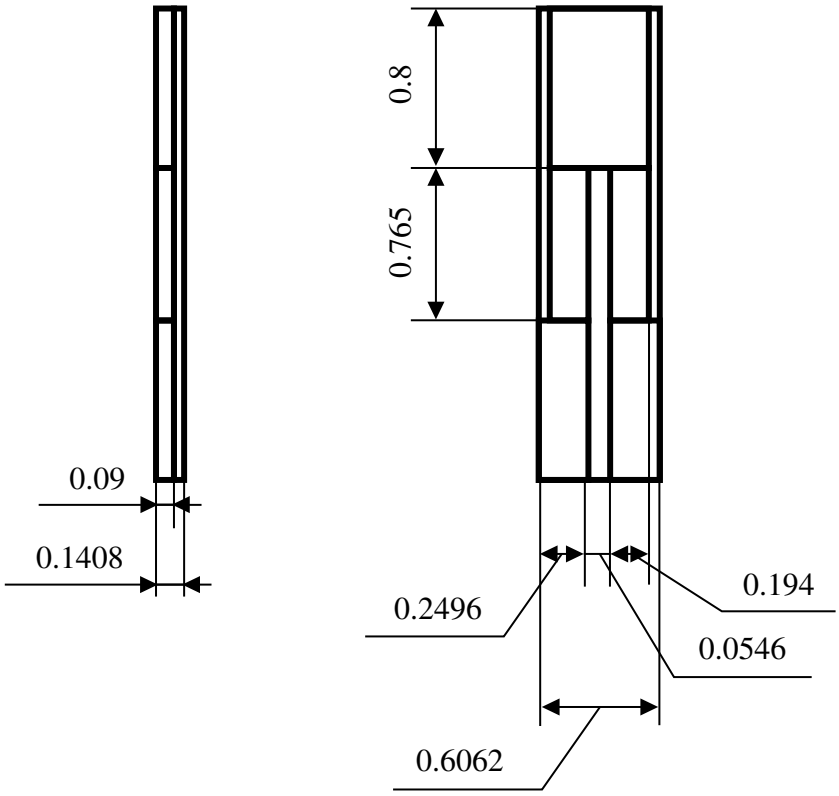

Figure 5.6: Final design of each unit of the optimised 170-unit TEG (dimensions in millimetres).

Table 5.3: Parameters of the final design of the model.

Parameter	Value
w_l	0.194 [mm]
h_l	0.765 [mm]
t	0.09 [mm]
p	0.09828 [mm]
c	0.04914 [mm]
h_c	0.8 [mm]
t_s	0.0508 [mm]
n	170

Additionally, Figure 5.7 shows a three-dimensional model of the generator unit and Figure 5.8 depicts the model of the TEG in its entirety.

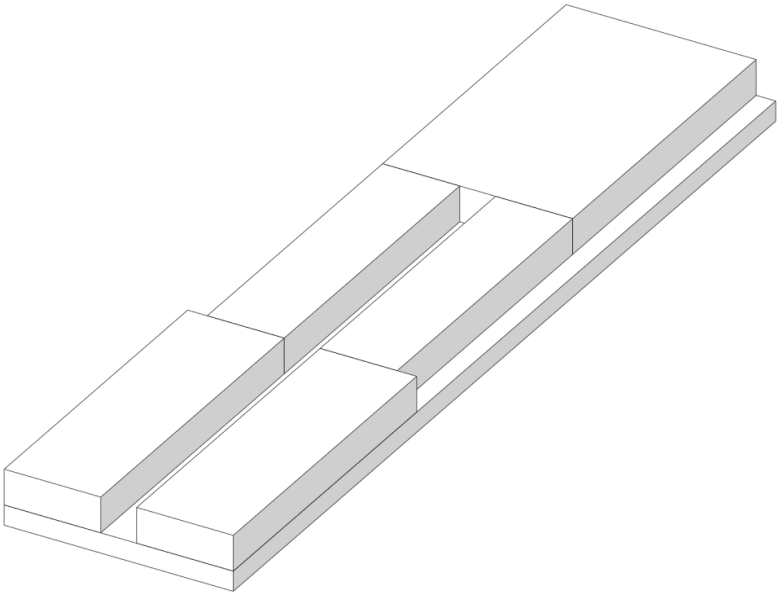

Figure 5.7: Three-dimensional model of the final design of one unit of the TEG.

The semiconductor components of the generator are connected thermally in parallel and electrically in series. For the applied thermal conditions, it is possible to obtain the temperature and voltage profiles of the generator, which are shown in Figure 5.9 and Figure 5.10, respectively.

Looking at the temperature profile shown in Figure 5.9, it is possible to verify that the TEG is working in the expected way, since the temperature of the generator varied vertically and evolved in parallel to the height of the semiconductor legs, from the heat source to the heat sink. In addition, in the exhibited voltage profile, presented in Figure 5.10, the voltage increased horizontally. As explained in Section 4.1.6, the leftmost unit of the generator possesses the electrical boundary condition of having a surface with 0 V and, therefore, the voltage increases through the course of the attached units to its right.

Figure 5.8: Three-dimensional model of the final design of one unit of the TEG.

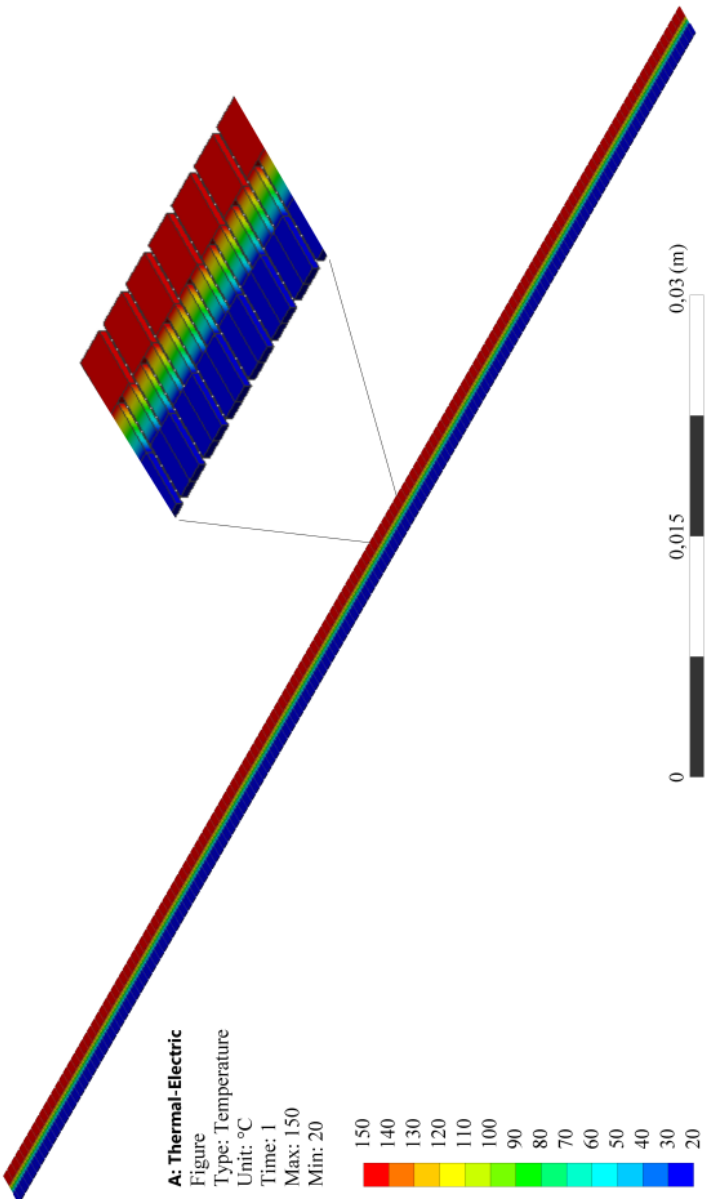

Figure 5.9: Three-dimensional temperature profile of TEG.

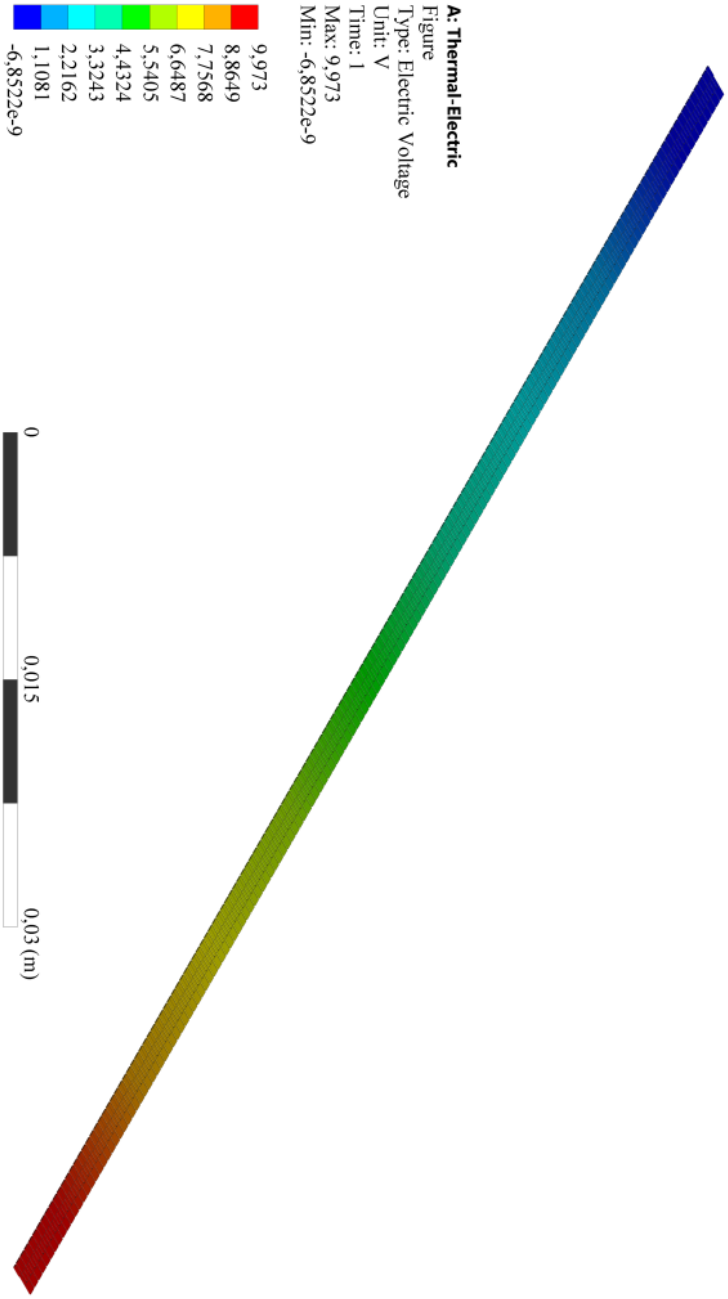

Figure 5.10: Three-dimensional voltage profile of TEG.

However, looking at the dimensions of the final design, it is possible to question the feasibility of the generator. In fact, since the value of the height of the generator is very small, the preservation of the desired temperature gradient, of 130 °C, seems unrealistic and not possible, since the TEG is not perfectly isolated in reality, contrary to the simulation process. Additionally, the small dimensions of the generator may not be printable through the available dispenser printer and with the necessary material and dimensional quality.

In fact, the available space is very small for the necessary requirements, as well as the existing temperature gradient.

For instance, for the same available area, if the heat source temperature was raised from 150 °C to 250 °C, the obtained voltage in each unit would increase, decreasing the number of necessary units. Performing this calculation, in order to achieve the required 10 V in the terminals of the generator, the number of necessary units would only be 94. Hence, the maximum width and height of the semiconductor legs would be 0.34 mm and 2.288 mm, respectively. Despite still leading to a generator whose practical performance is questionable, the dimensions of the generator would witness a drastic increase relatively to the established dimensions of the final design.

Moreover, preserving the new hypothetical heat source temperature of 250 °C, but increasing the available area to 20 cmx10 cm, the maximum height and width admissible would be raised to 4.603 mm and 0.685 mm, respectively.

Therefore, the manufacturing and testing of the design would be of major importance to verify the feasibility of the design. In the case of the generator being unprintable, due to the small dimensions which require a higher printer resolution, the established area would have to increase, to allow bigger components.

Chapter 6

Conclusions and Future Work

6.1 Conclusions

The main objective of this thesis, which was the development of a parametrically optimised planar thermoelectric generator for a set of physical constraints, was successfully accomplished.

Firstly, the research of the theoretical phenomena that occur in a thermoelectric generator took place, and it was an essential step of this project, since the equations which mathematically represent these phenomena where crucial for the creation of the theoretical parametric optimisation tool used to corroborate the obtained numerical values.

Afterwards, the examination of the state-of-the-art thermoelectric generators was vital to develop the configuration of the model, as well as the chosen materials for the substrate and the semiconductors.

The thermoelectric phenomenon was simulated using ANSYS 2019, a simulation software which utilises the finite element method to solve complex analytical equations. Using this software, it was possible to parametrically optimise the design of a planar thermoelectric generator, through the optimisation of the parameters that directly influence the performance, namely the dimensions of the semiconductor components and the number of units connected in series.

The numerical and theoretical results showed that the alteration of the heat source temperature, the number of units of the generator and the dimensions of the semiconductor materials is the most effective way of changing the output power produced by the generator, the former one not being applicable in this project. Furthermore, the increase of the number of units in a generator positively impacted the output power, as well as the increase of the cross-sectional area of the legs, whereas the increase of their height created a higher thermal resistance, decreasing the performance of the generator.

Moreover, an optimal design of the generator was achieved, having the 170-unit generator's legs a width of 0.194 mm, a height of 0.765 mm and a thickness of 0.09 mm. The device, which occupies an area of 100 mm x 2.37 mm, is able to produce 0.10 W of power, an output current of 0.02 A, an open-circuit voltage equal to 9.973 V, and it possesses an internal resistance equal to 250.91 Ω. In addition, the bismuth telluride legs, connected with silver contacts and printed

onto a polyimide substrate, has a figure of merit equal to 0.764. Given the similarities between the theoretical and practical final designs, it is possible to conclude that both models efficiently performed the optimisation procedure, and could be essential tools to predict and evaluate the performance of already existing planar thermoelectric devices in specified operating conditions.

However, it is questionable if the device can be successfully printed in the available dispenser printer with the necessary quality, as well as if the device would be able to efficiently perform and preserve the imposed temperature gradient across the small generator height. Furthermore, easing the imposed thermal and geometrical constraints, namely the increase of the heat source temperature and available area, the generator could potentially assume more feasible dimensions.

6.2 Further Work

Even though the final design was achieved and, therefore, the optimisation problem was successfully solved, there is still room for further development of the generator.

Firstly, the theoretical model used in this project did not consider the heat transfer mechanisms of convection and radiation. In addition, it did not take into account any thermal contact resistances, considered negligible, and, therefore, it would be interesting to complement the created theoretical tool with more complex equations which contemplate these phenomena.

Additionally, the increase of the output parameters of the thermoelectric generator could be achieved through segmentation of the legs with different materials. In fact, the legs of TEGs could be made from more than one semiconductor materials, in an attempt to increase their performance with limited resources. It would be interesting to analyse the possibility of implementing other semiconductor materials indicated for lower temperature applications, such as other chalcogenides.

Finally, the future work of greater importance would be the practical experimentation of the generator, which was not carried because of the safety measures imposed by CeNTI due to the COVID-19 situation.

Through an experimental setup, the final design of the generator could be tested, and the results would indicate how well the generator would perform realistically. Afterwards, the practical results could be analysed and compared to the obtained ones in the theoretical and numerical analysis.

Additionally, the manufacturing of the thermoelectric generator through dispenser printing would first require a rheological study of the functional inks, to measure their compatibility with the existing printer. Afterwards, it would have been required to program the equipment of additive manufacturing in order to fabricate the different components sequentially and later perform the necessary heat treatments.

Finally, analysing the dimensions and output parameters of the produced generator, which implies that the dispensing printer possesses the required resolution to efficiently print the different components, the numerical and theoretical models could be altered to encompass the necessary

changes in order for a new generator design to be found and later printed. The new generator would be able to more efficiently recover waste heat in practical operating conditions.

Appendix A

Simulated models

A.1 Number of units

The utilised models, ranging from one to nine units, are shown respectively in Figures A.1 through A.9.

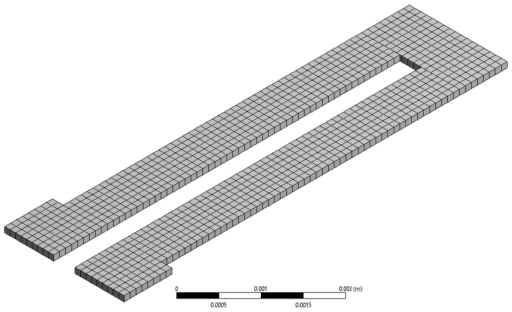

Figure A.1: Model of generator with 1 unit and the applied mesh.

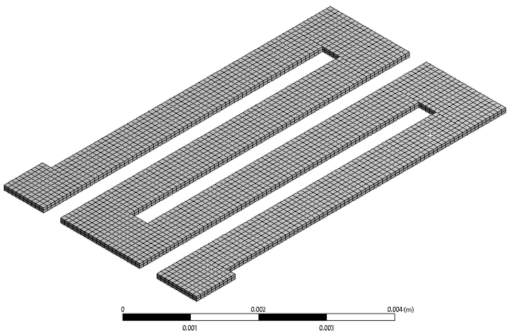

Figure A.2: Model of generator with 2 units and the applied mesh.

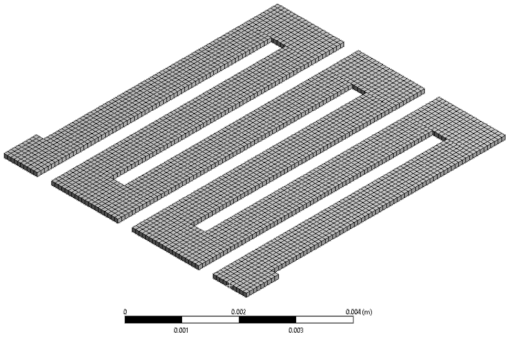

Figure A.3: Model of generator with 3 units and the applied mesh.

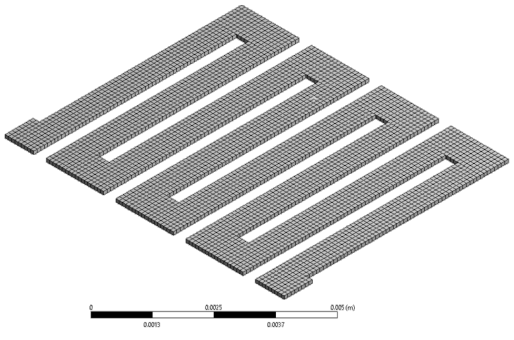

Figure A.4: Model of generator with 4 units and the applied mesh.

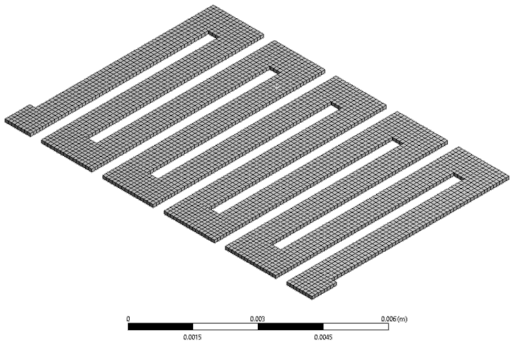

Figure A.5: Model of generator with 5 units and the applied mesh.

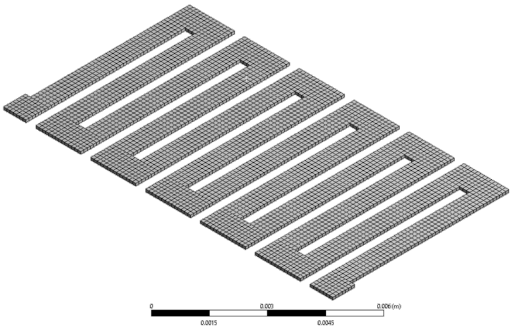

Figure A.6: Model of generator with 6 units and the applied mesh.

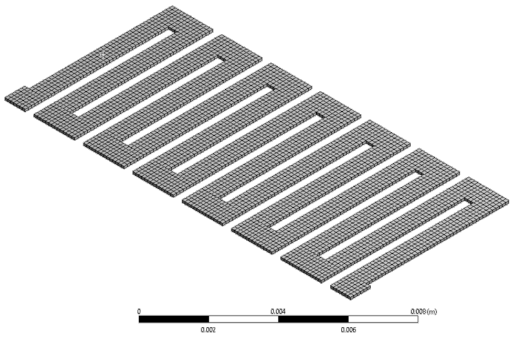

Figure A.7: Model of generator with 7 units and the applied mesh.

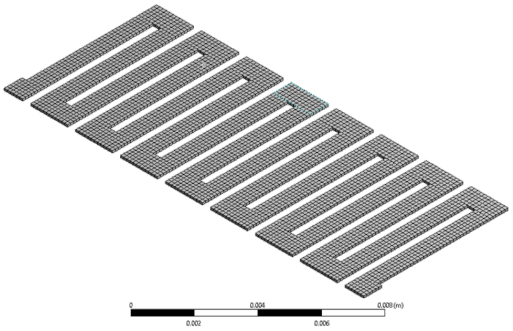

Figure A.8: Model of generator with 8 units and the applied mesh.

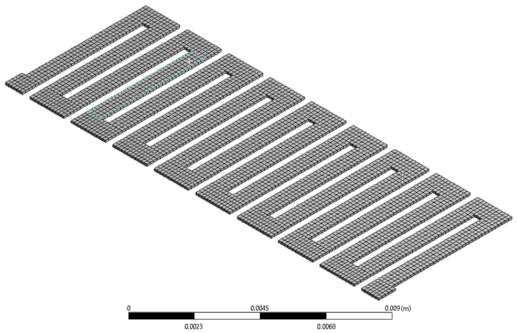

Figure A.9: Model of generator with 9 units and the applied mesh.

A.2 Isolated model

The models, which were utilised to study the impact of the coating on the performance of a unit, are seen in Figure A.10 through Figure A.13, where the thickness was equal to, respectively, 0 µm, 30 µm, 60 µm and 90 µm.

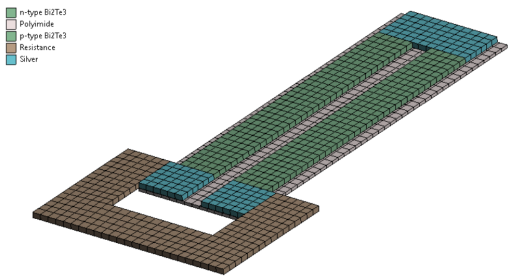

Figure A.10: Model of generator with 1 unit without coating.

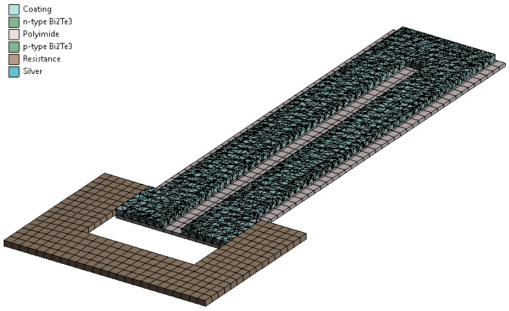

Figure A.11: Model of generator with 1 unit with a 30 µm coating.

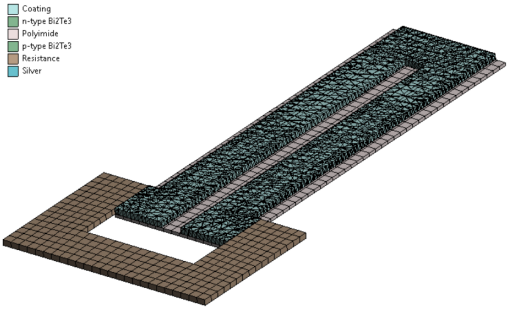

Figure A.12: Model of generator with 1 unit with a 60 µm coating.

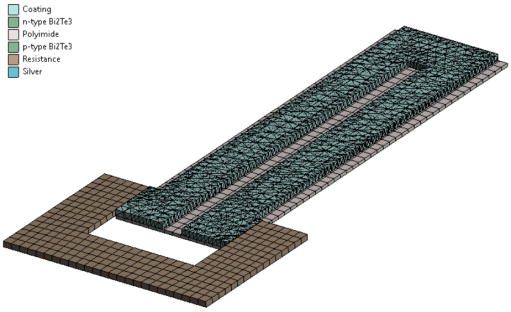

Figure A.13: Model of generator with 1 unit and a with a 90 µm coating.

A.3 Substrate material and thickness

The models which were utilised to study the impact of the substrate material and thickness, are seen in Figure A.14 through Figure A.15, where the thickness was altered between 50.8 µm, 101.6 µm and 152.4 µm, respectively.

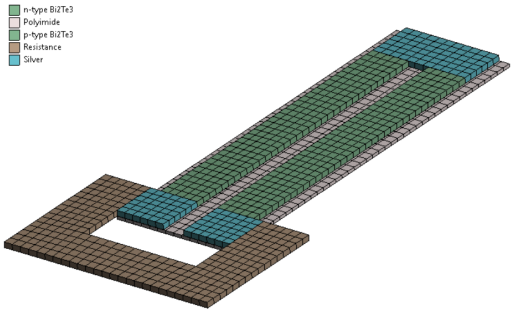

Figure A.14: Model of generator with 1 unit with polyimide 50.8 µm.

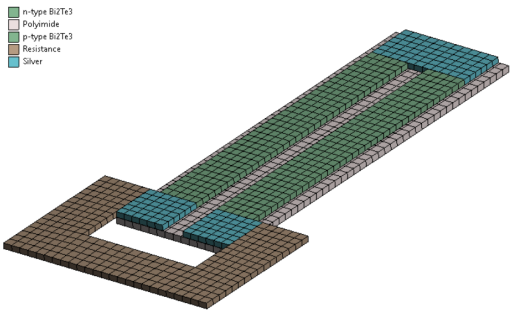

Figure A.15: Model of generator with 1 unit with polyimide 101.6 µm.

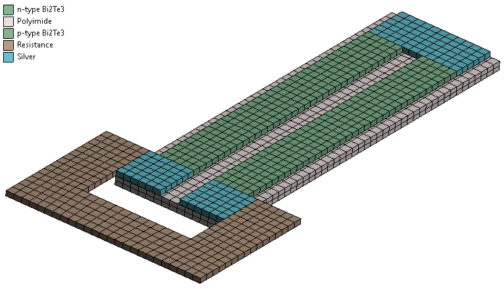

Figure A.16: Model of generator with 1 unit with polyimide 152.4 µm.

A.4 Unit depth

In this Section, half of the simulated models are shown, from Figure A.17 to Figure A.21, where the thickness was altered between 100 µm and 500 µm.

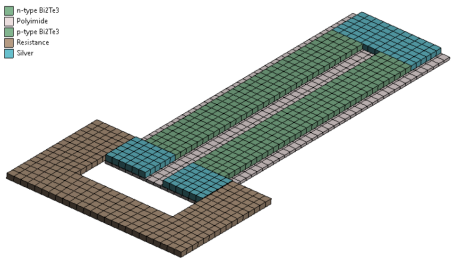

Figure A.17: Model of generator with a depth of 100 µm.

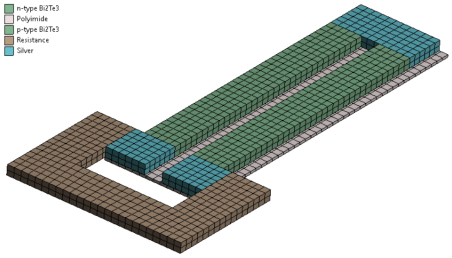

Figure A.18: Model of generator with a depth of 200 µm.

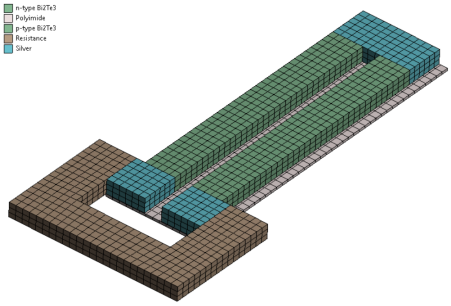

Figure A.19: Model of generator with a depth of 300 µm.

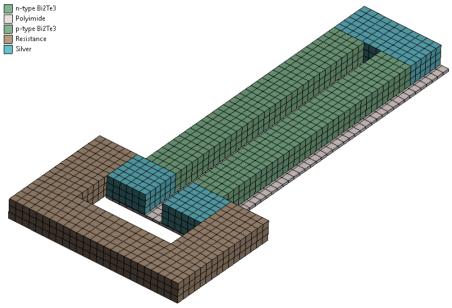

Figure A.20: Model of generator with a depth of 400 µm.

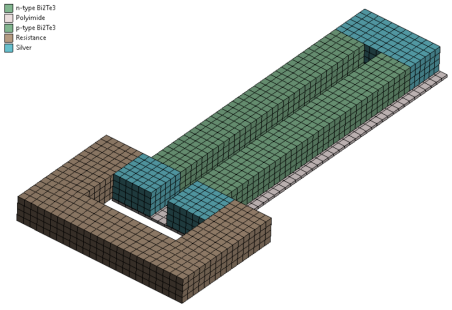

Figure A.21: Model of generator with a depth of 500 µm.

A.5 Leg dimensions

Upon the analysis the impact of the leg dimensions on the performance of the generator, several models were created. In this Section, firstly, the models where the height of the semiconductor materials was changed are shown from Figure A.22 to Figure A.31. Afterwards, the same logic applied to the width, and the obtained models are shown from Figure A.32 to Figure A.39.

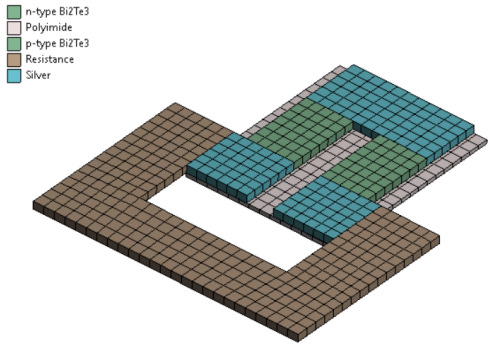

Figure A.22: Model of generator with a height of 1 mm.

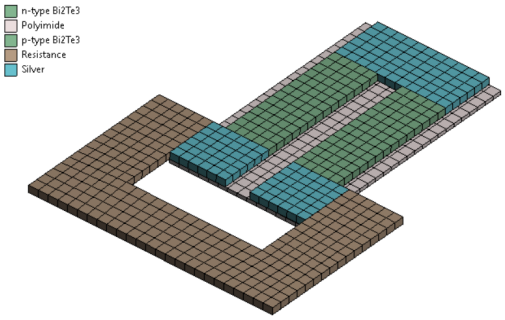

Figure A.23: Model of generator with a height of 2 mm.

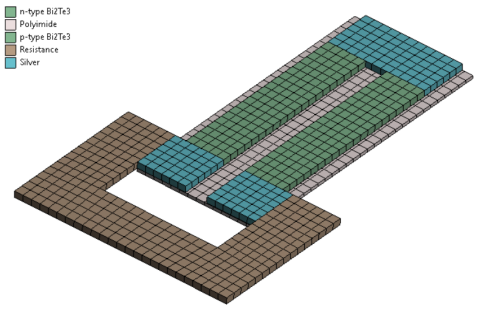

Figure A.24: Model of generator with a height of 3 mm.

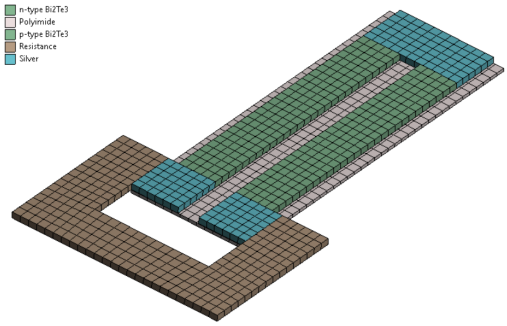

Figure A.25: Model of generator with a height of 4 mm.

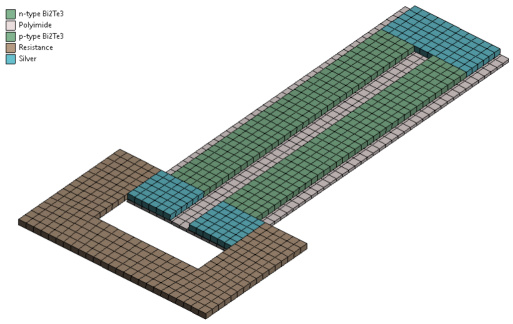

Figure A.26: Model of generator with a height of 5 mm.

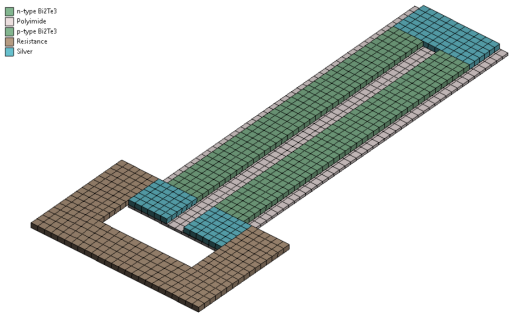

Figure A.27: Model of generator with a height of 6 mm.

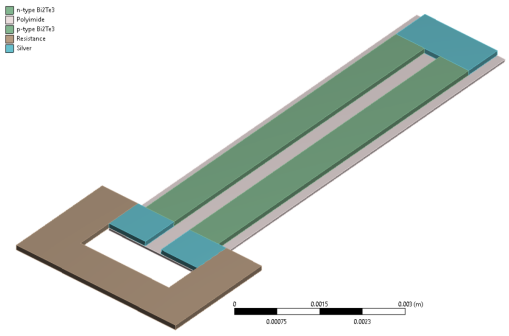

Figure A.28: Model of generator with a height of 7 mm.

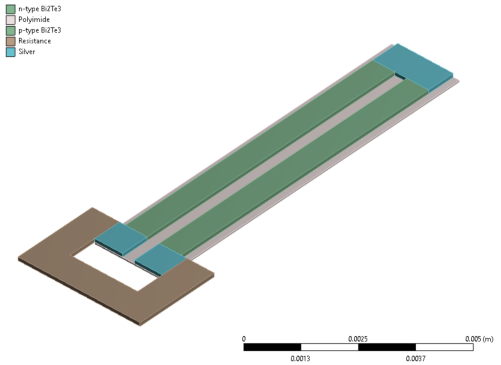

Figure A.29: Model of generator with a height of 8 mm.

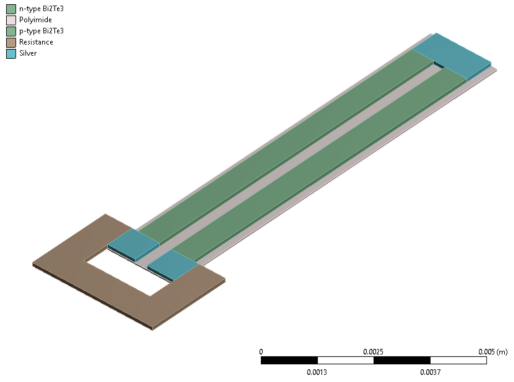

Figure A.30: Model of generator with a height of 9 mm.

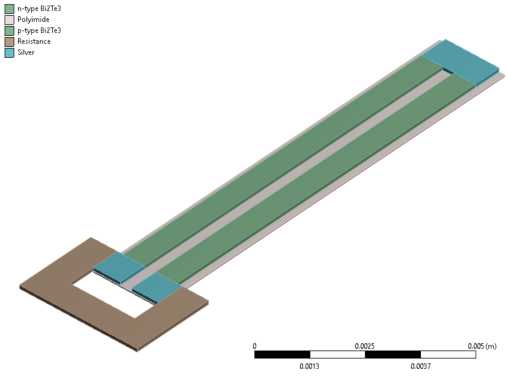

Figure A.31: Model of generator with a height of 10 mm.

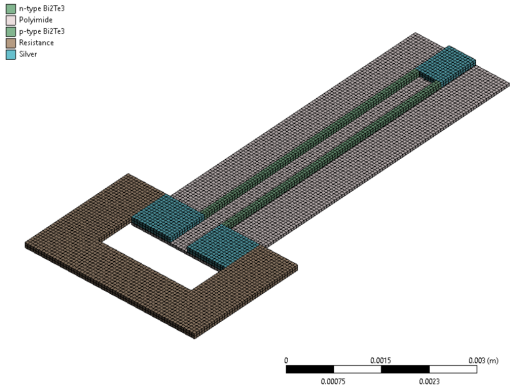

Figure A.32: Model of generator with a width of 0.1 mm.

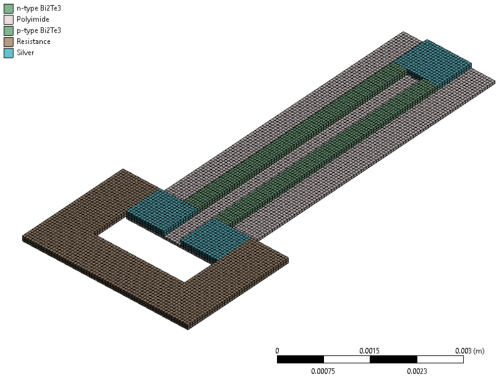

Figure A.33: Model of generator with a width of 0.2 mm.

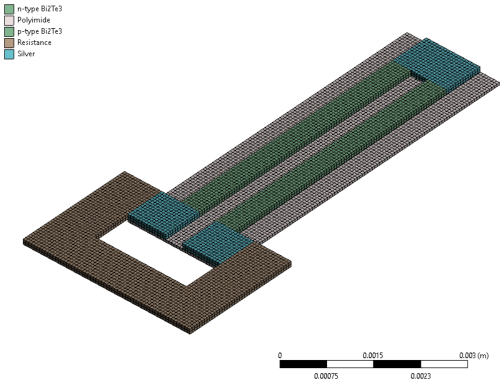

Figure A.34: Model of generator with a width of 0.3 mm.

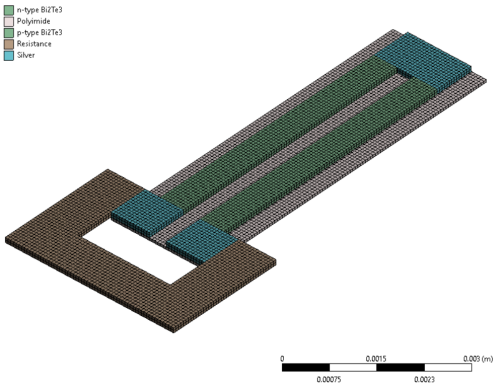

Figure A.35: Model of generator with a width of 0.4 mm.

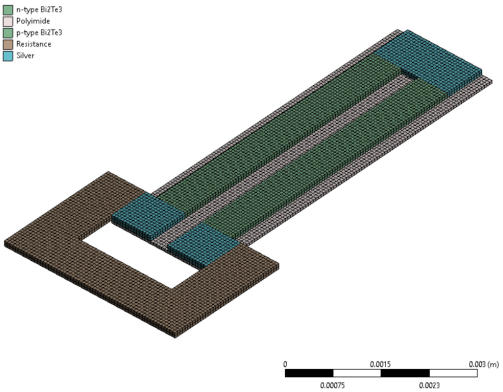

Figure A.36: Model of generator with a width of 0.5 mm.

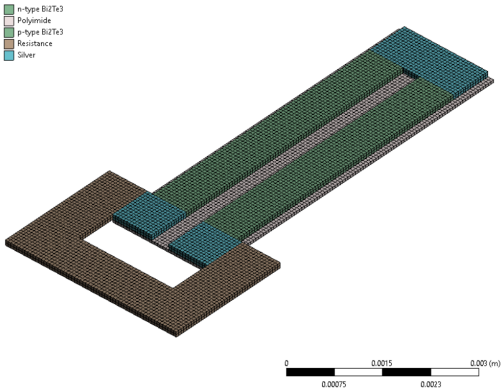

Figure A.37: Model of generator with a width of 0.6 mm.

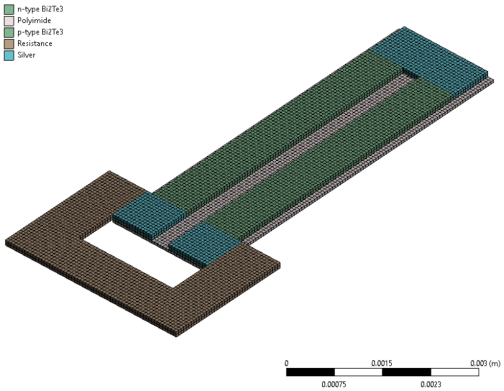

Figure A.38: Model of generator with a width of 0.7 mm.

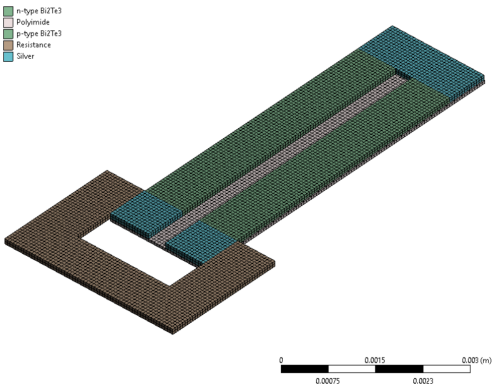

Figure A.39: Model of generator with a width of 0.8 mm.

Appendix B

EXCEL sheet used in theoretical optimisation

The theoretical parametric optimisation of the thermoelectric was done through the definition of the different parameters with theoretical equations. As seen in Figure B.1, Figure B.2 and Figure B.3, there is an indication of the used Equations of Section 2, for clarification.

In Figure B.1, the initial design was introduced in the spreadsheet. Afterwards, the Solver tool was utilised in order to optimise the dimensions, shown in Figure B.2. Finally, in Figure B.3, n and γ_l were calculated and the cell w_l and h_l were altered to define the maximum dimensions allowed for the available space.

Thermal properties					**Internal properties**			
T_{low}	293.15	K			R_{int}	2.5184	Ω	(2.27)
T_{high}	423.15	K			V_{oc}	0.05904	V	(2.3)
ΔT	130	K			K_{int}	3.83767E-05	W K^{-1}	(2.29)
$\bar{T}$	358.15	K			z	0.00213	K^{-1}	(2.21)
Material properties					$z\bar{T}$	0.764	-	(2.21)
$n\int S(T)/(\Delta T)$	4.541E-04	V K^{-1}			η_{Carnot}	30.72%	-	(2.40)
$n\int \rho(T)/(\Delta T)$	2.901E-05	Ω m			**Desired electrical properties**			
$n\int \sigma(T)/(\Delta T)$	1.415E+05	S m^{-1}			$V_{desired}$	5	V	
$n\int k(T)/(\Delta T)$	3.331E+00	W m^{-1} K^{-1}			$P_{desired}$	0.1	W	
Generator dimensions					R	250	Ω	(2.17)
n	**1**	-			I	0.02	A	(2.4)
$W_{max,\ generator}$	0.1	m			**Electrical properties**			
$H_{max,\ generator}$	0.1	m			R_{load}	250	Ω	(2.17)
$n_{max,\ horizontal}$	50	-	(5.9)		m	**0.01**	-	(2.41)
Component dimensions					$V_{consumed}$	0.05845	V	(5.1)
w_l	6.40E-04	m			I	0.0002	A	(2.39)
h_l	5.00E-03	m			P	**0.000014**	W	(2.4)
d_l	9.00E-05	m			$\dot{Q}_{low}$	0.00502	W	(2.35)
h_c	8.00E-04	m			$\dot{Q}_{high}$	0.00503	W	(2.33)
c	1.80E-04	m			$\Delta\dot{Q}$	0.00	W	(2.36)
p	3.60E-04	m			η	4.99%	-	(2.45)
d_s	5.08E-05	m			**Optimum electrical properties**			
A_l	5.76E-08	m^2			P_{max}	**0.000346**	W	(2.53)
γ_l (A_l/h_l)	**1.15E-05**	m	(2.46)		η_{max}	4.99%	-	(2.50)

Figure B.1: Definition of the initial design in spreadsheet.

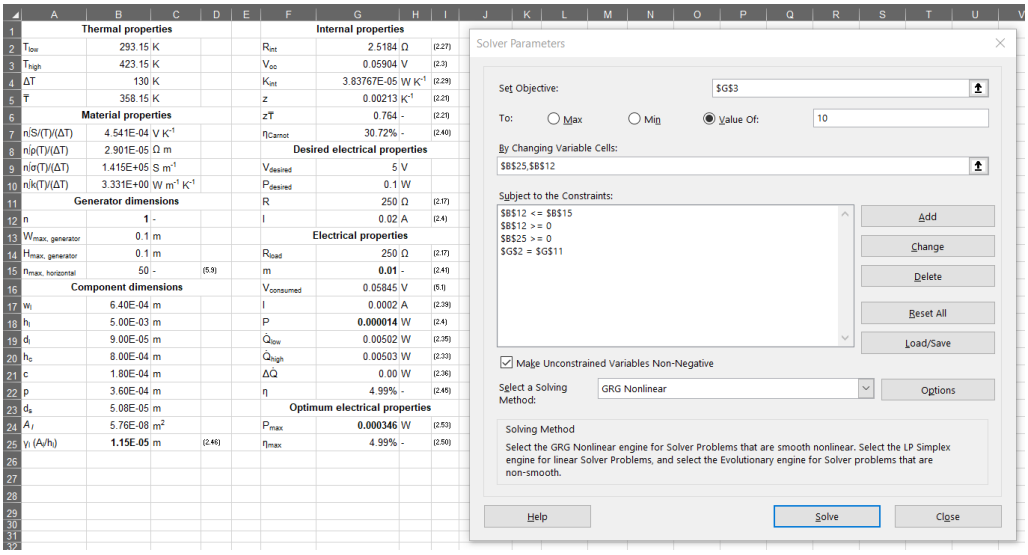

Figure B.2: Solver tool utilised in the optimisation of the generator.

	A	B	C	D	E	F	G	H	I
1	**Thermal properties**					**Internal properties**			
2	T_{low}	293.15	K			R_{int}	250.9130	Ω	(2.27)
3	T_{high}	423.15	K			V_{oc}	10.03652	V	(2.3)
4	ΔT	130	K			K_{int}	0.011131833	W K^{-1}	(2.29)
5	$\overline{T}$	358.15	K			z	0.00213	K^{-1}	(2.21)
6	**Material properties**					$z\overline{T}$	0.764	-	(2.21)
7	n∫S/(T)/(ΔT)	7.720E-02	V K^{-1}			η_{Carnot}	30.72%	-	(2.40)
8	n∫ρ(T)/(ΔT)	4.932E-03	Ω m			**Desired electrical properties**			
9	n∫σ(T)/(ΔT)	2.405E+07	S m^{-1}			$V_{desired}$	5	V	
10	n∫k(T)/(ΔT)	5.663E+02	W m^{-1} K^{-1}			$P_{desired}$	0.1	W	
11	**Generator dimensions**					R	250	Ω	(2.17)
12	n	**170**	-			I	0.02	A	(2.4)
13	$W_{max,\ generator}$	0.1	m			**Electrical properties**			
14	$H_{max,\ generator}$	0.1	m			R_{load}	250	Ω	(2.17)
15	$n_{max,\ horizontal}$	163	-	(5.9)		m	**1.00**	-	(2.41)
16	**Component dimensions**					$V_{consumed}$	5.00911	V	(5.1)
17	w_l	1.961E-04	m			I	0.0200	A	(2.39)
18	h_l	8.979E-04	m			P	**0.10**	W	(2.4)
19	d_l	9.00E-05	m			$\dot{Q}_{low}$	1.95098	W	(2.35)
20	h_c	8.00E-04	m			$\dot{Q}_{high}$	2.05134	W	(2.33)
21	c	5.52E-05	m			$\Delta\dot{Q}$	0.10	W	(2.36)
22	p	1.10E-04	m			η	4.99%	-	(2.45)
23	d_s	5.08E-05	m			**Optimum electrical properties**			
24	A_l	1.76E-08	m^2			P_{max}	**0.10**	W	(2.53)
25	γ_l (A_l/h_l)	**1.97E-05**	m	(2.46)		η_{max}	4.99%	-	(2.50)

Figure B.3: Theoretical final design of the generator.

Appendix C

Full Paper

In this Appendix, the following paper was accepted and published in the proceedings of *IRF2020 -INTEGRITY-RELIABILITY-FAILURE* conference.

The presentation of this work at the conference will be held, due to the COVID-19 situation, by video conference from the 6^{th} to the 10^{th} of September 2020.

Proceedings IRF2020: 7th International Conference Integrity-Reliability-Failure.
J.F. Silva Gomes and S.A. Meguid (editors), INEGI-FEUP (2020), pp.653-662.
https://paginas.fe.up.pt/~irf/Proceedings_IRF2020/

PAPER REF: 17884

SIMULATION, OPTIMIZATION AND DEVELOPMENT OF A THERMOELECTRIC PLANAR DEVICE

M.C. Fernandes[1], C. Furtado[3], D. Campanhã[3], S.I.S. Pinto[1,2(*)]

[1]Engineering Faculty, University of Porto, Porto, Portugal
[2]Institute of Science and Innovation in Mechanical and Industrial Engineering (LAETA-INEGI), Porto, Portugal
[3]Centre for Nanotechnology and Smart Materials (CeNTI), Vila Nova de Famalicão, Portugal
[(*)]*Email:* spinto@fe.up.pt

ABSTRACT

Thermoelectric devices and materials have been under research for their promising capabilities to convert thermal energy into electricity. In order to develop flexible thermoelectric devices, an extensive analysis of the state-of-the-art semiconductor materials was made. The current project aims to design and optimize a numerical model of a planar thermoelectric generator (TEG). From the results of the numerical simulations, the energy harvesting device will then be developed by a dispensing printing process.

Keywords: thermoelectric, flexible devices, energy harvesting, numerical simulation, dispensing

INTRODUCTION

A thermodynamic power cycle produces heat which, in most cases, is not recovered to power secondary low-energy cycles. However, with the increase of the energy demands and the arising challenges of producing electricity in a more efficient way lead to a search of recovering such wasted heat. Additionally, the development of technology lead to more powerful and portable devices that are not constantly connected to a power grid, from the common mobile phone and laptop to, for instance, pressure sensors connected to a natural gas pipeline with an extension of several kilometres.

A phenomenon like thermoelectricity is a potential way of bridging the gap since it exhibits attractive advantages. Firstly, a thermoelectric generator (TEG) does not emit any pollutants to the atmosphere. Secondly, since there are no moving components, the overall system requires low levels of maintenance, reducing the operation costs. Thirdly, the devices are self-sustainable and are easily adaptable and scalable. Furthermore, the process can be reversed to induce a temperature gradient between two spaces, by consuming electricity to create a heating or cooling effect for Peltier heaters and coolers, respectively.

However, the low efficiency conversion of waste heat into electricity, due to the low efficiency of thermoelectric materials (He and Tritt 2017), should not deter researchers from continuing to improve this technology, which still increases the overall efficiency of a power generation system. TEG has a promising role in the future of electricity generation.

Suarez *et al.* (2016) produced a self-powered wearable electronic device using a thermoelectric generator which recovered body heat, reaching a maximum power of 120 μW. Baranowski *et al.* (2012) developed a solar thermoelectric generator which used a concentrated solar collector as the heat source, achieving a 15.9% conversion efficiency.

The present document intends to design and optimize, numerically, a flexible thermoelectric generator in order to fabricate the best design by dispensing. The obtained geometry, conditioned by physical restrictions of the printer and the geometrical restrictions of the device, will be further validated through experimental settings of the manufactured model. One interesting application is in a micro temperature sensor for electronic purposes.

THERMOELECTRIC GENERATOR

The thermoelectric generators are devices that convert waste heat at a high temperature, above the average ambient temperature, and convert it to electricity due to the resulting temperature gradient. The efficiency of the conversion, η, is the ratio between the electrical output P and the recovered heat Q_{high} (He, *et al.* 2015):

$$\eta = \frac{P}{Q_{high}} \tag{1}$$

The efficiency of a thermoelectric generator is defined as the ratio between the useful output and the necessary input to achieve it. The heat flow in a thermoelectric generator results from a combination of four types of heat flows: Joule heat, Peltier heat, conduction heat and, finally, the heat Q_{high} absorbed from the heat source at a fixed temperature T_{high} as well as Q_{low}, the emitted heat to the heat sink, at a constant temperature T_{low}.

The Joule heat derives from the Joule's First Law (Eq. 2). When a resistor is subjected to a current flow, it produces an amount of heat proportional to the resistance and to the square of the current. Next, the Peltier heat is released and absorbed near the hot source and heat sink, respectively, as a result of the thermoelectric effect, since the source and sink are set at a constant temperature. The Peltier effect explains why a material exposed to a temperature gradient and a current flow will absorb or reject heat if the heat and current flows are in the same or in opposite directions. It can be calculated with the Seebeck coefficient, S, the current, I, and the temperature T (Eq. 3). Moreover, since the dominant heat transfer mechanism is conduction, there is also the conduction heat (4), which depends on the internal thermal resistance R_{int}, calculated with the knowledge of the cross-sectional area A and length L in the direction of the heat flow, as well as the thermal conductivity k (Eq. 5) (He*, et al.* 2015).

$$Q_{Joule} = I^2 \cdot R \qquad [W] \tag{2}$$

$$Q_{Peltier} = S \cdot I \cdot T \qquad [W] \tag{3}$$

$$Q_{cond} = \frac{\Delta T}{R_{int}} \qquad [W] \tag{4}$$

$$R_{int} = \frac{L}{A \cdot k} \qquad \left[\frac{K}{W}\right] \tag{5}$$

Performing an energy balance near the heat source and another closer to the heat sink, the heat flows Q_{high} (Eq. 6) and Q_{low} (Eq. 7) can be calculated, where K is the thermal conductance, the inverse of the internal thermal resistance.

$$Q_{high} = -\frac{1}{2} \cdot I^2 \cdot R + \left(T_{high} - T_{low}\right) \cdot K + S \cdot I \cdot T_{high} \qquad [W] \tag{6}$$

$$Q_{low} = \frac{1}{2} \cdot I^2 \cdot R + \left(T_{high} - T_{low}\right) \cdot K + S \cdot I \cdot T_{low} \qquad [W] \tag{7}$$

In addition, the output power is given by the difference between the absorbed and the rejected heat, as well as the product between the current and the load resistance R_{load}, corresponding to the resistance of the component powered by the generator. Therefore, it is possible to express

the efficiency as a function of the geometric and material properties of the device (Eq. 8), introducing the concept m, the resistance ratio between the internal resistance of the semiconductor and the load resistance.

$$\eta = \frac{T_{high}-T_{low}}{T_{high}} \cdot \frac{m}{-\frac{1}{2}\cdot\frac{T_{high}-T_{low}}{T_{high}} + \frac{K\cdot R}{S^2\cdot T_{high}}\cdot(1+m)^2 + (1+m)} \tag{8}$$

From (Eq. 8), it is possible to define the figure of merit zT, a non-dimensional parameter that describes the thermoelectric efficiency of the materials. This is the parameter that relates properties such as the Seebeck coefficient, the thermal conductivity and the electrical conductivity, σ, (Eq. 9). This figure of merit presents higher values for semiconductor materials, which are the most indicated for thermoelectric applications (Prasad *et al.* 2018).

$$zT = \frac{S^2\cdot\sigma\cdot T}{k} \tag{9}$$

Additionally, in the expression for η, it is possible to find the Carnot efficiency, which is the maximum efficiency of a heat engine, determined uniquely by the operating temperature gradient. Therefore, the equation for the efficiency can be simplified by Eq.10 (Prasad *et al.* 2018).

$$\eta = \eta_{Carnot} \cdot \frac{m}{-\frac{1}{2}\cdot\eta_{Carnot} + \frac{(1+m)^2}{zT_{high}} + (1+m)} \tag{10}$$

METHODOLOGY

After bibliographical research, a planar type device was chosen for the thermoelectric generator, due to its compactness, which is ideal for electronic circuits. Next, the initial planar TEG (Fig. 1a) was modelled in SOLDWORKS® 2019 and dimensioned according to Madan *et al.* (2011).

Exporting the model to ANSYS® Mechanical 2020, there is a need to create a material attribution. A p- and n-type bismuth telluride, Bi_2Te_3, legs were linked by a silver connector at the top. And at the bottom of each leg, two silver connections were installed to connect with more single units, in order to obtain a chain of TEG connected electrically in series and thermally in parallel, deposited onto a polyimide substrate.

Since Bi_2Te_3 was not defined in the software, it was required to introduce the respective thermoelectric properties in ANSYS®. Resorting to Fraisse *et al.* (2013), the necessary thermoelectric properties, approximations of the Seebeck coefficient S (Eq. 11), thermal conductivity k (Eq. 12) and electrical conductivity σ (Eq. 13) of the material, are fully defined.

$$\begin{cases} S(T) = (22224 + 930.6\cdot T - 0.9905\cdot T^2)\cdot 10^{-9} & [V\,K^{-1}] \quad (11) \\ k(T) = (62605 - 277.7\cdot T + 0.4131\cdot T^2)\cdot 10^{-4} & [W\,m^{-1}\,K^{-1}] \quad (12) \\ \sigma(T) = (5112 + 163.4\cdot T + 0.6279\cdot T^2)^{-1}\cdot 10^{10} & [S\,m^{-1}] \quad (13) \end{cases}$$

Furtherly, a mesh of 5308 quadrangular elements with an element size of 59 μm was applied to the three-dimensional model (Fig. 1b). The generated mesh corresponds to the maximum number of elements allowed in the used student software version, and it is necessary to understand if it is refined enough to produce satisfactory results. Therefore, it is necessary to make a mesh convergence test. To start, three temperature gradients were established – setting the heat sink as the environment, at an ambient temperature of 20ºC, the temperature of the heat source was defined as 30ºC, 260ºC and 500ºC, resulting in a gradient of 10ºC, 240ºC and 480ºC, respectively – and the voltage was measured for different mesh sizes.

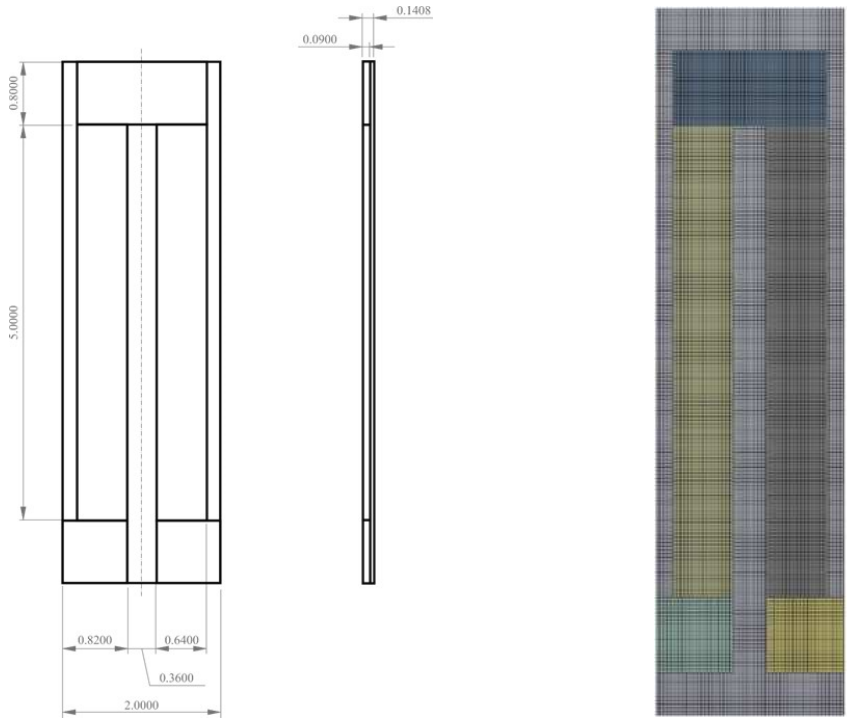

(a) (b)

Fig. 1 - (a) Initial drawing of the TEG; (b) Representation of the mesh used in the simulation

The correlation between the size and the number of elements in the ten generated meshes is presented in Table 1.

Table 1 - Correlation between size and number of elements of the mesh

Situation	**I**	**II**	**III**	**IV**	**V**	**VI**	**VII**	**VIII**	**IX**	**X**
Mesh size [μm]	100	95	90	85	80	75	70	65	60	59
Number of elements	980	1066	1247	2688	2876	3380	4032	4432	5264	5308

The evolution of the voltage as well as the computational time from the simulation process were taken for each gradient of 10ºC (Figure 2a), 240ºC (Figure 2b) and 480ºC (Figure 2c) as a function of the number of elements of the mesh. Analysing the obtained results, it is safe to conclude that the voltage does not significantly change with the increase of the refinement of the mesh. Additional, despite the increase of the computational time with the sophistication of the mesh, it is still a manageable simulation time. Therefore, the maximum mesh size is used for the simulations since the difference in computational time is negligible.

In order to perform simulations, it is necessary to state the conditions in which the model is simulated; in other words, it is mandatory to define the boundary-conditions associated with the physical phenomena involved, namely the thermoelectric and heat transfer. Thermal, electrical and convective boundary-conditions were defined.

Firstly, the top surface of the top silver contact was set as 150ºC whereas the temperature of the bottom surface of both bottom contacts was defined as 20ºC, the ambient temperature. Additionally, the voltage of the left surface of the bottom left silver contact was defined as 0 V in order to achieve the maximum absolute voltage on the right bottom silver contact. Finally, the remaining surfaces were assumed as perfectly isolated, which is the same as deeming radiation and convection insignificant and assuming conduction as the only heat transfer mechanism.

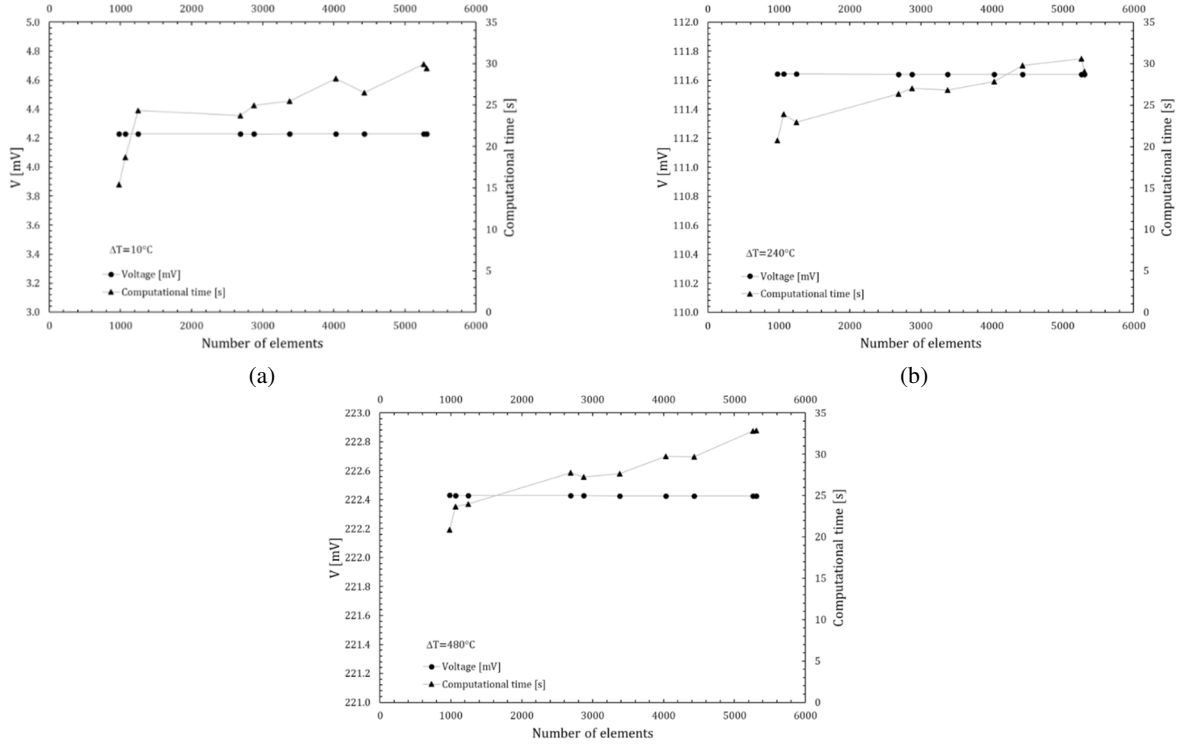

Fig. 2 - Voltage and computational time vs. number of elements for (a) a gradient of 10ºC; (b) a gradient of 240ºC; (c) a gradient of 480ºC

RESULTS AND CONCLUSIONS

Preceding the optimization process a sensitivity analysis was performed. In this section, the influence of some geometrical parameters in the global performance of the thermoelectric generator is going to be quantified. This way, it is possible to understand the necessary adjustments on the initial design to reach the final and optimized design for the generator.

Firstly, the legs are going to be analysed. As seen before, the thermoelectric process of converting heat into electricity occurs in the p- and n-type legs, meaning these components could impact the resulting properties, namely the voltage and the absorbed and rejected heats. The leg height (Figure 3a and Figure 3b) and the leg width (Figure 4a and Figure 4b) were changed and the model performance was simulated.

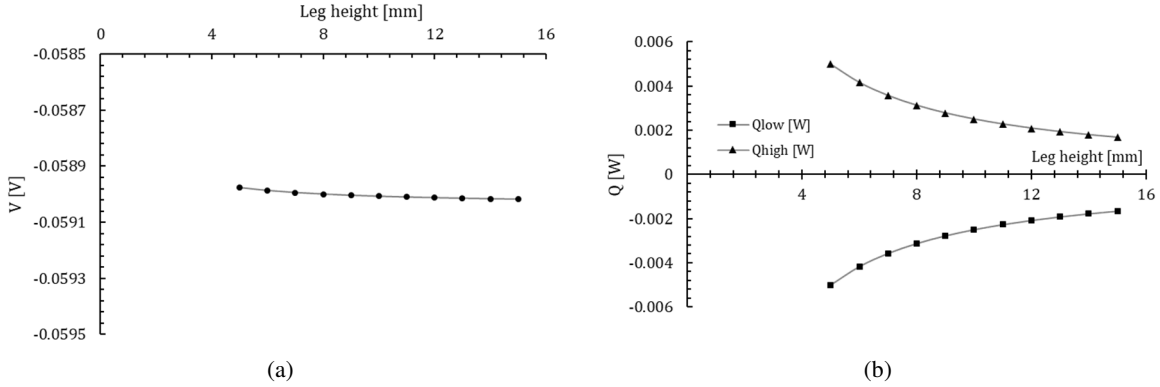

Fig. 3 - Impact of the leg height (a) in the obtained voltage; (b) in the absorbed and rejected heat flows

The influence on the resulting voltage is minimal since the Seebeck coefficient is independent of geometric parameters, but the impact is noticeable in the heat flow absorbed from the heat source, Q_{high}, and the heat flow rejected to the heat sink, Q_{low}. The differences can be easily explained by (Eq. 6) and (Eq. 7).

Equating L to the leg height and A as the product of the depth with the width of the legs, it is easily concluded that increasing the height of the legs leads to the increase of the resistance and the decrease of heat flows. Moreover, the increase of the cross-sectional area returns a smaller thermal resistance which in turn leads to an increase of the absorbed heat flow, and consequently the rejected heat flow (Chen *et al.* 2002).

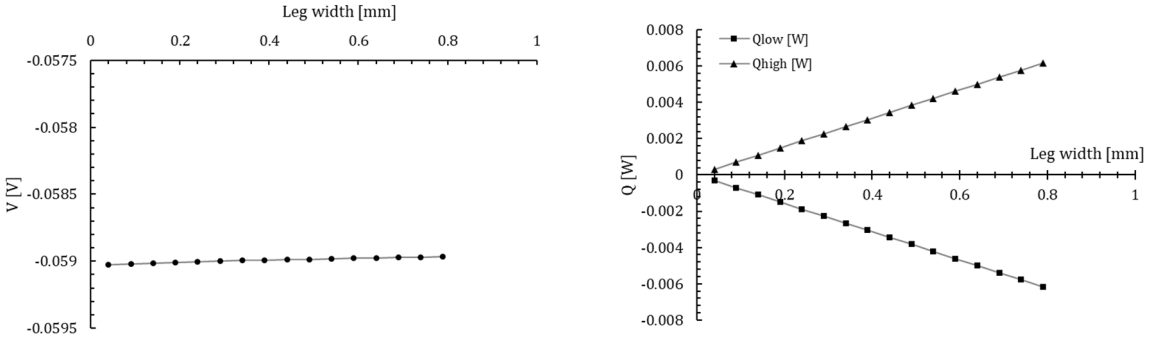

Fig. 4 - Impact of the leg width (a) in the obtained voltage; (b) in the absorbed and rejected heat flows

Secondly, an analysis of the height and width of the silver conductors is going to take place. These conductors act as a bridge between consecutive units, and their dimensions might affect the performance. Through the simulation, however, it is possible to observe that the height (Figure 5a and Figure 5b) and the width (Figure 6a and Figure 6b) of the conductors have no impact on the obtained voltage or heat flows. Once more, the conversion of heat into electricity is not influenced by the geometrical parameters. Furthermore, silver is a metal and has very high values for the thermal conductivity, equal to 419 $Wm^{-1}K^{-1}$, whereas k of bismuth telluride at this temperature range is 217.3 $Wm^{-1}K^{-1}$, meaning that geometrical adjustments become negligible in comparison to the magnitude of k.

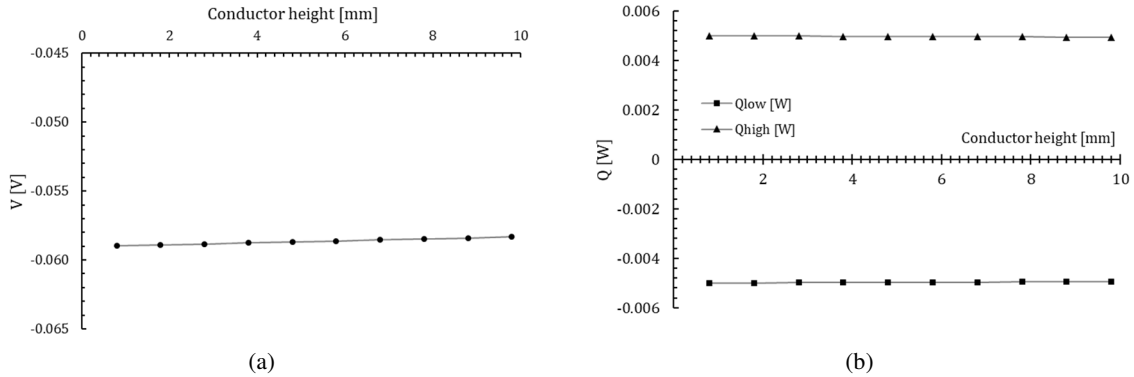

Fig. 5 - Impact of the conductor height (a) in the obtained voltage; (b) in the absorbed and rejected heat flows

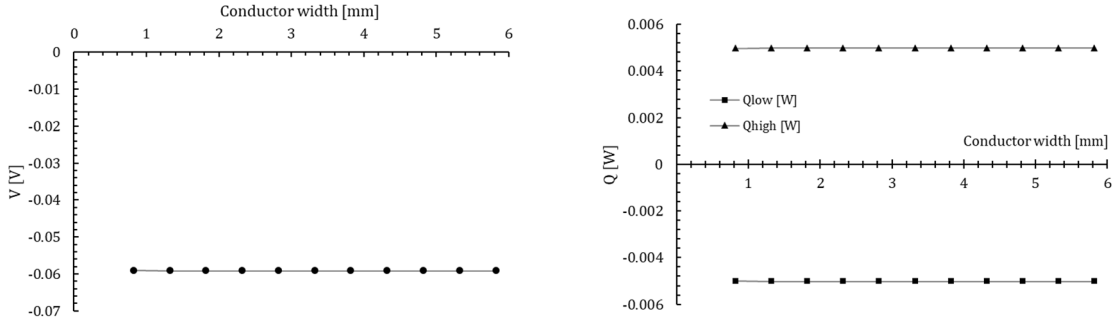

(a) (b)

Fig. 6 - Impact of the conductor width (a) in the obtained voltage; (b) in the absorbed and rejected heat flows

Finally, the depth of the model was analysed. As predicted by the previous justifications, the voltage output (Figure 7a) became unaffected whereas the heat flows (Figure 7b) increased because the cross-section of the model also increased.

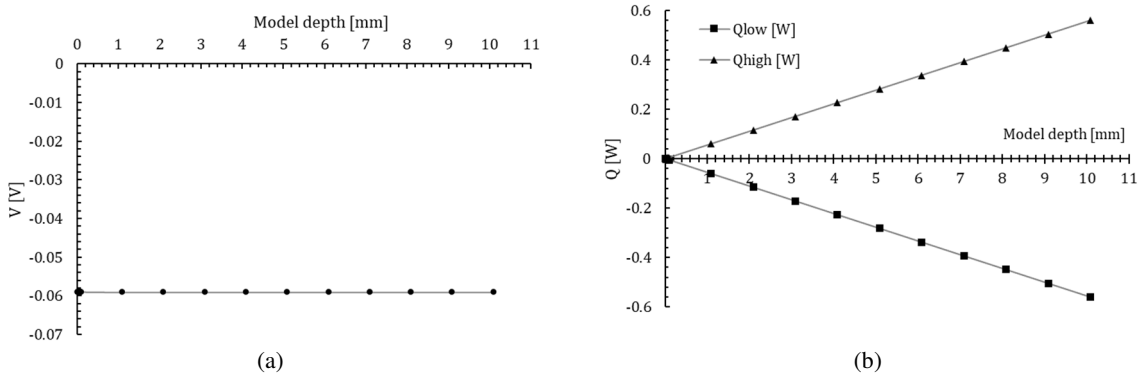

(a) (b)

Fig. 7 - Impact of the model depth (a) in the obtained voltage; (b) in the absorbed and rejected heat flows

It became apparent that the increase of the voltage can only be achieved by the geometric adaptation of the semiconductor legs, whereas the decrease of the necessary heat flows required the combination of different changes throughout the whole model.

Performing a numerical simulation of the first design, the heat flux generated an electrical differential of 58.976 mV and the total current density peaked at 4039.8 Am^{-2}. The temperature and electrical potential distribution (Figure 8a and Figure 8b, respectively) reveal the continuous evolution of these thermoelectric properties. As displayed by the figures, the units, connected at the bottom, will be in series electrically and in parallel thermally, given the spatial distribution of these properties.

The real thermoelectric generator is going to be connected in a closed loop to the device it is meant to power. It is assumed that the load resistance is unitary for simplification sake, and that the thermoelectric generator is limited by a width of 100 mm and a height of 25 mm.

Finally, the thermoelectric generator must have the smallest possible depth, which is determined by the dispensing printer. In fact, the minimum film depth allowed by the nozzle of the used printer is 90 μm, and, therefore, the depth of the initial design is preserved.

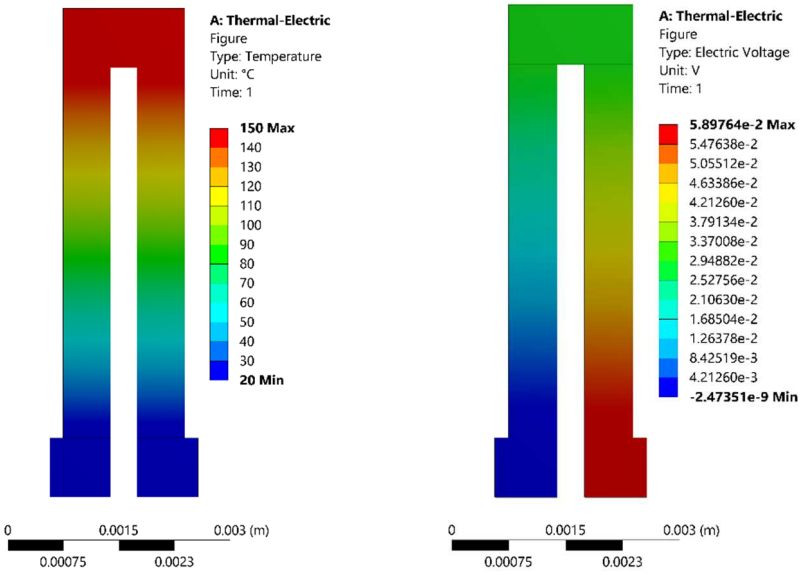

(a) (b)

Fig. 8 - (a) Temperature profile of the TEG; (b) Voltage profile of the TEG, both for the established boundary-conditions

The width and height of the thermoelectric were adjusted in a parametric analysis and the resulting power output was computed (Figure 9).

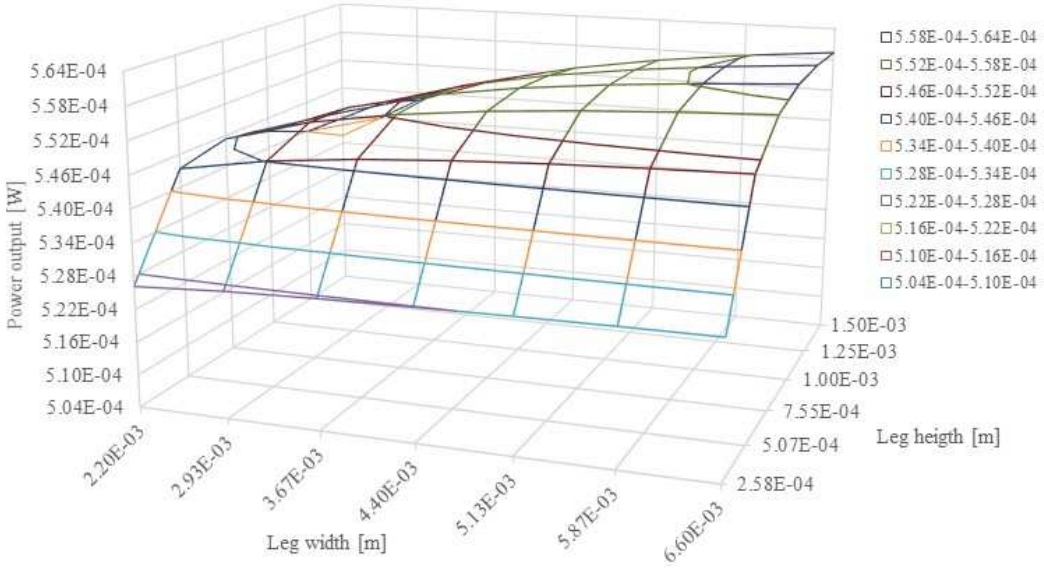

Fig. 9 - Graphical representation of the evolution of leg height, width and output power

It was concluded that the height and width of the semiconductor legs should be 0.732 mm and 2.1 mm, respectively, resulting in an output power of 0.5437 mW. Therefore, the final design for the thermoelectric generator unit has been achieved for the purposed application (Figure 10).

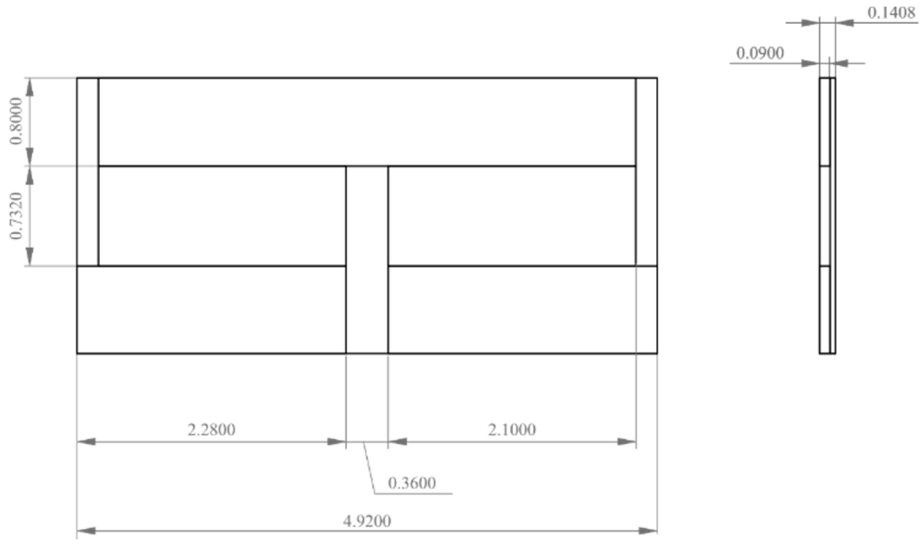

Fig. 10 - Final drawing of the TEG

FUTURE WORK

For the experimental set-up, 20 thermoelectric units in series are going to be produced considering the geometric differences brought by the optimization process of a single unit. It would be interesting to attest the theoretical and the numerical simulation values with experimental ones, to understand not only the validity of the theoretical equations and their mathematical manipulation, but also the simulation process and optimization that was done to improve the design.

ACKNOWLEDGMENTS

Authors gratefully acknowledge the Engineering Faculty of University of Porto (FEUP), the Department of Mechanical Engineering (DEMec) of FEUP, the Institute of Science and Innovation in Mechanical and Industrial Engineering (LAETA-INEGI) and the Centre for Nanotechnology and Smart Materials (CeNTI).

REFERENCES

[1] Baranowski L, Snyder G, Toberer E, Concentrated solar thermoelectric generators. Energy and Environmental Science, 2012, pp.9055-9067.

[2] Chen L, Gong J, Sun F, Wu C, Effect of heat transfer on the performance of thermoelectric generators. International Journal of Thermal Sciences, 2002.

[3] Fraisse G, Ramousse J, Sgorlon D, Goupil C, Comparison of different modeling approaches for thermoelectric elements. Energy Conversion and Management 65, 2013, pp.301-356.

[4] He J, Terry M, Advances in thermoelectric materials research: Looking back and moving forward. Science, 2017, pp.1.

[5] He W, Zhang G, Zhang X, Li J, Li G, Zhao X, Recent development and application of thermoelectric generator and cooler. Applied Energy, 2015.

[6] Incropera F, DeWitt D, Bergman T, Lavine A, Fundamentals of Heat and Mass Transfer. Michigan: Wiley, 2007.

[7] Madan D, Chen A, Wright P, Evans J, Dispenser printed composite thermoelectric thick films for thermoelectric generator applications. Journal of Applied Physics, 2011.

[8] Prasad, A, Thiagarajan R, Multiphysics Modelling and Multilevel Optimization of Thermoelectric Generator for Waste Heat Recovery. ATOA Scientific Technologies, 2018.

[9] Suarez F, Nozariasbmarz A, Vashaee D, Öztürk M, Designing thermoelectric generators for self-powered wearable electronics. Energy and Environmental Science, 2016, pp.2099-2113.

References

[1] Song Lan, Zhijia Yang, Rui Chen, and Richard Stobart. A dynamic model for thermoelectric generator applied to vehicle waste heat recovery. *Applied Energy*, 210(June 2017):327–338, 2018.

[2] Karol Sztekler, Krzysztof Wojciechowski, and Maciek Komorowski. The thermoelectric generators use for waste heat utilization from conventional power plant. *E3S Web of Conferences*, 14, 2017.

[3] Pradeepkumar Sundarraj, Dipak Maity, Susanta Sinha Roy, and Robert A. Taylor. Recent advances in thermoelectric materials and solar thermoelectric generators-a critical review. *RSC Advances*, 4(87):46860–46874, 2014.

[4] Hadi Ali Madkhali, Ali Hamil, and Ho Sung Lee. Validation, Optimization and Simulation of a Solar Thermoelectric Generator Model. *Journal of Electronic Materials*, 46(12):6756–6768, 2017.

[5] Ding Zhang, Yuanhao Wang, and Ya Yang. Design, Performance, and Application of Thermoelectric Nanogenerators. *Small*, 15(32):1–13, 2019.

[6] Mohd Quasim Khan, S. Malarmannan, and G. Manikandaraja. Power generation from waste heat of vehicle exhaust using thermo electric generator: A review. *IOP Conference Series: Materials Science and Engineering*, 402(1), 2018.

[7] Nicholas Kempf and Yanliang Zhang. Design and optimization of automotive thermoelectric generators for maximum fuel efficiency improvement. *Energy Conversion and Management*, 121:224–231, 2016.

[8] Wei He, Shixue Wang, Chi Lu, Xing Zhang, and Yanzhe Li. Influence of different cooling methods on thermoelectric performance of an engine exhaust gas waste heat recovery system. *Applied Energy*, 162:1251–1258, 2016.

[9] Wei He, Shixue Wang, Yulong Zhao, and Yanzhe Li. Effects of heat transfer characteristics between fluid channels and thermoelectric modules on optimal thermoelectric performance. *Energy Conversion and Management*, 113:201–208, 2016.

[10] Wei He, Shixue Wang, Yanzhe Li, and Yulong Zhao. Structural size optimization on an exhaust exchanger based on the fluid heat transfer and flow resistance characteristics applied to an automotive thermoelectric generator. *Energy Conversion and Management*, 129:240–249, 2016.

[11] T. Zhang. New thinking on modeling of thermoelectric devices. *Applied Energy*, 168:65–74, 2016.

[12] Jaideep Pandit, Megan Thompson, Srinath V. Ekkad, and Scott T. Huxtable. Effect of pin fin to channel height ratio and pin fin geometry on heat transfer performance for flow in rectangular channels. *International Journal of Heat and Mass Transfer*, 77:359–368, 2014.

[13] Xiaonan Ma, Gequn Shu, Hua Tian, Haoqi Yang, and Tianyu Chen. Optimization of length ratio in segmented thermoelectric generators for engine's waste heat recovery. *Energy Procedia*, 158:583–588, 2019.

[14] Jean Marie Dilhac, Romain Monthéard, Marise Bafleur, Vincent Boitier, Paul Durand-Estèbe, and Patrick Tounsi. Implementation of thermoelectric generators in airliners for powering battery-free wireless sensor networks. *Journal of Electronic Materials*, 43(6):2444–2451, 2014.

[15] V. V. Gusev, A. A. Pustovalov, N. N. Rybkin, L. I. Anatychuk, B. N. Demchuk, and I. Yu Ludchak. Milliwatt-power radioisotope thermoelectric generator (RTG) based on plutonium-238. *Journal of Electronic Materials*, 40(5):807–811, 2011.

[16] Zicheng Yuan, Xiaobin Tang, Zhiheng Xu, Junqin Li, Wang Chen, Kai Liu, Yunpeng Liu, and Zhengrong Zhang. Screen-printed radial structure micro radioisotope thermoelectric generator. *Applied Energy*, 225(February):746–754, 2018.

[17] Richard R. Furlong and Earl J. Wahlquist. U . S . space missions using radioisotope power systems. *Nuclear News*, 4(2):26–34, 1999.

[18] Abu Raihan Mohammad Siddique, Ronil Rabari, Shohel Mahmud, and Bill Van Heyst. Thermal energy harvesting from the human body using flexible thermoelectric generator (FTEG) fabricated by a dispenser printing technique. *Energy*, 115:1081–1091, 2016.

[19] Francisco Suarez, Amin Nozariasbmarz, Daryoosh Vashaee, and Mehmet C. Öztürk. Designing thermoelectric generators for self-powered wearable electronics. *Energy and Environmental Science*, 9(6):2099–2113, 2016.

[20] Linden K. Allison and Trisha L. Andrew. A Wearable All-Fabric Thermoelectric Generator. *Advanced Materials Technologies*, 4(5):1–7, 2019.

[21] Welcome to *centi*. https://www.centi.pt/en/about/welcome. Accessed: 2020-02-24.

[22] Ssennoga Twaha, Jie Zhu, Yuying Yan, and Bo Li. A comprehensive review of thermoelectric technology: Materials, applications, modelling and performance improvement. *Renewable and Sustainable Energy Reviews*, 65:698–726, 2016.

[23] Yan Chen, Xiangnan Hou, Chunyan Ma, Yinke Dou, and Wentao Wu. Review of Development Status of Bi2Te3-Based Semiconductor Thermoelectric Power Generation. *Advances in Materials Science and Engineering*, 2018, 2018.

[24] G. Jeffrey Snyder and Eric S. Toberer. Complex thermoelectric materials. *Nature Materials*, 7(2):105–114, 2008.

[25] Thomas johann seebeck. https://www.britannica.com/biography/Thomas-Johann-Seebeck. Accessed: 2020-03-05.

[26] Chhatrasal Gayner and Kamal K. Kar. Recent advances in thermoelectric materials. *Progress in Materials Science*, 83:330–382, 2016.

[27] Shripad Dhoopagunta. Analytical Modeling and Numerical Simulation of a Thermoelectric Generator Including Contact Resistances. *Master's Theses*, 2016.

[28] H. Julian Goldsmid. Bismuth telluride and its alloys as materials for thermoelectric generation. *Materials*, 7(4):2577–2592, 2014.

[29] R. Bjørk, A. Sarhadi, N. Pryds, N. Lindeburg, and P. Viereck. A thermoelectric power generating heat exchanger: Part i - Experimental realization. *Energy Conversion and Management*, 119:473–480, 2016.

[30] December 1840: Joule's abstract on converting mechanical power into heat. https://www.aps.org/publications/apsnews/200912/physicshistory.cfm. Accessed: 2020-02-25.

[31] William thomson, baron kelvin. https://www.britannica.com/biography/William-Thomson-Baron-Kelvin. Accessed: 2020-03-05.

[32] Guangxi Wu and Xiong Yu. A holistic 3D finite element simulation model for thermoelectric power generator element. *Energy Conversion and Management*, 86:99–110, 2014.

[33] J. Kestin. *Thermodynamics and Statistical Mechanics*. Elsevier Science, 2012.

[34] Olle Högblom and Ronnie Andersson. A simulation framework for prediction of thermoelectric generator system performance. *Applied Energy*, 180:472–482, 2016.

[35] Christian Lundgaard and Ole Sigmund. A density-based topology optimization methodology for thermoelectric energy conversion problems. *Structural and Multidisciplinary Optimization*, 57(4):1427–1442, 2018.

[36] Mingjian Liao, Zhu He, Chengpeng Jiang, Xi'an Fan, Yawei Li, and Fengsheng Qi. A three-dimensional model for thermoelectric generator and the influence of Peltier effect on the performance and heat transfer. *Applied Thermal Engineering*, 133(January):493–500, 2018.

[37] Jeannine R. Szczech, Jeremy M. Higgins, and Song Jin. Enhancement of the thermoelectric properties in nanoscale and nanostructured materials. *Journal of Materials Chemistry*, 21(12):4037–4055, 2011.

[38] Frank P. Incropera. *Fundamentals of Heat and Mass Transfer*. John Wiley & Sons, Inc., Hoboken, NJ, USA, 2006.

[39] Charles Kittel. *Introduction to Solid State Physics, 8th edition*. Wiley & Sons, New York, NY, 8th edition edition, 2004.

[40] M. N. Tripathi, C. M. Bhandari, and M. P. Singh. Lorenz number in low-dimensional structures. *Physica B: Condensed Matter*, 405(23):4818–4820, 2010.

[41] Olga Bubnova and Xavier Crispin. Towards polymer-based organic thermoelectric generators. *Energy and Environmental Science*, 5(11):9345–9362, 2012.

[42] Mario Culebras, Clara M. Gómez, and Andrés Cantarero. Review on polymers for thermoelectric applications. *Materials*, 6(9):6701–6732, 2014.

[43] Lon E Bell and Francis J. DiSalvo. Cooling , Heating , Generating Heat with and Recovering Waste Thermoelectric. *Science*, 321(JULY):1457–1461, 2008.

[44] Xiaodong Jia and Yuanwen Gao. Optimal design of a novel thermoelectric generator with linear-shaped structure under different operating temperature conditions. *Applied Thermal Engineering*, 78:533–542, 2015.

[45] Xiaodong Jia and Yuanwen Gao. Estimation of thermoelectric and mechanical performances of segmented thermoelectric generators under optimal operating conditions. *Applied Thermal Engineering*, 73(1):335–342, 2014.

[46] Chang Jiang Yao, Hao Li Zhang, and Qichun Zhang. Recent progress in thermoelectric materials based on conjugated polymers. *Polymers*, 11(1):1–19, 2019.

[47] Jian He and Terry M. Tritt. Advances in thermoelectric materials research: Looking back and moving forward. *Science*, 357(6358), 2017.

[48] Fuqiang Cheng. Calculation Methods for Thermoelectric Generator Performance. *Thermoelectrics for Power Generation - A Look at Trends in the Technology*, 2016.

[49] Linhao Fan, Guobin Zhang, Renfang Wang, and Kui Jiao. A comprehensive and time-efficient model for determination of thermoelectric generator length and cross-section area. *Energy Conversion and Management*, 122:85–94, 2016.

[50] Wei He, Gan Zhang, Xingxing Zhang, Jie Ji, Guiqiang Li, and Xudong Zhao. Recent development and application of thermoelectric generator and cooler. *Applied Energy*, 143:1–25, 2015.

[51] E. Massaguer, A. Massaguer, L. Montoro, and J. R. Gonzalez. Development and validation of a new TRNSYS type for the simulation of thermoelectric generators. *Applied Energy*, 134:65–74, 2014.

[52] Assmelash Negash. Direct contact thermoelectric generator (DCTEG): A concept for removing the contact resistance between thermoelectric modules and heat source. *Energy Conversion and Management*, 142:20–27, 2017.

[53] A. Chen, D. Madan, P. K. Wright, and J. W. Evans. Dispenser-printed planar thick-film thermoelectric energy generators. *Journal of Micromechanics and Microengineering*, 21(10), 2011.

[54] Camille Favarel, Jean Pierre Bédécarrats, Tarik Kousksou, and Daniel Champier. Experimental analysis with numerical comparison for different thermoelectric generators configurations. *Energy Conversion and Management*, 107:114–122, 2016.

[55] Lauryn L. Baranowski, G. Jeffrey Snyder, and Eric S. Toberer. Concentrated solar thermoelectric generators. *Energy and Environmental Science*, 5(10):9055–9067, 2012.

[56] Nesrine Jaziri, Ayda Boughamoura, Jens Müller, Brahim Mezghani, Fares Tounsi, and Mohammed Ismail. A comprehensive review of Thermoelectric Generators: Technologies and common applications, 2019.

[57] Fei Jiao. Flexible Thermoelectrics and Thermoelectric Textiles. *Flexible and Wearable Electronics for Smart Clothing*, pages 49–66, 2020.

[58] Jin-cheng Zheng. Recent advances on thermoelectric materials. *Frontiers of Physics in China*, 3(3):269–279, Jul 2008.

[59] Element collection, inc. https://periodictable.com/. Accessed: 2020-03-30.

[60] Geffrey K. Ottman and Christopher B. Hersman. The pluto-new horizons RTG and power system early mission performance. *Collection of Technical Papers - 4th International Energy Conversion Engineering Conference*, 1:309–316, 2006.

[61] Teahoon Park, Hanwhuy Lim, Jong Un Hwang, Jongbeom Na, Hyunki Lee, and Eunkyoung Kim. Roll type conducting polymer legs for rigid-flexible thermoelectric generator. *APL Materials*, 5(7), 2017.

[62] Jianxiong Zhu, Zhonglin Xu, and Luyu Jia. Design and fabrication of 3D flexible thermoelectric energy generator using chemical vapor deposition method based on paper substrate. *2018 International Symposium in Sensing and Instrumentation in IoT Era, ISSI 2018*, pages 1–4, 2018.

[63] Zhisong Lu, Huihui Zhang, Cuiping Mao, and Chang Ming Li. Silk fabric-based wearable thermoelectric generator for energy harvesting from the human body. *Applied Energy*, 164:57–63, 2016.

[64] Hend M. Elmoughni, Akanksha K. Menon, Rylan M.W. Wolfe, and Shannon K. Yee. A Textile-Integrated Polymer Thermoelectric Generator for Body Heat Harvesting. *Advanced Materials Technologies*, 4(7):1–6, 2019.

[65] Robert Freer and Anthony V. Powell. Realising the potential of thermoelectric technology: A Roadmap. *Journal of Materials Chemistry C*, 8(2):441–463, 2020.

[66] Flexibility: Flexural modulus. https://omnexus.specialchem.com/polymer-properties/properties/flexibility?id=307. Accessed: 2020-04-28.

[67] Ju Hyung We, Sun Jin Kim, and Byung Jin Cho. Hybrid composite of screen-printed inorganic thermoelectric film and organic conducting polymer for flexible thermoelectric power generator. *Energy*, 73:506–512, 2014.

[68] João Paulo Carmo, Luis Miguel Goncalves, Reinoud F. Wolffenbuttel, and José Higino Correia. A planar thermoelectric power generator for integration in wearable microsystems. *Sensors and Actuators, A: Physical*, 161(1-2):199–204, 2010.

[69] Li Yang, Keng Hsu, Brian Baughman, Donald Godfrey, Francisco Medina, Mamballykalathil Menon, and Soeren Wiener. *Additive Manufacturing of Metals: The Technology, Materials, Design and Production*. Springer International Publishing, 2017.

[70] Joseph P Heremans, Vladimir Jovovic, and Donald T Morelli. Ternary Thermoelectric Materials and Methods of Fabrication, 2009.

[71] Z. Cao, J. J. Shi, R. N. Torah, M. J. Tudor, and S. P. Beeby. All dispenser printed flexible 3D structured thermoelectric generators. *Journal of Physics: Conference Series*, 660(1), 2015.

[72] Deepa Madan, Alic Chen, Paul K. Wright, and James W. Evans. Dispenser printed composite thermoelectric thick films for thermoelectric generator applications. *Journal of Applied Physics*, 109(3), 2011.

[73] Witold Brostow, Tea Datashvili, Haley E.Hagg Lobland, Travis Hilbig, Lisa Su, Carolina Vinado, and John White. Bismuth telluride-based thermoelectric materials: Coatings as protection against thermal cycling effects. *Journal of Materials Research*, 27(22):2930–2936, 2012.

[74] Francesco Gucci, Fabiana D'Isanto, Ruizhi Zhang, Michael J. Reece, Federico Smeacetto, and Milena Salvo. Oxidation protective hybrid coating for thermoelectric materials. *Materials*, 12(4):1–11, 2019.

[75] G. Fraisse, J. Ramousse, D. Sgorlon, and C. Goupil. Comparison of different modeling approaches for thermoelectric elements. *Energy Conversion and Management*, 65:351–356, 2013.

[76] A. O. Galitskaya and R. D. Buslaev. Simulation of flexible thermoelectric generators with different geometry. *Journal of Physics: Conference Series*, 1326(1), 2019.

[77] Boron nitride coating. https://www.final-materials.com/gb/177-boron-nitride-coating. Accessed: 2020-05-28.

[78] Chao Yuan, Jiahan Li, Lucas Lindsay, David Cherns, James W. Pomeroy, Song Liu, James H. Edgar, and Martin Kuball. Modulating the thermal conductivity in hexagonal boron nitride via controlled boron isotope concentration. *Communications Physics*, 2(1):1–8, 2019.

[79] Matthew M. Barry, Kenechi A. Agbim, Parthib Rao, Corey E. Clifford, B. V.K. Reddy, and Minking K. Chyu. Geometric optimization of thermoelectric elements for maximum efficiency and power output. *Energy*, 112:388–407, 2016.

[80] Loise Rissini Kramer, Anderson Luis Oliveira Maran, Samara Silva De Souza, and Oswaldo Hideo Ando. Analytical and numerical study for the determination of a thermoelectric generator's internal resistance. *Energies*, 12(16), 2019.